Enhancing the Performance of Quantum Computers

Dissertation

zur Erlangung des Grades

des Doktors der Naturwissenschaften

der Naturwissenschaftlich - Technischen Fakultät

der Universität des Saarlandes

von

Lukas Simon Theis

Saarbrücken

2018

Tag des Kolloquiums: 09. April 2019

Dekan: Prof. Dr. Guido Kickelbick

Berichterstatter: Prof. Dr. Frank Wilhelm-Mauch

                       Prof. Dr. Steffen Glaser

                       Prof. Dr. Ludger Santen

Vorsitz: Prof. Dr. Christoph Becher

Akad. Mitarbeiter: Dr. Adam Wysocki

Für meine Eltern.

Acknowledgements

Abstract

Recent progress in quantum information technology suggests that we will soon be able to carry out computational tasks that are intractable on classical computers. In the common quantum circuit model that divides the underlying quantum algorithms into discrete gates, it is crucial to perform each of these gates with high accuracy. In this thesis we develop an effective model required to precisely describe interactions between superconducting qubits mediated by a resonator. An analytical technique to design optimal control shapes based on derivatives of some base waveform is reviewed, connecting it to related methodology in literature and completing with novel insights. Using this technique, we develop improved pulse sequences to entangle two Rydberg atoms via the Rydberg-blockade interaction and achieve fidelities beyond what previously appeared to be a fundamental limit. A modern optimal control algorithm that combines analytical pulse shapes with numerical optimization is used to study the generation of entanglement between trapped ions. Additionally, we focus on cooling superconducting qubits in adiabatic quantum computation where computational problems are solved by adiabatically changing the Hamiltonian of a quantum system. Errors due to imperfect adiabatic evolution and finite temperatures deteriorate performance in such protocols. We propose a novel approach to reducing these errors efficiently, overcoming limits of previous cooling schemes.

Zusammenfassung

Aktuelle Entwicklungen im Gebiet Quanteninformationstechnologie lassen erwarten, dass bald erste Rechnungen auf Quantencomputern durchgeführt werden, die auf klassischen Computern nicht ausführbar sind. Unterteilt man die zugrunde liegenden Quantenalgorithmen in individuelle Gatter, ist es nötig, diese Gatter mit hoher Genauigkeit auszuführen. In dieser Arbeit erarbeiten wir ein effektives Modell zur genauen Beschreibung der mittels eines Resonators vermittelten Wechselwirkung zwischen supraleitenden Qubits. Eine analytische Technik zur präzisen Systemkontrolle mittels Ableitungen einer Funktion wird in neuartiger Form aufgearbeitet, in Bezug zu verwandten Methoden gesetzt und durch bisher unveröffentlichte Erkenntnisse vervollständigt. Anhand dessen entwickeln wir verbesserte Sequenzen zur Verschränkung zweier Rydbergatome mittels der Rydberg-Blockade und überwinden bisher vermutete Einschränkungen. Ein moderner Algorithmus, der analytische Pulsformen mit numerischer Optimierung kombiniert, wird genutzt, um die Verschränkung zwischen gefangenen Ionen zu untersuchen. Daneben untersuchen wir Kühlprozesse im adiabatischen Quantencomputing, bei dem Probleme durch adiabatisches Umschalten des Hamiltonians eines Quantensystems gelöst werden. Wir schlagen eine neue Methode vor, um in solchen Verfahren relevante Fehler aufgrund imperfekter Adiabatizität und endlicher Temperatur effektiv zu reduzieren und überwinden dabei Einschränkungen bisheriger Verfahren.

Contents

List of Figures

Part I

Introduction

Chapter 1

Quantum Information Processing and Computation

It is impossible to imagine our everyday life without computers. They take on heavy computational tasks for research and development purposes, automatically control and monitor various electrical devices, or are even used as communication tools in everyone's pockets. After Bardeen, Shockley and Brattain presented the first working solid state amplifier (a transistor) at Bell Labs in December 1947, further improvements of the transistor revolutionized technological progress in all areas of electronics in the twentieth century. Transistors are key to central processing units (CPUs), where their continuously decreasing physical dimensions – from a few centimeters in their early stages to only a few nanometers at present – allow to keep on enhancing performance and computational power.

Remarkably, albeit the functionality of transistors – particularly, but nonexclusively, the description of energy bands – relies on quantum mechanics, computers as we are still used to them process information according to the laws of classical physics. The key element of classical information is a *bit*: It can be assigned to either have value 0 or 1, and information is encoded in long strings of zeros and ones. To process information and perform computational tasks, different logical operations (*gates*) exist. A simple fundamental example is an AND gate between two bits: Its outcome is 1 only if both input bits are 1, otherwise it will return 0. It turns out that any logical operation on bits can be decomposed for instance in terms of NAND gates (inverted AND), provided that a bit can be replaced by two identical copies of itself (this is referred to as FANOUT operation). The NAND gate is therefore considered a *universal gate* of classical computation.

Transistors, together with other devices and phenomena that are based on quantum mechanics but otherwise act as macroscopic systems, can be

3

grouped unter the terminology Quantum Technology 1.0. Prominent examples are lasers, magnetic resonance and nuclear technology. Currently, new systems that belong to Quantum Technology 2.0 are emerging [1]: Systems that not only rely on quantum mechanics, but also explicitly make use of unique quantum properties of quantum systems to process information. A main concept thereof is a quantum computer: A computer that itself treats information quantum mechanically and opens new perspectives of computation. This idea was pioneered by Feynman [2] who wondered how quantum mechanics can be simulated with classical computers, given that the size of the Hilbert space grows exponentially with the number of particles in a quantum system. He proposed to use a well controlled quantum system to simulate another one, and thus the idea of a *universal quantum simulator* was born. A few years later, Deutsch [3] first proposed to apply quantum mechanics to computational problems.

In analogy to classical bits, the key unit of a quantum computer is referred to as a *quantum bit* (*qubit*). The fundamental and crucial difference between classical bits and qubits is that a qubit is not limited to two possible values. Since the value of a qubit, as will be detailed in section 1.1, is actually a quantum mechanical state, it can be in infinitely many superpositions of so-called *computational basis states*, denoted by $|0\rangle$ and $|1\rangle$, respectively. This substantiates a core advantage of quantum computing: An intrinsic quantum speed up due to massive parallelism without the need for multiple cores (as required for parallelization on classical hardware). However, taking advantage of this parallelism is not straightforward and quantum algorithms need to be designed with care. Nevertheless, it has been shown [4] that quantum algorithms can be more efficient than their *known* classical counterparts. Prominent examples are Grover's algorithm [5] to search an unsorted database and Shor's algorithm [6] for factoring large numbers. Note that often a proven bound on the efficiency of classical algorithms does not exist, and hence quantum algorithms can only be compared to the best known classical algorithm at date.

Given the perspectives of quantum computing, there is no longer only academic interest in the field. Industrial research, lead by multiple startups as well as Google, IBM, Intel and – with slightly different focus – by Microsoft and D-Wave Systems, is currently pushing the rapid development in the field of quantum hardware. The number of coherently operated qubits, however, is still orders of magnitude below what is needed for large-scale quantum computing of commercial interest. IBM and Intel released chips with 50 [7] and 49 [8] qubits, respectively, and Google took a major step forward with the announcement of a 72-qubit chip [9]. At the time of writing the performance of these chips still needs to be quantified. Although the announced qubit

numbers are orders of magnitude below of what is required for large-scale devices, the technological progress is remarkable and *quantum supremacy* – successful operation of a computational task on quantum hardware that cannot be run on classical computers – will potentially be demonstrated in the very near future [10, 11]. One of the first important applications of quantum hardware in near-term – before large-scale universal quantum computers exist – will likely lie in quantum chemistry, where small quantum devices can be used to study electronic structure problems of molecules [12, 13]. For instance, with contribution of about one to three percent to the global energy consumption, the Haber-Bosch process to synthesize ammonium is one of the largest industrial energy users worldwide [14]. Specialized quantum simulators could help to accurately engineer better catalysts for this and other processes, or even an alternative synthesization protocol with reduced energy consumption and less environmental pollution.

This thesis addresses two important aspects relevant for quantum technologies: First, it focuses on techniques to achieve accurate control of quantum systems and the derivation of accurate models to describe such systems. Second, it explores how heating in so-called quantum annealing devices can be suppressed efficiently. Both of these aspects are key to building universal quantum devices. The remainder of this part gives a fundamental introduction into the field of quantum information. Part II will address the question of how quantum systems can be manipulated in order to achieve a desired result, and how their dynamics can be described within an effective framework to significantly simplify their analysis. The majority of part II is based on the idea of running quantum algorithms as sequences of distinct operations, much like for classical computers. A different concept to build universal quantum devices will be introduced in part III and end with a discussion of how a specific fundamental error in these systems can be addressed.

1.1   Basic Introduction to Quantum Bits

Key to the algorithms implemented on quantum hardware is a proper mathematical toolset. In analogy to classical bits the fundamental concept to describe the state of quantum systems are *quantum bits* (short: *qubits*). Since they obey the rules of quantum mechanics [15] the state $|\psi\rangle$ can be any superposition of computational basis states, which – in analogy to classical bits – are referred to as $|0\rangle$ and $|1\rangle$, respectively. That is,

$$|\psi\rangle = \alpha\,|0\rangle + \beta\,|1\rangle \tag{1.1}$$

with complex probability amplitudes α and β. Since the state $|\psi\rangle$ must be normalized, the probabilities to find the system in either $|0\rangle$ or $|1\rangle$ need to sum up to one, i.e. $|\alpha|^2 + |\beta|^2 = 1$. This fundamental difference to a classical system, where bits can exclusively be either in state 0 or 1, gives rise to an intrinsic quantum speedup due to parallelization and hence paved the way for massive research and development in the field of quantum information over the last decades. An equivalent way to express the state of a qubit (1.1) is

$$|\psi\rangle = e^{i\gamma}\left(\cos\left(\frac{\theta}{2}\right)|0\rangle + e^{i\phi}\sin\left(\frac{\theta}{2}\right)|1\rangle\right) \tag{1.2}$$

where the qubit state is determined by a global phase γ as well as polar and azimuthal angles θ and ϕ, respectively. As the outcome of a measurement of some operator $\hat{M}$ is determined by $\langle\hat{M}\rangle = \langle\psi|\hat{M}|\psi\rangle$, which is independent of γ, the global phase γ has no observable effect and is hence typically neglected, so that the state $|\psi\rangle$ is solely determined by the angles (θ, ϕ). So far, we assumed that $|\psi\rangle$ is known exactly. More generally, a quantum state can be in one of a number of states $|\psi_i\rangle$ with corresponding probabilities p_i. The *density operator* (also: *density matrix*)

$$\hat{\rho} = \sum_i p_i |\psi_i\rangle\langle\psi_i| \tag{1.3}$$

is a means for describing that a quantum system can be in any of the ensembles of pure states $\{p_i, |\psi_i\rangle\}$. Any density operator $\hat{\rho}$ has to meet three fundamental properties: (i) Its trace equals one, (ii) it must be a positive operator and (iii) it must be Hermitian, i.e. $\hat{\rho} = \hat{\rho}^\dagger$. The density operator allows to characterize whether the state of a quantum system is known exactly, or a mixture of all possible ensembles. These two situations are referred to as *pure* and *mixed* states, respectively. For pure states, the trace of the squared density matrix equals one, i.e. $\mathrm{Tr}\left(\hat{\rho}^2\right) = 1$, while for a mixed state it will satisfy $\mathrm{Tr}\left(\hat{\rho}^2\right) < 1$. Representation (1.2) gives rise to a three dimensional visualization of quantum states on the so-called *Bloch sphere*, as illustrated in FIG. 1.1. The axes of the Bloch sphere correspond to eigenstates of the three Pauli matrices $\hat{\sigma}_x$, $\hat{\sigma}_y$ and $\hat{\sigma}_z$. Their matrix representations are

$$\hat{\sigma}_x = \begin{pmatrix} 0 & 1 \\ 1 & 0 \end{pmatrix}, \quad \hat{\sigma}_y = \begin{pmatrix} 0 & -i \\ i & 0 \end{pmatrix}, \quad \hat{\sigma}_z = \begin{pmatrix} 1 & 0 \\ 0 & -1 \end{pmatrix}.$$

Note that only pure quantum states correspond to points on the surface of the Bloch sphere. For a single qubit, rewriting the density operator (1.3) as

$$\hat{\rho} = \frac{1}{2}\left(\hat{\mathbb{1}} + \vec{b}\cdot\vec{\sigma}\right), \tag{1.4}$$
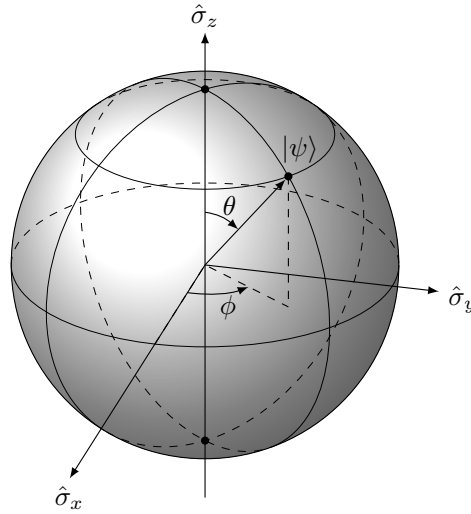
FIG. 1.1 – Pure qubit states are represented as points on the the surface of the Bloch sphere. The state is uniquely determined by the angles θ and ϕ. The axes correspond to eigenstates of the respective Pauli operators.

where $\vec{\sigma} = (\hat{\sigma}_x, \hat{\sigma}_y, \hat{\sigma}_z)^{\mathrm{T}}$ is the vector of Pauli matrices and $\hat{\mathbb{1}}$ the identity operator, enables to describe any single-qubit state in terms of the *Bloch vector* $\vec{b}$. Pure states will satisfy $|\vec{b}| = 1$ while for mixed states we have $|\vec{b}| < 1$, so that they correspond to points inside the Bloch sphere.

In a multi-qubit system, the computational basis states are formed by the product states of individual qubits. That is, for N qubits the computational basis is spanned by the states $|q_1\rangle \otimes |q_2\rangle \otimes \ldots \otimes |q_N\rangle \equiv |q_1 q_2 \ldots q_N\rangle$, where $q_j \in \{0, 1\}$ labels whether qubit j is in state $|0\rangle$ or $|1\rangle$.

1.2 Quantum Circuit Model

As classical computation is based on *gates* – logical operations on bits to process information – there exist *quantum gates* for quantum computation. We shall simply refer to them as *gates* as well. In classical information processing the NAND (inverted AND) gate is a *universal gate*: every classical algorithm can be decomposed solely in terms of NAND gates if FANOUT operations are available. A similar concept exists in quantum computation: The elements of a universal set of quantum gates are able to approximate any unitary operation to arbitrary accuracy. Different universal sets of quantum gates exist, but typically they consist of operations on single qubits as well as entangling two-qubit gates [16]. Two (or more) quantum systems are said to be *entangled* if their state cannot be described by a product state of the individual systems.

Single-qubit gates are parametrized as a rotation

$$\hat{R}(\alpha, \vec{n}) = \exp\left(-i\alpha\vec{n}\cdot\vec{\sigma}\right) = \cos(\alpha)\,\hat{\mathbb{1}} - i\sin(\alpha)\,\vec{n}\cdot\hat{\vec{\sigma}} \qquad (1.5)$$

of the qubit state $|\psi\rangle$ about an angle α around the axis defined by the unit vector $\vec{n}$ in the coordinate system of the Bloch sphere. Two-qubit gates are the quantum extension to classical conditional gates, such as the XOR. That is, a single-qubit gate is applied to one qubit (the *target*) conditioned on the state of another (the *control*). The quantum analog of the classical XOR gate is the controlled-NOT (CNOT) gate, which, in the basis $\{|00\rangle, |01\rangle, |10\rangle, |11\rangle\}$, reads

$$\text{CNOT} = \begin{pmatrix} 1 & 0 & 0 & 0 \\ 0 & 1 & 0 & 0 \\ 0 & 0 & 0 & 1 \\ 0 & 0 & 1 & 0 \end{pmatrix}. \qquad (1.6)$$

If starting in a computational basis state, it flips the state of the target qubit only if the control qubit is in state $|1\rangle$. Since quantum gates obey the laws of quantum mechanics, they are reversible – which is fundamentally different to classical gates, where only certain gates are invertible. The CNOT gate, together with single-qubit gates, forms a universal set of gates for quantum computation [17]. It is a perfectly entangling gate. That is, it is capable of creating the non-separable two-qubit Bell states $|\Phi^{\pm}\rangle = (|00\rangle \pm |11\rangle)/\sqrt{2}$ and $|\Psi^{\pm}\rangle = (|01\rangle \pm |10\rangle)/\sqrt{2}$ from two separable single-qubit states. For instance, together with the Hadamard gate

$$\text{H} = \frac{1}{\sqrt{2}} \begin{pmatrix} 1 & 1 \\ 1 & -1 \end{pmatrix}, \qquad (1.7)$$

it can be used to generate the maximally entangled Bell state $|\Phi^{+}\rangle$ from the input state $|00\rangle$. In order to visualize a sequence of quantum gates, that constitute an algorithm, they are drawn in the form of *quantum circuits*. An example of a particularly small quantum circuit that creates the Bell state $|\Phi^{+}\rangle$ is drawn in FIG. 1.2: Horizontal lines represent individual qubits and time evolves from left to right. In certain cases the qubit interactions do not allow for a direct implementation of the CNOT gate. Often, it is then possible to realize a controlled phase gate $C_Z = |00\rangle\langle00| + |01\rangle\langle01| + |10\rangle\langle10| - |11\rangle\langle11|$.
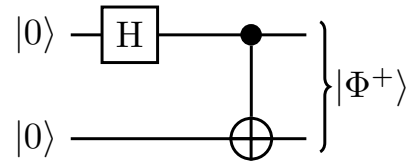
FIG. 1.2 – Quantum circuit that generates the Bell state $|\Phi^{+}\rangle$ using a Hadamard and CNOT gate. Horizontal lines represent qubits.

By applying a Hadamard gate before and after the C_Z gate, the CNOT can be recovered from the controlled phase gate.

In general, of course, quantum circuits become more involved and typically contain many different types of single- and two-qubit gates. Prominent examples of further perfectly entangling gates are the $\sqrt{\text{SWAP}}$ and iSWAP gates [16]. The concept of dividing a quantum algorithm into discrete gates, which much like classical Boolean circuits are visualized in quantum circuits, is known as the *quantum circuit model*. An alternative approach – adiabatic quantum computation – will be introduced in part III of the thesis.

1.3   The DiVincenzo Criteria

Section 1.1 introduced the basic mathematical concept behind qubits, followed by a short description of quantum gates and how (complex) quantum algorithms can be visualized in terms of quantum circuits. In order for a quantum computer based on the circuit model to work, its components need to satisfy the five DiVincenzo criteria [18, 19]:

1. **Identification of well-defined qubits:**
   Qubits – as introduced mathematically in the previous section – are in fact ideal or effective two-level systems. The computational basis states $\{|0\rangle, |1\rangle\}$ are often defined out of a larger Hilbert space and correspond to states of lower energy (*ground state*) and higher energy (*excited state*). The energy difference between ground and excited state is what will be referred to as the *qubit frequency*. Physically, qubits can be defined in a variety of different platforms which will be reviewed in chapter 2. It is crucial that the Hilbert space of the quantum system is precisely delineated and that the individual qubits can be isolated from others, in terms of control and measurement.

2. **Reliable state preparation:**
   Different algorithms require different initial conditions. Hence, it is inevitable to be able to prepare the set of qubits in a well-defined initial state. For instance, a common initial state is when all qubits are prepared in their ground state. The difficulty of how to prepare a qubit system in the respective states and also the technology to do so depends very much on the physical platform the qubits are built from.

3. **Low decoherence:**
   Decoherence processes limit the time over which a qubit can be used

for reliable quantum information processing. It originates from interactions between the qubit and its environment, which has two major effects: (i) *Relaxation*, where the qubit loses energy to the environment and as a consequence decays to its ground state, and (ii) *dephasing*, where a superposition of states loses a coherent relation of their phases and become mixed – eventually recovering classical behavior. In order to minimize decoherence errors, qubits are designed to suffer from decoherence as little as possible, and algorithms are supported by error correction schemes to account for certain errors [16].

4. **Accurate quantum gate operations:**
   It is not enough to be able to implement a single gate with low errors. In complicated quantum algorithms single- and two-qubit gates need to be accurate enough to be repeatedly used, so that accumulated errors will remain low enough in order for the outcome to be still reliable. Conventional estimates [20] state that the error per gate should be less than 10^{-4} to allow for fault-tolerant quantum computing, while modern error correction schemes tolerate errors of about 1% [21]. Often, instead of quantifying accuracy in terms of gate error, one uses the *fidelity F*. It is directly related to the gate error, which is defined as $1 - F$.

5. **Reliable quantum measurements:**
   Lastly, after applying all required gates, the final state of the qubit register needs to be measured to extract the outcome of the computation. Measurement schemes need to be fast enough so that the state is determined before decoherence renders the result unreliable.

In part II of this thesis, the central focus will be a study of how accurate quantum gate operations in different quantum systems can be realized. In parts, chapters 7 and 8 will also address the third DiVincenzo criterion.

The reader is directed to the textbook by Nielsen and Chuang [16] for further information on quantum computation and quantum information.

Chapter 2

Physical Implementations of Qubits

Over the past decades there has been a wide variety of proposals for hardware platforms suitable for quantum computing, such as solid state systems in form of superconducting qubits, and atomic systems in form of trapped ions and trapped neutral atoms. On top of the DiVincenzo criteria (see section 1.3), the ultimate goal to let the whole quantum system operate as a computer imposes another constraint: Technology needs to be scalable, and hence poses challenging problems to both science and engineering.

This chapter will briefly expand upon those platforms that are of particular relevance for this thesis. A more exhaustive analysis of different platforms and their current (fall 2017) state of the art can be found in Ref. [22] where the authors propose to divide the evaluation of quantum computers into five levels and rate current platforms according to these criteria: (A) Basic functionality, such as implementation of gates and readout, (B) quality of operations, (C) demonstration of quantum error correction, (D) demonstration of fault-tolerant operations and (E) the implementation of complex fault-tolerant algorithms.

2.1 Superconducting Qubits

Superconducting qubits are solid state systems that can be used in integrated electrical circuits. They are human-made and hence parameters such as qubit frequencies can be engineered at a wide range, in contrast to for instance atoms, where the energy levels are given by nature. This, however, has both advantages and disadvantages: For instance, while multiple qubits can be printed quite easily on a single chip, there will always be inhomogeneities in
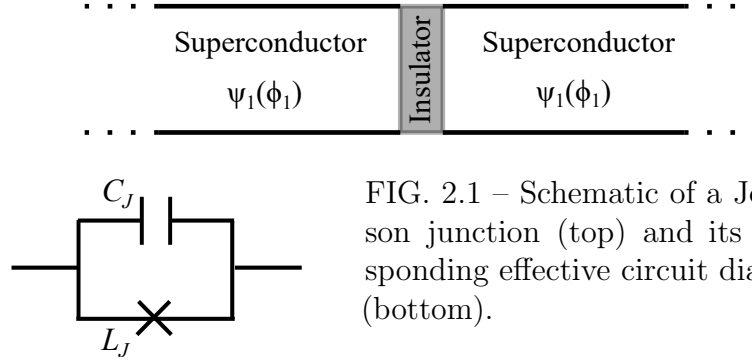
FIG. 2.1 – Schematic of a Josephson junction (top) and its corresponding effective circuit diagram (bottom).

the fabrication process, preventing the existence of exactly identical qubits. Superconducting qubits have been studied intensively in both theory and experiment over the last two decades. As a number of great reviews on the field already exist [23–27], we will briefly discuss the heart of each superconducting qubit – the *Josephson junction* – and then go over the basics of superconducting qubits.

2.1.1 Josephson Junction

It is well known that the Hamiltonian of a LC-resonator circuit resembles that of a harmonic oscillator, preventing it from being used as a qubit since energy levels are equidistant and hence a well-defined qubit subspace cannot be isolated. A nonlinear circuit element, the *Josephson junction*, breaks the degeneracy and thereby allows to isolate two qubit levels out of the resulting anharmonic oscillator.

As illustrated in FIG. 2.1, a Josephson junction is formed by two superconductors [28] separated by a thin insulating layer. The Cooper pairs in each of the superconductors are described by the wave functions $\psi_1(\phi_1)$ and $\psi_2(\phi_2)$. Owing to quantum mechanics, the Cooper pairs can tunnel through the insulating barrier, allowing for nonzero voltage V and current I across the tunnel junction. The dynamics of a Josephson junction are governed by the Josephson equations [29]

$$I = I_c \sin(\phi)\,, \tag{2.1}$$

$$V = \frac{\Phi_0}{2\pi}\dot{\phi}, \tag{2.2}$$

where $\phi = \phi_1 - \phi_2$ is the superconducting phase difference, $\Phi_0 = h/2e$ the magnetic flux quantum for superconductors and I_c the critical current of the junction. If the junction is biased with an external current above I_c superconductivity breaks down. Much like a LC-resonator circuit, the

Josephson junction can be thought of as a capacitor (capacitance C_J) in parallel to a nonlinear inductor (inductance L_J) [24].

2.1.2   Qubit Designs

Using the Josephson junction to form a qubit subspace, three basic designs of superconducting qubits emerged: (i) The *phase qubit* [30], where the Josephson junction is connected in series with a bias current and the qubit is formed by the ground and first excited state within a metastable well of a cosine washboard potential. (ii) The *flux qubit* [31], consisting of a superconducting loop that contains one or more Josephson junctions. Here, the qubit subspace is defined by (meta)stable states corresponding to opposite circulating currents in the loop. (iii) The *charge qubit* [32, 33], which is a Josephson junction connected in series with a capacitor of capacitance C_g and a voltage source V_g. The number of Cooper

FIG. 2.2 – Effective circuit diagram of a charge qubit.

pairs on the superconducting island, formed between the capacitor and the Josephson junction, defines the qubit states. Since the charge qubit is the basis for contemporary qubit designs, such as the Transmon [34] and the Xmon [35], we will briefly expand upon it here.

A schematic circuit diagram of the charge qubit is given in FIG. 2.2. In order to describe the charge qubit, a quantization of its circuit leads to the circuit Hamiltonian

$$\hat{H} = E_C \left(\hat{N} - N_g \right)^2 - E_J \cos(\hat{\varphi}) , \tag{2.3}$$

where the number of Cooper pairs $\hat{N} = \hat{Q}/2e$ equals the charge $\hat{Q}$ scaled by $1/2e$. The charge operator $\hat{Q}$ is conjugate to the phase $\hat{\varphi}$. In Hamiltonian (2.3) we have further introduced the charging energy $E_C = (2e)^2/2(C_g + C_J)$, the Josephson energy $E_J = \Phi_0 I_c$ and the gate charge number $N_g = -C_g V_g/2e$. The charging energy is the energy required to have an extra Cooper pair on the superconducting island, while the Josephson energy defines the energy a Cooper pair requires to tunnel across the junction.

The Hamiltonian is conveniently understood in terms of the eigenbasis of $\hat{N}$, that is $\hat{N}|n\rangle = n|n\rangle$. Owing to the nonlinearity of the Josephson junction, the Hamiltonian features an anharmonic spectrum. Hence, qubit states can be well-defined and addressed separately: Typically, the two lowest energy states form the qubit while higher states are the source of what will be later

referred to as *leakage* errors – excitations, and hence information loss, to states outside the computational subspace $\{|0\rangle, |1\rangle\}$. If the qubit is encoded in the ground and first excited state of Hamiltonian (2.3), the qubit frequency equals $E_C(1 - 2N_g)$ while the separation of first and second excited state is given by $E_C(3 - 2N_g)$. The difference between these transition energies, i.e. $2E_C$, is referred to as *anharmonicity*.

Taking into account that $\hat{N}$ and $\hat{\varphi}$ are conjugate variables, we find that $e^{i\hat{\varphi}}|n\rangle = |n+1\rangle$. We are then able to express Hamiltonian (2.3) in the Cooper pair number basis. If we restrict ourselves to the qubit subspace the Hamiltonian of the charge qubit becomes [36]

$$\hat{H}_{\text{cq}} = E_C \left(N_g - \frac{1}{2} \right) \hat{\sigma}_z - \frac{E_J}{2} \hat{\sigma}_x. \tag{2.4}$$

To achieve universal control of the qubit, nonzero Josephson energy and tunable N_g are required. Conventional charge qubits operate in the regime $E_C \gg E_J$ [23]. Their quality, particularly their coherence times, suffer from the direct dependence of qubit frequency on N_g, which is proportional to the gate voltage V_g. If there is noise in the voltage source, the qubit will dephase. This effect can be minimized by working at the charge degeneracy point where $N_g = 1/2$. Unfortunately, even only slightly away from the degeneracy point, the effect can be quite harmful and so improved variants of the charge qubit were developed.

Contemporarily used qubit designs, like the Transmon [34] and the Xmon [35], make use of an additional large capacitance shunted in parallel to the Josephson junction. This allows to operate the qubit in a regime where $E_J \gg E_C$ and decoherence errors from noise in the voltage source are reduced significantly, as substantiated by coherence times improving from a few nanoseconds [37] to about $100\mu s$ [38, 39] in only a decade. However, the downside of operating in the regime of large Josephson energy is that the qubit anharmonicity is decreased and hence leakage errors are enhanced. Yet, advanced control schemes exist [40, 41] so that superconducting Transmon and Xmon qubits remained state of the art at the time of writing.

Gates between multiple superconducting qubits can be established by connecting them with superconducting coplanar waveguides, serving both as resonators and transmission lines. The entire field of using such resonators is termed *circuit quantum electrodynamics* [42, 43], being the analog to the related field of *cavity quantum electrodynamics* [44]. Alternatively, tunable capacitive or inductive couplings between qubits can be used to mediate interactions [45, 46]. Yet, these tunable couplings are only used in specific applications, and instead resonance methods involving resonators are rather used for scalable quantum computation applications [47–49].

2.2   Trapped Ions

Based on the progress in gate fidelities [50, 51] and the experimental status
of error correction [52, 53], trapped ions currently belong – together with
superconducting qubits – to the most promising platforms for quantum com-
putation. After ionization, quantum states of single electrons in the outer
shell define the qubit. Hence, the choice of ions is restricted to the earth-alkali
group and some transition metals [54, 55]. For details on quantum compu-
tation with trapped ions the reader is referred to the literature [54, 56, 57].
Within this section we will focus on the necessary basics such as control, trap
designs and different types of qubits, and proceed to review more in depth
the ion dynamics in a linear Paul trap.

   In quantum information processing with trapped ions, there are two types
of qubits, distinguished by the states that constitute the computational sub-
space: The *optical qubit* and the *hyperfine qubit*.

1. **Optical qubit:**
   In an optical qubit the computational states correspond to fine structure
   levels of the trapped ion with an energy separation inside or close to
   the optical regime. The excited state must be as stable as possible to
   maintain coherence. A downside thereof is that strong single lasers are
   required to control the qubit. Prominent examples for ions that feature
   a forbidden direct optical transition and are typically used as optical
   qubits are $^{40}\mathrm{Ca}^+$, $^{88}\mathrm{Sr}^+$ and $^{138}\mathrm{Ba}^+$.

2. **Hyperfine qubit:**
   Ions with nonzero nuclear spin are qualified to be used as hyperfine
   qubits. Here, the computational states are encoded in the hyperfine sub-
   levels of a ground state, which makes them immune to decay and allows
   for coherence times on the order of 1000s [58]. Since direct transitions
   between the computational states are forbidden, gates are implemented
   using Raman lasers [59] that drive transitions via an intermediate third
   level with frequencies in or close to the optical range. Typical examples
   are ions of odd isotopes, such as $^9\mathrm{Be}^+$, $^{25}\mathrm{Mg}^+$ and $^{43}\mathrm{Ca}^+$.

Based on these two types of qubits, lasers in the optical regime are convention-
ally used to control the ions [60, 61]. While there has been significant progress
in terms of quantum information with trapped ions using laser controls, the
experimental setups become very involved and hence pose severe problems to
scale up the number of qubits by orders of magnitude to be compatible with
large-scale fault-tolerant algorithms. A potential solution has been brought
forward in form of using microwave/radio-frequency control [62–64], which
greatly simplifies the complexity of the experimental setups.

2.2.1 Trapping Technologies

Owing to their electrical charge ions are trapped using electrostatic potentials. However, as proven by Earnshaw's theorem [65], it is impossible to spatially stabilize an ion by solely using an electrostatic force. Using an additional time-dependent field allows for stabilized trapping of the ions by synchronizing the field to the motion of the ions. Since the synchronization of field and ion motion requires exact knowledge of the ion mass, the system needs to be isotopically pure. While there are many different types of traps, we restrict our discussion to the following three basic trap designs:

1. **Linear Paul trap:**
   The ions are trapped within a quadrupole geometry [66] and form a linear chain (details below). There is a limit on the number of ions that can be trapped and controlled coherently [67], given by the requirement that the minimal spacing between ions must be larger than the focal spot of the control lasers. It is expected that the current world record of 14 entangled ions [68] is probably operating at or very close to this limit.

2. **Penning trap:**
   In a Penning trap, ions are confined using a combination of a strong, homogeneous magnetic field and a static quadrupolar electric potential. It allows for 2D arrays of trapped ions with ~ 300 ions [69]. A notable disadvantage of the Penning trap is that individual addressability and control of the atoms can be very difficult [58].

3. **Surface traps:**
   Here, the ions are trapped by potentials (similar to Paul trap) generated via flat metallic surfaces [70]. By dividing the surface into multiple segments it is straightforward to manipulate only a subset of ions at a time. The planar electronic structure offers great prospects for scalability [71] and motivates development of 2D surface trap designs [72].

2.2.2 Dynamics in a Linear Paul Trap

After introducing the very basics of trapped ions we proceed to analyze the collective motion inside a linear Paul trap. The following description will follow work by James [73]. Let ω_α be the trap frequency in direction α. Then, for this particular trap design, stable confinement of ions along the z-axis requires $\omega_{x,y} \gg \omega_z$. Without loss of generality, we will further consider the situation of strong bounding in the x/y directions and therefore neglect all

motion along the corresponding axes. Nevertheless, we note that motion transverse to the ion chain can be a source of decoherence [74]. An additional source of error is given by phase transitions to ion configurations other than a linear chain, due to instable transverse modes. The probability for such phase transitions has been shown to grow with the number N of ions inside the trap [75]. We consider a linear trap with N ions of individual masses M along the z-axis. The trap potential in this case reads

$$V = \sum_{m=1}^{N} \frac{1}{2} M \omega_z^2 \left(z^{(m)}(t) \right)^2 + \sum_{\substack{n,m=1 \\ m \neq n}}^{N} \frac{Z^2 e^2}{8\pi\epsilon_0} \frac{1}{|z^{(n)}(t) - z^{(m)}(t)|}, \qquad (2.5)$$

where Z is the degree of ionization, e is the electron charge, ϵ_0 is the permitivity of free space and $z^{(m)}(t)$ the z-coordinate of ion m at time t. If we assume that each ion is sufficiently cooled, its motion is given by a fluctuation $q^{(m)}(t)$ around its fixed equilibrium position $z_0^{(m)}$, i.e. $z^{(m)}(t) \approx z_0^{(m)} + q^{(m)}(t)$.

Equilibrium positions in the chain

The equilibrium positions are determined by the minima of the trap potential V. That is, we need to find the roots of

$$\left. \frac{\partial V}{\partial z^{(m)}} \right|_{z^{(m)}=z_0^{(m)}} = 0. \qquad (2.6)$$

We introduce the typical length scale $l = (Z^2 e^2 / 4\pi\epsilon_0 \omega_z^2 M)^{1/3}$ of the ion-ion spacing and use it to define the dimensionless equilibrium positions $u^{(m)} \equiv z_0^{(m)}/l$. Expressing equation (2.6) in terms of dimensionless coordinates leads to the following system of $m = 1, \ldots, N$ coupled equations for the $u^{(m)}$:

$$u^{(m)} - \sum_{n=1}^{m-1} \frac{1}{\left(u^{(m)} - u^{(n)} \right)^2} + \sum_{n=m+1}^{N} \frac{1}{\left(u^{(m)} - u^{(n)} \right)^2} = 0 \qquad (2.7)$$

For up to three ions the system (2.7) can be solved analytically. The respective solutions for the equilibrium positions of $N = 3$ ions are given by

$$u^{(1)} = -\left(\frac{5}{4} \right)^{1/3}, \quad u^{(2)} = 0, \quad u^{(3)} = \left(\frac{5}{4} \right)^{1/3}. \qquad (2.8)$$

Numerical solutions for ion numbers $N > 3$ reveal that the ion-ion spacing grows with increasing distance from the center of the chain. The minimal distance between ions obeys the empirical relation $u_{\min}(N) \approx 2.018/N^{0.559}$ and poses limitations on the maximum number of trapped ions [67].

Fluctuations around the equilibrium

The Lagrangian of the ion system allows to determine the fluctuations $q^{(m)}(t)$ of ion m around its equilibrium. Using a second order Taylor expansion of the trap potential around the equilibrium positions we compute the Lagrangian to be

$$L = \frac{M}{2} \sum_{m=1}^{N} \left(\dot{q}^{(m)} \right)^2 - \frac{1}{2} \sum_{n,m=1}^{N} q^{(n)} q^{(m)} \left. \frac{\partial^2 V}{\partial z^{(n)} \partial z^{(m)}} \right|_{q^{(m)}=q^{(n)}=0} \tag{2.9}$$

$$= \frac{M}{2} \left[\sum_{m=1}^{N} \left(\dot{q}^{(m)} \right)^2 - \omega_z^2 \sum_{m,n=1}^{N} K_{nm} q^{(n)} q^{(m)} \right]. \tag{2.10}$$

The matrix elements K_{nm} are given by

$$K_{nm} = \begin{cases} 1 + 2 \sum_{\substack{j=1 \\ j \neq m}}^{N} \dfrac{1}{|u^{(m)} - u^{(n)}|^3} & , n = m \\[4mm] -\dfrac{2}{|u^{(m)} - u^{(n)}|^3} & , n \neq m. \end{cases} \tag{2.11}$$

Since the matrix K is real, symmetric and positive semidefinite it has non-negative eigenvalues μ_p associated to eigenvectors $\vec{b}^{(p)}$. The eigenvectors are defined by the relation $\sum_{n=1}^{N} K_{mn} b_m^{(p)} = \mu_p b_m^{(p)}$, where $b_m^{(p)}$ denotes the m-th element of the p-th eigenvector $\vec{b}^{(p)}$. As was the case for the equilibrium positions, analytical solutions to the eigensystem exist only for at most three trapped ions. For $N = 3$ ions, the motion is determined by the eigenvectors

$$\mu_1 = 1, \quad \vec{b}^{(1)} = (1, 1, 1)/\sqrt{3}, \tag{2.12}$$

$$\mu_2 = 3, \quad \vec{b}^{(2)} = (1, 0, -1)/\sqrt{2}, \tag{2.13}$$

$$\mu_3 = \frac{29}{5}, \quad \vec{b}^{(3)} = (1, -2, 1)/\sqrt{6}, \tag{2.14}$$

which correspond in order to the *center of mass (COM)* mode, *breathing* mode (also *stretch* mode) and *Egyptian* mode of the chain. The associated mode frequencies are given by $\omega_{z,p} = \sqrt{\mu_p} \omega_z$. In the COM mode all ions move in the same direction with identical amplitude, while for the breathing mode the inner ion is at rest and the outer ions oscillate with equal amplitude in opposite direction. The Egyptian mode describes a vibrational state of the chain where the inner ion moves out of phase and with twice the amplitude as both outer ions.

Quantum motion of the ions

A second quantization of the ions' motion is possible by first moving to normal mode coordinates of the chain, i.e. using $Q_p(t) = \sum_{m=1}^{N} b_m^{(p)} q^{(m)}(t)$. We now express the normal mode coordinates through the respective harmonic lowering and raising operators $\hat{a}$ and $\hat{a}^\dagger$, respectively, to obtain the expression

$$\hat{q}^{(m)}(t) = \sqrt{\frac{\hbar}{2M\omega_z}} \sum_{p=1}^{N} s_m^{(p)} \left(\hat{a}_{z,p} e^{-i\omega_{z,p}t} + \hat{a}_{z,p}^\dagger e^{i\omega_{z,p}t} \right) \qquad (2.15)$$

for the fluctuation of ion m in second quantization. Here, we introduced the quantity $s_m^{(p)} = b_m^{(p)}/\mu_p^{1/4}$ and used the following representation for position and momentum operators:

$$\hat{Q}_p = \sqrt{\frac{\hbar}{2M\omega_{z,p}}} \left(\hat{a}_{z,p}^\dagger + \hat{a}_{z,p} \right), \qquad (2.16)$$

$$\hat{P}_p = i\sqrt{\frac{\hbar M\omega_{z,p}}{2}} \left(\hat{a}_{z,p}^\dagger - \hat{a}_{z,p} \right), \qquad (2.17)$$

They obey the canonical commutation relation $\left[\hat{Q}_p, \hat{P}_q \right] = i\hbar\delta_{pq}$ and constitute the Hamiltonian describing the quantum motion of N ions in a linear Paul trap,

$$\hat{H}_{\text{Paul}} = \frac{1}{2M} \sum_{p=1}^{N} \hat{P}_p^2 + \frac{M}{2} \sum_{p=1}^{N} \omega_{z,p}^2 \hat{Q}_p^2. \qquad (2.18)$$

Hamiltonian (2.18) is the sum of N harmonic oscillators, each with frequency $\omega_{z,p}$. It turns out that the vibrational modes of the ion chain can be used to generate entanglement between different ions [76, 77]. An alternative approach to couple trapped ions involves long-range photonic links [54].

2.3 Rydberg Atoms

Rydberg atoms belong to the field of neutral atoms and hence, in contrast to ions, cannot be trapped using electrostatic potentials. Instead, neutral atoms are trapped in optical lattices formed by light-induced forces [78, 79]. More precisely, Rydberg atoms are atoms with large outer shell radii that are excited to quantum states with large principal quantum numbers. Their physics is well understood and excellently discussed in Gallagher's textbook [80].
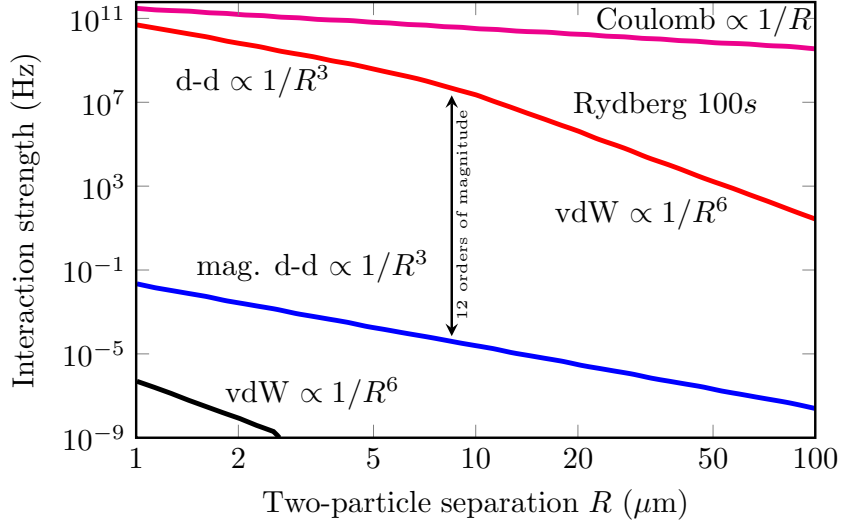
FIG. 2.3 – Two-body interaction strength as a function of particle separation R for Rb atoms in their ground state, Rb atoms excited to the $100s$ Rydberg state and Coulomb interaction between ions. Power laws for van der Waals (vdW) forces, magnetic dipole-dipole (mag. d-d) interactions and dipole-dipole (d-d) couplings are indicated. Recreated with permission from [81]. Copyright (2010) by the American Physical Society.

A special feature of Rydberg atoms which makes them of interest for quantum information processing is their strong long-range interaction [81]. Let us focus on the interaction of two particles separated spatially by distance R: For neutral atoms in their ground state the interaction for $R \lesssim 30$nm is dominated by $1/R^6$ van der Waals forces, while for larger separations magnetic dipole-dipole interactions $\propto 1/R^3$ dominate. For $R \gtrsim 1\mu$m the interaction strength falls below 0.1Hz. However, if the atoms are excited to Rydberg s-states with principal quantum number $n = 100$, the interaction between the particles is about twelve orders of magnitude larger than if they are in their ground states, as illustrated in FIG. 2.3. As such, Rydberg atoms have the great advantage of exceptional on-off-rations in their couplings, based on excitation and de-excitation of their quantum states. This is in contrast to for instance trapped ions, where a strong Coulomb interaction on the order of 10^{11}Hz for $R = 1\mu$m is always present.

As can be done for trapped ions, qubit states in Rydberg atoms are typically encoded in hyperfine sublevels. Common examples of Rydberg atoms used in quantum information are Rb and Cs. For a detailed review about how Rydberg atoms can be used for quantum information processing the reader is referred to [81]. Similar to trapped ion systems, Raman lasers near

or in the optical regime can be used to control Rydberg atom qubits [82, 83].
Additionally, control schemes based on microwaves [84], and a combination
of microwaves and gradient fields [85, 86] have been proposed.

Unfortunately, compared with superconducting qubits and trapped ions,
quantum gates with Rydberg atoms lack accuracy: Recent implementations
of single-qubit gates feature errors slighlty below 1% [87, 88]. However, gate
errors for multi-qubit gates are significantly worse. In advanced experimental
setups, two-qubit gate errors after accounting for certain known error sources
barely undercut values of 20% [89–91]. A detailed review of progress and
challenges of quantum computation with neutral atom qubits is provided by
Saffman [92]. Besides intrinsic limits on the fidelities of multi-qubit gates
there are multiple experimental issues. Examples for most relevant issues in
experiments with neutral atoms are Doppler dephasing, laser noise and atom
loss during the operations.

There exist different approaches to generate entanglement between trapped
Rydberg atoms [81, 92]. Examples thereof are (i) Rydberg dressing [90, 93],
where entanglement is generated via local spin exchange, (ii) dissipative entan-
glement [94, 95], where a combination of coherent and dissipative dynamics
(see chapter 3 for details on dynamics of quantum systems) is used to prepare
entangled states, and (iii) the Rydberg blockade [96–98], which is an effect
based on the strong long-range interaction between Rydberg atoms. Entan-
glement generation via the Rydberg blockade mechanism is an essential part
of the thesis and will be discussed in detail in chapter 7.

2.4 Other Candidates

Besides superconducting qubits, trapped ions and neutral atoms there are
other hardware platforms that are potentially suitable for building future
quantum computers. This section gives a superficial overview of these candi-
dates and points to relevant literature for more information. In general, the
remaining candidates can be categorized into semiconductor-based, photonic
and molecular platforms.

1. **Semiconductors:**
   Since semiconductors are of enormous industrial importance, fabrication
   and miniaturization has been perfected over the years and hence sub-
   stantiates the great potential of these platforms for large-scale quantum
   computing. The semiconductor platform can be divided into three main
   types: (i) *Quantum dots* [19, 99], where trapped single electrons act as
   artificial atoms and their spin is used as a qubit. Operation of quantum
   dots shares some similarities with superconducting qubit circuits. (ii)

Color centers, referring to isolated defects in artificial diamond crystals [100, 101]. The diamond crystal serves as a trap for defects with nuclear and electronic degrees of freedom that can be operated similar to trapped ions. (iii) *Donor qubits* in Silicon [102, 103], where strongly bound electrons around single isolated dopants or defects in the material can be used to encode qubits.

2. **Photonic platforms:**
   Aside from being used for control and communication channels in quantum systems, photons can also be used to host quantum information [104]. A fundamental challenge, however, is that there is no interaction between photons and hence multi-qubit gates cannot be implemented directly. Strategies to circumvent this limitation by simulating the required interactions involve special media, measurements or post-processing [105, 106]

3. **Molecules:**
   Nuclear magnetic resonance (NMR), where the qubit is encoded in a nuclear spin 1/2, was one of the first candidates for quantum computing [107, 108]. Yet, scalability is severely limited and it is hence no longer pursued as a serious candidate for quantum information [109].

Chapter 3

Dynamics of Quantum Systems

In order to model and understand the dynamics of quantum systems it is necessary to formulate equations of motions that accurately incorporate all relevant effects. A fundamental criterion that differentiates between two approaches is the existence of couplings between the quantum system and its environment. If such couplings do not exist – or at least are negligible for the time window of interest – the quantum system may be considered a *closed* system, which we will briefly review in the subsequent section 3.1. If couplings to an environment are relevant and can no longer be neglected, the system is referred to as an *open* quantum system. Section 3.2 gives an overview of two methodologies that provide equations of motions for such open systems.

3.1 Closed Quantum Systems

The dynamics of a closed quantum system, often referred to as *coherent* or *unitary*, are solely governed by its Hamiltonian $\hat{H}$. The equation of motion for a specific quantum state $|\psi\rangle$ is given by the Schrödinger equation $i\partial_t |\psi\rangle = \hat{H} |\psi\rangle$ (the convention $\hbar \equiv 1$ is used in this thesis) with some initial condition $|\psi(t_0)\rangle = |\psi_0\rangle$. Equivalently, but more common for applications that we will study in part II of the thesis, the Schrödinger equation is rephrased in terms of the unitary time evolution operator (the *propagator*) $\hat{U}(t)$,

$$\partial_t \hat{U}(t) = -i\hat{H}(t)\hat{U}(t), \quad \hat{U}(0) = \hat{\mathbb{1}}. \tag{3.1}$$

An equivalent way of representing the equation of motion is the von Neumann equation: It describes the evolution in terms of the system's density operator that we introduced in equation (1.3). The von Neumann equation reads

$$\dot{\hat{\rho}}(t) = -i[\hat{H}(t), \hat{\rho}(t)], \quad \hat{\rho}(t_0) = \hat{\rho}_0, \tag{3.2}$$

where $[\hat{A}, \hat{B}] = \hat{A}\hat{B} - \hat{B}\hat{A}$ is the commutator of $\hat{A}$ and $\hat{B}$, and $\hat{\rho}_0$ the initial state of the system at time t_0. Often, the dynamics dictated by equation (3.1) can be greatly simplified by moving to a different basis, for instance to remove fast intrinsic oscillations from the Hamiltonian. We denote such a unitary, generally time-dependent, transformation by $\hat{V}(t)$. It transforms Hamiltonian $\hat{H}$ according to

$$\hat{H}_v = \hat{V}^\dagger \hat{H} \hat{V} + i\dot{\hat{V}}^\dagger \hat{V}. \tag{3.3}$$

We will further refer to the original frame as the *lab frame* and label operators in the new frame with a subscript v. The form of the Schrödinger equation is invariant under transformation (3.3), and the propagator $\hat{U}(t) = \hat{V}(t)\hat{U}_v(t)\hat{V}^\dagger(0)$ in the lab frame can directly be recovered from that in the new basis.

3.2 Open Quantum Systems

While it is theoretically more convenient to focus on closed systems, in experiments it is often insufficient and instead couplings between a quantum system and its environment need to be considered. In principle "the system" could be enlarged such that it includes all relevant parts that participate in the interaction. However, aside from the huge overhead that would be required, often a mathematical model to describe the enlarged system does not exist. But even if it did, solving the full equations of motions of such an enlarged system is often simply impossible.

Instead, it is favorable to derive effective equations of motion – so-called *master equations* – for the quantum system. These master equations take into account all relevant interactions but do not require to solve for the generally irrelevant evolution of the environment. In quantum mechanics, two common methods to study the dynamics of open quantum systems are the Lindblad master equation and the Bloch-Redfield master equation, which we will briefly discuss here, since both are of particular importance for chapters 7 and 10, respectively.

3.2.1 Lindblad Master Equation

The evolution of a system state $\hat{\rho}_Q(t)$, confined to the quantum system of interest, according to the Lindblad master equation is subject to the differential equation

$$\dot{\hat{\rho}}_Q(t) = -i[\hat{H}(t), \hat{\rho}_Q(t)] + \sum_r \gamma_r \left(\hat{L}_r \hat{\rho}_Q(t) \hat{L}_r^\dagger - \frac{1}{2} \left\{ \hat{L}_r^\dagger \hat{L}_r, \hat{\rho}_Q(t) \right\} \right), \tag{3.4}$$

where $\{\hat{A}, \hat{B}\} = \hat{A}\hat{B} + \hat{B}\hat{A}$ is the anticommutator of $\hat{A}$ and $\hat{B}$. The first term in equation (3.4) corresponds to the coherent dynamics – the von Neumann equation (3.2) – while the second term of equation (3.4) gives rise to dissipative dynamics due to the environment. The Lindblad operators $\hat{L}_r$ describe incoherent transitions with Lindblad rates $\gamma_r > 0$. For a detailed discussion of the underlying quantum dynamical semigroup the reader is referred to [110].

The Lindblad master equation is very instructive to use and hence has a wide range of applications. A detailed derivation of the Lindblad form (3.4) is given in the excellent textbook by Breuer and Petruccione [111]. We will briefly discuss the underlying assumptions and approximations that are key to the derivation:

1. **Separability:** It is assumed that at initial time t_0 there are no correlations between the quantum system and its environment. Hence, the full density matrix is the tensor product $\hat{\rho}(t_0) = \hat{\rho}_Q(t_0) \otimes \hat{\rho}_{\mathrm{env}}(t_0)$.

2. **Born approximation:** The Born approximation states that throughout the evolution, the full density matrix remains separable, i.e. $\hat{\rho}(t) \approx \hat{\rho}_Q(t) \otimes \hat{\rho}_{\mathrm{env}}$. In other words, the interaction of system and environment must not change the state of the environment significantly. This is valid for weak couplings, and if the environment is much larger than the system.

3. **Markov approximation:** This states that the environment does not have a memory effect. That is, the evolution of the state at time t only depends on the state at that particular time. It requires that the timescale τ_{env} of correlations with the environment is much shorter than than any relevant timescale τ_Q of the system.

4. **Secular approximation:** The secular approximation amounts to neglecting rapidly oscillating terms. More specifically, terms with transition frequencies $|\omega| \ll 1/\tau_Q$ are neglected.

Note that the Lindblad master equation (3.4) is constructed such that it properly describes a physical process. That is, it preserves fundamental properties of the density operator (i.e., trace and positivity). However, a direct connection to a microscopic model of the interactions between the system and its environment is intractable with the Lindblad formalism. While the Lindblad operators and rates often correspond to intuitive physical phenomena such as dephasing and relaxation, they are still somewhat arbitrary parameters of the model.

3.2.2 Bloch-Redfield Master Equation

As opposed to the Lindblad formalism described above, the Bloch-Redfield formalism derives the equations of motion from a microscopic model and thereby allows to relate components of the resulting master equation to fundamental physical properties, such as the spectral density of the environment. The Bloch-Redfield master equation, derived under assumptions (1)-(3) used in the Lindblad formalism above, reads [111]

$$\dot{\hat{\rho}}_Q(t) = -\int\limits_{t_0}^{\infty} \mathrm{d}s \, \mathrm{Tr}_{\mathrm{env}} \left\{ [\hat{H}_{QB}(t), [\hat{H}_{QB}(t-s), \hat{\rho}_Q(t) \otimes \hat{\rho}_{\mathrm{env}}]] \right\}. \qquad (3.5)$$

Here, $\hat{H}_{QB}(t)$ is the coupling Hamiltonian between the system and its environment, given in the interaction picture defined by the bare system and environment Hamiltonian. By tracing out the environmental degrees of freedom, microscopic effects such as the noise-power spectrum of the environment enter the equations of motions through environmental correlation functions. The Bloch-Redfield master equation (3.5) can be brought into the Lindbladian form (3.4) if the secular approximation is applied [111].

Part II

Optimal Control Theory

Chapter 4

Introduction to Optimal Control Theory

Control theory addresses the task of controlling systems such that a desired result is achieved. A prominent example from engineering is cruise control of a car: It needs to set some control variable (i.e., the power provided by the engine) such that the target velocity specified by the driver is kept constant. If the solution to the control problem also needs to ensure optimality with respect to another quantity, for instance fuel consumption, *Optimal Control Theory* (OCT) provides a framework to find adequate solutions, and to generally answer the question of controllability, of such a control task.

The central focus of this part of the thesis will be to find efficient solutions to drive different quantum systems into a desired target or along a certain trajectory. Steering quantum systems, that is engineering a specific time-evolution (see chapter 3), in a well-controlled manner with the aid of OCT is a fundamental problem that lies at the heart of currently emerging quantum technologies [112]. While OCT is commonly used in quantum information processing [113] it has a wide range of applications in other fields. For instance, it is regularly used in nuclear magnetic resonance [114], spectroscopy [115], sensing and metrology [116], but also has applications in biodynamics, where it can be used to control the energy flow in biomolecules [117]. Two basic requirements for OCT to work is that (i) a controllable set $\vec{u}$ of functions u_j exist and (ii) that the performance of the process can be quantified in terms of a scalar *fidelity* function. A typical example of the controls u_j in the field of superconducting qubits are electromagnetic fields that are shaped in time, in order to drive desired single- or multi-qubit gates.

4.1   Fidelity Measures

A fidelity function defines a figure of merit to measure the quality of some quantum evolution, induced by a set of control fields applied to the system. Different fidelity functions exist [114, 118–122], each of them designed to be particularly suited for certain systems and certain applications. The optimal control problems we will discuss throughout part II of this thesis focus on the implementation of different unitary gates, as well as state generation in dissipative environments, and we will now introduce two fidelity functions that (or similar forms thereof) are commonly used for these purposes.

In case of coherent dynamics, where the unitary propagator $\hat{U}$ is accessible, we can use the gate overlap fidelity [114]

$$F_1 = \frac{1}{d^2} \left| \mathrm{Tr} \left(\hat{\mathbb{P}}_{\mathcal{Q}} \hat{U}_t^{\dagger} \hat{\mathbb{P}}_{\mathcal{Q}} \hat{U}(t_g) \right) \right|^2 \tag{4.1}$$

to quantify the overlap between the gate $\hat{U}(t_g)$ that was actually implemented by the applied set of controls, and the target gate $\hat{U}_t$. The projector $\hat{\mathbb{P}}_{\mathcal{Q}}$ allows to consider only the d-dimensional subspace $\mathcal{Q}$ of interest. For instance, when the qubit is encoded in a nonlinear oscillator (see section 2.1), we are often only interested in the final dynamics within its computational subspace $\mathcal{Q}$, spanned by the states $\{|0\rangle, |1\rangle\}$. By construction, the gate overlap fidelity (4.1) satisfies $0 \leq F_1 \leq 1$, whereby $F_1 = 1$ corresponds to the best possible result.

For dissipative dynamics a unitary propagator does not exist and hence it is impossible to use the gate overlap fidelity (4.1). Instead, performance can be quantified in terms of the state overlap fidelity [123]

$$F_2 = \left(\mathrm{Tr}_{\mathcal{Q}} \left\{ \sqrt{\sqrt{\hat{\rho}(t_g)} \hat{\rho}_t \sqrt{\hat{\rho}(t_g)}} \right\} \right)^2, \tag{4.2}$$

where $\hat{\rho}_t$ is the target state, $\hat{\rho}(t_g)$ the state that is actually implemented and $\mathrm{Tr}_{\mathcal{Q}}\{\hat{O}\}$ denotes the partial trace of operator $\hat{O}$ over the subspace $\mathcal{Q}$ of interest (comparable to the projection $\mathbb{P}_{\mathcal{Q}}$ for F_1). Note that, in contrast to the gate overlap fidelity (4.1), the state overlap fidelity (4.2) is applicable for both coherent and incoherent dynamics. However, if the propagator is accessible *and* gradient information is used during the optimization, it is more convenient to use the gate overlap (4.1).

4.2   Optimization Algorithms

In order to improve the fidelity function, i.e. to minimize the error, the control fields $\vec{u}$ are updated iteratively in numerically assisted methods. There exists a vast variety of optimization algorithms which can be fundamentally differentiated by whether they make use of derivatives of the fidelity function or not. Common examples of direct search methods, that is derivative-free optimization routines, are Simulated Annealing [124], Covariance Matrix Adaption Evolution Strategy (CMA-ES) [125] and Nelder-Mead [126]. In contrast, methods such as Sequential Quadratic Programming (SQP), interior point methods [127], Limited-memory Broyden-Fletcher-Goldfarb-Shanno (L-BFGS) [128] or Gradient Ascent Pulse Engineering (GRAPE) [114] explicitly use derivatives of the fidelity function to update the parameters.

While direct search methods tend to converge slower than gradient-based ones, they are typically more tolerant to noise and are hence used for closed-loop optimizations to calibrate pulse sequences in experiments [129, 130]. Regardless of the specific choice a good OCT method should satisfy three basic criteria: Speed, accuracy and flexibility. That is, it needs to be able to find simple high-fidelity solutions in a realistic experimental model, in reasonable time [131].

The above description refers to numerically assisted OCT. Instead, in certain situations it is also possible to design optimized control fields analytically, without additional numerical support. A prominent technique to derive analytic controls will be detailed in chapter 6. We now briefly discuss two common numerically assisted algorithms.

4.2.1   Nelder-Mead

The Nelder-Mead algorithm is a method designed to minimize a function $f : \mathbb{R}^n \to \mathbb{R}$ of n variables. It compares the function values at $(n + 1)$ vertices $\vec{x}_1, \vec{x}_2, \ldots, \vec{x}_{n+1}$ that themselves form a general *simplex*. The simplex iteratively adjusts to the local landscape and ultimately contracts to a local minimum of the function f.

In its original version [126] three operations are used to manipulate the simplex: *Reflection*, *contraction* and *expansion*. Advanced versions of the Nelder-Mead algorithm additionally use a *shrink* operation [132, 133]. The details of each step depend on the constant parameters $c_r > 0$ (reflection), $c_e > 1$ (expansion), $0 < c_c < 1$ (contraction) and $0 < c_s < 1$ (shrink). At each iteration the vertices are ordered with respect to their associated function

values

$$f_1 \leq f_2 \leq \ldots \leq f_{n+1}, \tag{4.3}$$

where we use the notation $f_j \equiv f(\vec{x}_j)$. In that ordering, $\vec{x}_1$ and $\vec{x}_{n+1}$ are referred to as the *best* and *worst* vertices, respectively. The *centroid* of the best n vertices is defined as $\bar{x} \equiv \sum_j \vec{x}_j/n$. Following Ref. [133] each iteration of the Nelder-Mead algorithm contains the following steps:

1. **Sort:** Evaluate the function values at all $(n + 1)$ vertices and sort according to relation (4.3)

2. **Reflect:** Compute the reflection $\vec{x}_R = \bar{x} + c_r(\bar{x} - \vec{x}_{n+1})$ and evaluate f_R. If $f_1 \leq f_R < f_n$, replace $\vec{x}_{n+1}$ with $\vec{x}_R$.

3. **Expand:** If $f_R < f_1$ compute the expansion $\vec{x}_E = \bar{x} + c_e(\vec{x}_R - \bar{x})$ and evaluate f_E. If $f_E < f_R$, replace $\vec{x}_{n+1}$ with $\vec{x}_E$. Otherwise, replace $\vec{x}_{n+1}$ with $\vec{x}_R$.

4. **Contract:** (i) If $f_n \leq f_R < f_{n+1}$, compute the *outside contraction* $\vec{x}_{OC} = \bar{x} + c_c(\vec{x}_R - \bar{x})$ and evaluate f_{OC}. If $f_{OC} \leq f_R$, replace $\vec{x}_{n+1}$ with $\vec{x}_{OC}$. Otherwise, go sto step 5. (ii) If $f_R \geq f_{n+1}$, compute the *inside contraction* $x_{IC} = \bar{x} - c_c(\vec{x}_R - \bar{x})$ and evaluate f_{IC}. If $f_{IC} < f_{n+1}$, replace $\vec{x}_{n+1}$ with $\vec{x}_{IC}$. Otherwise, go to step 5.

5. **Shrink:** Redefine the vertices according to $\vec{x}_j = \vec{x}_1 + c_s(\vec{x}_j - \vec{x}_1)$ for $2 \leq j \leq n + 1$.

As such, the Nelder-Mead algorithm allows to optimize control parametrizations that can be chosen to fit experimental needs. Thereby, it already satisfies one of the three criteria for a good OCT method. However, Nelder-Mead optimizations do not generally feature speed and high accuracy since, for rather complex problems, it tends to easily get stuck in local traps inside the optimization landscape.

4.2.2 Gradient Optimization of Analytic Controls

A novel method that is believed to meet all three criteria described above is reviewed in this subsection. It is based on simple analytic parametrizations that can be chosen to accurately model experimental capabilities and uses a gradient-based optimization routine, giving rise to the name *Gradient Optimization of Analytic conTrols* (GOAT) [131].

In order to better understand gradient-based optimization in quantum systems, we will now briefly discuss the core idea of the GOAT algorithm. It is convenient to decompose the total Hamiltonian

$$\hat{H}(\vec{x}, t) = \hat{H}_0 + \sum_k u_k(\vec{x}, t)\hat{H}_k \qquad (4.4)$$

into a non-controllable drift Hamiltonian $\hat{H}_0$ and a set of control Hamiltonians $\hat{H}_k$. The control functions u_k are characterized by a set of parameters $\vec{x}$. If, for instance, a Fourier parametrization is chosen, the parameters $\vec{x}$ correspond to amplitudes, frequencies and phases of all Fourier components. The specific choice of the parametrization is mainly determined by experimental constraints, but also taking into account that generally a solution with fewer parameters is preferable since it is easier to calibrate.

For the purpose of the discussion here, we will focus on the implementation of a target gate $\hat{U}_t$ within a given gate time t_g. As a figure of merit, we pick the gate error (also *infidelity*) g which is given by

$$g(\vec{x}) = 1 - \frac{1}{d}\left|\mathrm{Tr}\left(\hat{U}_t^\dagger \hat{U}(\vec{x}, t_g)\right)\right|. \qquad (4.5)$$

Note the similarity to the overlap fidelity (4.1). The task of OCT is to minimize infidelity g by finding an optimal set of parameters $\vec{x}$. In order for the optimization algorithm to be efficient, i.e. to meet the speed criterion, it needs to be able to efficiently compute the gradient $\partial_{\vec{x}} g(\vec{x})$ of the goal function. The sought gradient is found to be [131]

$$\partial_{\vec{x}} g(\vec{x}) = -\,\mathrm{Re}\left\{\frac{g^*}{|g|}\frac{1}{d}\mathrm{Tr}\left(\hat{U}_t^\dagger \partial_{\vec{x}}\hat{U}(\vec{x}, t_g)\right)\right\}. \qquad (4.6)$$

By swapping derivative orders, we obtain a coupled system of differential equations for $\hat{U}(\vec{x}, t_g)$ and its gradients from Schrödinger's equation (3.1),

$$\partial_t \begin{pmatrix} \hat{U} \\ \partial_{\vec{x}}\hat{U} \end{pmatrix} = -i \begin{pmatrix} \hat{H} & 0 \\ \partial_{\vec{x}}\hat{H} & \hat{H} \end{pmatrix} \begin{pmatrix} \hat{U} \\ \partial_{\vec{x}}\hat{U} \end{pmatrix}. \qquad (4.7)$$

An optimization process with GOAT will start at some initial set of parameters $\vec{x}_0$, which can either be a random or educated guess, and initiate any gradient-based optimization routine such as L-BFGS [128] to minimize the goal function (4.5). The required solutions to the coupled ordinary differential equations (ODE) (4.7) can be computed by any suitable ODE integrator, for instance an adaptive Runge-Kutta method. The search algorithm will iteratively update the parameters $\vec{x}$ based on evaluations of equations (4.5)

and (4.6) until a requested threshold is reached, or no further improvement is possible.

More details on the GOAT algorithm, particularly how it compares to other methods, and why it is believed to be the first OCT algorithm that meets all three criteria speed, accuracy and flexibility, can be found in [131].

4.3 Propagation Methods

While optimal control is in principle independent of the choice of propagation method, the final method of choice can have a major effect on the feasibility of optimizing a high-dimensional system. Two quantities which one should consider are the highest occupied energy level, which determines the rate at which the state's phase oscillates, and the highest frequency component of the Hamiltonian's time dependence.

A piecewise constant (PWC) propagator [114, 118], which explicitly exponentiates the Hamiltonian at every time step, is preferred when the control fields are slow compared to the phase oscillations, and the exponential naturally takes accurate care of the latter. Instead of PWC propagation, the equations of motion may also be solved using standard ODE propagators, such as adaptive Runge-Kutta methods. These are typically preferred when the field oscillations are the fastest varying component of the state. Appendix 8.A provides details of PWC propagation.

Chapter 5

Nonadiabatic Corrections

In many branches of physics and other natural sciences, analyzing dynamics of certain systems of interest can often be vastly simplified if it is possible to separate timescales, as is possible for a spinning top: It spins at a high frequency whereas its precession frequency is usually much lower. Often, it is then advantageous to apply frame transformations that separate the subspace of interest from the rest, such as separating a low-energy(frequency) subspace from a high-energy(frequency) subspace. A prominent and well-celebrated technique in quantum physics is the Schrieffer-Wolff transformation [134] which is named after the authors of a famous condensed matter paper [135] that relates the Anderson Hamiltonian to the Kondo Hamiltonian. In fact, the transformation has already been used multiple times many years before – for instance in order to study the dynamics of rotating molecules [136], which is why the method is also known as *van Vleck perturbation theory*. To our knowledge, the first application in quantum physics was about 15 years before Ref. [135] in Foldy's and Wouthuysen's work about the Dirac theory of spin 1/2 particles [137]. However, for convenience, we will refer to the technique as Schrieffer-Wolff transformation (SWT). A related method, so-called *adiabatic perturbation theory* [138, 139], perturbatively extends the adiabatic approximation (see chapter 6) in order to solve the effective dynamics of Hamiltonians that feature such a separation of scales.

Currently, applications of the SWT are countless. Apart from the examples mentioned before, it is widely used in quantum many-body systems. The SWT can for instance be used to study electron gases [140] and the ground state of the Hubbard model [141], but it has also become an important tool in

---

quantum information theory. For instance, it aids the understanding of the dispersive interaction in circuit quantum electrodynamics [43, 142, 143] within the framework of superconducting qubits [26] coupled through a resonator [144].

An important property of the SWT is that the eigenvalues of the derived effective Hamiltonian reproduce those of the full Hamiltonian (in the relevant subspace) to the required order of approximation. It may happen that the derived effective Hamiltonian has fewer degrees of freedom than the full Hamiltonian while featuring a more complex structure. This has eventually inspired the idea of perturbative gadgets [145, 146], where the SWT is used to analyze and construct high-energy simulator Hamiltonians with a low degree of complexity, that are used to approximate complex low-energy dynamics of some target Hamiltonian [147].

With ongoing technical developments, real-time control of quantum systems – in terms of shaped pulses for instance found via OCT, as introduced in chapter 4 – has become an important tool in quantum information to assess new degrees of controllability. However, applications of real-time control are not only limited to quantum information processing [148]. Possible other examples are quantum quenches in many-body systems, where a Hamiltonian is suddenly changed non-adiabatically [149], or fast tuning of qubit frequencies [150, 151]. Frequency-tuning of superconducting qubits is typically done by changing the magnetic flux penetrating the Josephson junctions [152], as we will explain in section 5.2. This method is quite sensitive to flux noise, which is why fast real-time flux control has so far been a difficult task. Yet, recent developments of a new qubit design [153], called the *Gatemon*, allows for fast frequency-tuning by manipulating voltage [154] instead of magnetic flux, so that fast frequency sweeps are easily possible.

In this chapter, we briefly review the idea of the SWT and present a general extension of the method incorporating time-dependent effects, which is inevitable given the imminent implementation of real-time controls. Goldin and Avishai [155] have used a time-dependent analogue of the SWT to study time-dependent impurities in Anderson and Kondo models. We adapt the idea of constructing a time-dependent Schrieffer-Wolff transformation (TDSWT) and present the full hierarchy of the approximation. Performing a second order perturbation theory ultimately reveals that the TDSWT adiabatically eliminates terms in the Hamiltonian that originate in real-time control. A similar idea of frame transformations has been used to adiabatically eliminate leakage errors in anharmonic ladder systems [40], such as superconducting qubits, but has – in a generalized version – for instance also shown promise to reduce errors in Rydberg gates [98]. Both applications will be detailed in chapters 6 and 7, respectively. By way of example we reconsider the dispersive

transformation of a Jaynes-Cummings type Hamiltonian for arbirarily many multilevel systems, taking into account that the energy levels as well as the couplings in general may depend on external controls, such as magnetic flux for Transmon qubits [34].

We focus on a system that is relevant for the implementation of entangling gates with superconducting qubits. However, similar arguments hold for instance for a quantum dot architecture, where the couplings depend on the external laser controls [156]. To substantiate the importance of our work, we show that the difference in fidelities, based on previous models and our extended one, can be on the order of 10^{-2} which is of indisputable importance for high-fidelity gates, given that error thresholds for fault-tolerant quantum error correction are believed to lie between 10^{-4} and 10^{-2} for many relevant systems [157]. A second-order Magnus expansion [158, 159] provides a closed analytic form to accurately estimate the errors observed in numerically exact simulations.

5.1 The Schrieffer-Wolff Transformation

The essence of the original SWT [135] is to remove a perturbation from some Hamiltonian $\hat{H}$. Hereto it generates an effective Hamiltonian $\hat{H}^{\text{eff}}$ from the Hamiltonian $\hat{H} = \hat{H}_0 + \epsilon(\hat{H}_1 + \hat{H}_2)$ using a perturbative expansion, so that $\hat{H}^{\text{eff}}$ is diagonal up to a desired order in the perturbing term $\epsilon(\hat{H}_1 + \hat{H}_2)$. Note that it is advantageous to separate the perturbation into a diagonal term $\hat{H}_1$ and a offdiagonal one $\hat{H}_2$ – both assumed to be constant operators. The effective Hamiltonian is then obtained via a unitary transformation so that $\hat{H}^{\text{eff}} = e^{-\hat{S}}\hat{H}e^{\hat{S}}$. The generator $\hat{S}$ must be anti-hermitian (this preserves the Lie structure of the problem [160]) and we continue to write the effective Hamiltonian in terms of nested commutators,

$$\hat{H}^{\text{eff}} = e^{-\hat{S}}\hat{H}e^{\hat{S}} = \sum_{j=0}^{\infty} \frac{1}{j!}[\hat{H}, \hat{S}]_j, \qquad (5.1)$$

whereby $[\hat{A}, \hat{B}]_n = [[\hat{A}, \hat{B}]_{n-1}, \hat{B}]$ and $[\hat{A}, \hat{B}]_0 = \hat{A}$. A typical, but not mandatory way to determine the sought transformation is to expand $\hat{S}$ in different orders j of ϵ, i.e. $\hat{S} = \sum_j \hat{S}_j$. Ultimately, this gives rise to removing the offdiagonal perturbation $\hat{H}_2$ up to a desired order in ϵ. One obtains successive equations for the $\hat{S}_j$ from an order-by-order expansion in the perturbation ϵ, e.g. $[\hat{H}_0, \hat{S}_1] = -\hat{H}_2$ removes the off-diagonal perturbation to lowest order. More details are provided in the remainder of this section, which extends the SWT to a generic time-dependent case.

5.1.1 Extension to Time-Dependent Perturbations

The formalism of the previous section needs to be extended [155], as soon as the perturbation is time-dependent. Then, the generator $\hat{S}$ in general is time-dependent as well, so that the amended transformation (5.1) becomes

$$\hat{H}^{\text{eff}} = e^{-\hat{S}} \hat{H} e^{\hat{S}} + i\partial_t \left(e^{-\hat{S}} \right) e^{\hat{S}}. \tag{5.2}$$

Analogously to before, equation (5.2) is expanded in terms of nested commutators so that the effective Hamiltonian can be written as

$$\hat{H}^{\text{eff}} = \sum_{j=0}^{\infty} \frac{1}{j!} [\hat{H}, \hat{S}]_j - i \sum_{j=0}^{\infty} \frac{1}{(j+1)!} [\dot{\hat{S}}, \hat{S}]_j. \tag{5.3}$$

We proceed to separate the effective Hamiltonian $\hat{H}^{\text{eff}}$ into off-diagonal ($\hat{H}^{\text{eff}}_{\text{od}}$) and diagonal ($\hat{H}^{\text{eff}}_{\text{d}}$) terms, which are given by

$$\begin{aligned}
\hat{H}^{\text{eff}}_{\text{od}} = &\sum_{j=0}^{\infty} \frac{1}{(2j+1)!} [\hat{H}_0 + \hat{H}_1, \hat{S}]_{2j+1} + \sum_{j=0}^{\infty} \frac{1}{(2j)!} [\hat{H}_2, \hat{S}]_{2j} \\
&- i \sum_{j=0}^{\infty} \frac{1}{(2j+1)!} [\dot{\hat{S}}, \hat{S}]_{2j},
\end{aligned} \tag{5.4a}$$

$$\begin{aligned}
\hat{H}^{\text{eff}}_{\text{d}} = &\sum_{j=0}^{\infty} \frac{1}{(2j)!} [\hat{H}_0 + \hat{H}_1, \hat{S}]_{2j} + \sum_{j=0}^{\infty} \frac{1}{(2j+1)!} [\hat{H}_2, \hat{S}]_{2j+1} \\
&- i \sum_{j=0}^{\infty} \frac{1}{(2j+2)!} [\dot{\hat{S}}, \hat{S}]_{2j+1}.
\end{aligned} \tag{5.4b}$$

Expanding $\hat{S} = \sum_j \hat{S}_j$ as a power series in the perturbation yields equations that remove off-diagonal terms in the effective Hamiltonian, i.e. solve $\hat{H}^{\text{eff}}_{\text{od}} = 0$ up to the desired order in ϵ, and thereby diagonalize the Hamiltonian. As stated before, the particular definition of $\hat{S}$ is not mandatory, but the typical choice of a perturbative expansion. Consequently, different ansätze for $\hat{S}$ lead to different diagonalizations. In order to compare orders of ϵ, we make the *a priori* assumption that $\partial_t \hat{S}_j$ is of order $(j+1)$ of the perturbation. Hence, the first few equations that determine the transformation read

$$[\hat{H}_0, \hat{S}_1] = -\hat{H}_2, \tag{5.5a}$$

$$[\hat{H}_0, \hat{S}_2] = -[\hat{H}_1, \hat{S}_1] + i\dot{\hat{S}}_1, \tag{5.5b}$$

$$[\hat{H}_0, \hat{S}_3] = -[\hat{H}_1, \hat{S}_2] - \frac{1}{3}[\hat{H}_2, \hat{S}_1]_2 + i\dot{\hat{S}}_2, \tag{5.5c}$$

$$[\hat{H}_0, \hat{S}_4] = -[\hat{H}_1, \hat{S}_3] - \frac{1}{3}[[\hat{H}_2, \hat{S}_1], \hat{S}_2] - \frac{1}{3}[[\hat{H}_2, \hat{S}_2], \hat{S}_1] + i\dot{\hat{S}}_3. \tag{5.5d}$$

Successively solving equations (5.5) will then cancel all perturbing terms up to the desired order so that the effective Hamiltonian $\hat{H}^{\text{eff}}$ is purely diagonal. We need to verify the consistency of solutions to equations (5.5) under the *a priori* assumption on the derivative of $\partial_t \hat{S}_j$: from equation (5.5a) we see that $\hat{S}_1$ inherits perturbation of order one from $\hat{H}_2$. Similarly, it follows from equation (5.5b) that $\partial_t \hat{S}_1$ and $\hat{S}_2$ are of order two in the perturbation and so on. This ensures the consistency of our expansion. Finally, the remaining diagonal terms in equation (5.4b) need to be calculated. We use equations (5.5) and obtain the first few remaining terms that constitute the effective Hamiltonian $\hat{H}^{\text{eff}} = \sum_j \hat{H}_j^{\text{eff}}$ to be

$$\hat{H}_0^{\text{eff}} = \hat{H}_0, \tag{5.6a}$$

$$\hat{H}_1^{\text{eff}} = \hat{H}_1, \tag{5.6b}$$

$$\hat{H}_2^{\text{eff}} = \frac{1}{2!}[\hat{H}_2, \hat{S}_1], \tag{5.6c}$$

$$\hat{H}_3^{\text{eff}} = \frac{1}{2!}[\hat{H}_2, \hat{S}_2], \tag{5.6d}$$

$$\hat{H}_4^{\text{eff}} = \frac{1}{2!}[\hat{H}_2, \hat{S}_3] - \frac{1}{4!}[\hat{H}_2, \hat{S}_1]_3. \tag{5.6e}$$

5.1.2   The Dispersive Transformation

A particular example of the SWT in the context of quantum information is the analysis of cavity-mediated residual interactions between multilevel systems. Under the assumption of weak coupling, the SWT can be used to derive an effective Hamiltonian which is free of interactions between multilevel systems and the cavity. Many fundamental concepts in quantum information, such as readout [42] and gate synthesis [43], are based on this so-called *dispersive frame*. We start with the decomposition of the Jaynes-Cummings Hamiltonian [161] for N multilevel systems with respective energy levels $\omega_j^{(m)}$, coupled to a cavity (oscillator frequency ω_r) with coupling strengths $g_{j,j+1}^{(m)}$ into

$$\hat{H}_0 = \omega_r \hat{a}^\dagger \hat{a} + \sum_{m=0}^{N} \sum_{j=0}^{\infty} \omega_j^{(m)} \hat{\Pi}_j^{(m)}, \tag{5.7a}$$

$$\hat{H}_1 = 0, \tag{5.7b}$$

$$\hat{H}_2 = \sum_{m=1}^{N} \sum_{j=0}^{\infty} g_{j,j+1}^{(m)} \left(\hat{\sigma}_j^{+(m)} \hat{a} + \hat{\sigma}_j^{-(m)} \hat{a}^\dagger \right), \tag{5.7c}$$

where superscript (m) labels the m-th element in the total Hilbert space, $\hat{\Pi}_j^{(m)} \equiv |j\rangle\langle j|^{(m)}$ is the projector to state $|j\rangle^{(m)}$ of system m, and $\hat{a}, \hat{a}^\dagger$ are

the harmonic ladder operators of the cavity. Hamiltonian $\hat{H}_0$ defines the bare energy levels of a harmonic oscillator with frequency ω_r and the N multilevel systems, while couplings between the oscillator and the multilevel systems are encoded in $\hat{H}_2$. For readability, we abstain from explicitly highlighting time-dependence, but we stress that in general both energy levels $\omega_j^{(m)}(t)$ and couplings $g_{j,j+1}^{(m)}(t)$ are time-dependent quantities. The raising and lowering operators of each multilevel system are given by $\hat{\sigma}_j^{+(m)} \equiv |j+1\rangle\langle j|^{(m)}$ and $\hat{\sigma}_j^{-(m)} \equiv |j\rangle\langle j+1|^{(m)}$, respectively. We aim at removing all interactions between the cavity and the multilevel systems up to second order, so that the dynamics can be solely reduced to the multilevel systems. Therefore, we need to find the operators $\hat{S}_1$ and $\hat{S}_2$ that satisfy equations (5.5a) and (5.5b), for the Hamiltonians given by equations (5.7). We note that

$$\left[\sum_{j=0}^{\infty}\left(\hat{\sigma}_j^{-(m)}\hat{a}^\dagger \pm \hat{\sigma}_j^{+(m)}\hat{a}\right), \hat{H}_0\right] \propto \sum_{j=0}^{\infty}\left(\hat{\sigma}_j^{-(m)}\hat{a}^\dagger \mp \hat{\sigma}_j^{+(m)}\hat{a}\right) \tag{5.8}$$

and use this identity to find solutions for the generators $\hat{S}_1$ and $\hat{S}_2$. With the shorthand notation $\delta_j^{(m)} \equiv \omega_{j,j+1}^{(m)} - \omega_r$ for the detunings from the resonator, and $\omega_{j,j+1}^{(m)} \equiv \omega_{j+1}^{(m)} - \omega_j^{(m)}$ we write the corresponding solutions as

$$\hat{S}_1 = \sum_{m=1}^{N}\sum_{j=0}^{\infty}\frac{g_{j,j+1}^{(m)}}{\delta_j^{(m)}}\left(\hat{\sigma}_j^{-(m)}\hat{a}^\dagger - \hat{\sigma}_j^{+(m)}\hat{a}\right), \tag{5.9a}$$

$$\hat{S}_2 = -i\sum_{m=1}^{N}\sum_{j=0}^{\infty}\frac{1}{\delta_j^{(m)}}\frac{\mathrm{d}}{\mathrm{d}t}\left(\frac{g_{j,j+1}^{(m)}}{\delta_j^{(m)}}\right)\left(\hat{\sigma}_j^{-(m)}\hat{a}^\dagger + \hat{\sigma}_j^{+(m)}\hat{a}\right). \tag{5.9b}$$

The so-called *dispersive Hamiltonian* up to second order then reads

$$\begin{aligned}
\hat{H}^{\text{eff}} = &\left\{\omega_r + \sum_{m=1}^{N}\sum_{j=1}^{\infty}\left(\chi_{j-1,j}^{(m)} - \chi_{j,j+1}^{(m)}\right)\hat{\Pi}_j^{(m)} - \sum_{m=1}^{N}\chi_{0,1}^{(m)}\hat{\Pi}_0^{(m)}\right\}\hat{a}^\dagger\hat{a} \\
&+ \sum_{m=1}^{N}\omega_0^{(m)}\hat{\Pi}_0^{(m)} + \sum_{m=1}^{N}\sum_{j=1}^{\infty}\left(\omega_j^{(m)} + \chi_{j-1,j}^{(m)}\right)\hat{\Pi}_j^{(m)} \\
&+ \sum_{m\neq n}\sum_{j,k=0}^{\infty}g_{j,j+1}^{(m)}\lambda_k^{(n)}\left(\hat{\sigma}_j^{-(m)}\hat{\sigma}_k^{+(n)} + \hat{\sigma}_j^{+(m)}\hat{\sigma}_k^{-(n)}\right) \\
&+ i\sum_{m\neq n}\sum_{j,k=0}^{\infty}g_{j,j+1}^{(m)}\frac{\dot{\lambda}_k^{(n)}}{\delta_k^{(n)}}\left(\hat{\sigma}_j^{-(m)}\hat{\sigma}_k^{+(n)} - \hat{\sigma}_j^{+(m)}\hat{\sigma}_k^{-(n)}\right).
\end{aligned} \tag{5.10}$$

Here we have denoted one of the expansion parameters by $\lambda_j^{(m)} \equiv g_{j,j+1}^{(m)}/\delta_j^{(m)}$, which we will refer to as the *dispersive parameter*, and introduced the dispersive shift

$$\chi_{j,j+1}^{(m)} \equiv \frac{\left(g_{j,j+1}^{(m)}\right)^2}{\delta_j^{(m)}}. \tag{5.11}$$

The contribution from $\hat{S}_2$ adiabatically eliminates a time-dependent qubit-cavity interaction that would be apparent if the usual SWT was applied and the effective Hamiltonian was then additionally extended by the summand $i\partial_t(e^{-\hat{S}})e^{\hat{S}}$, describing inertial forces when the new frame is interpreted as an accelerated reference frame. In fact, Hamiltonian (5.10) is almost identical to the commonly used dispersive Hamiltonian [162]: The multilevel systems are energy-shifted by the dispersive shifts and are dispersively coupled among each other through the cavity via $\hat{\sigma}^+\hat{\sigma}^-$-type interactions, whereby the interaction strength scales as $1/\delta$. Additionally, we observe the usual shift of the resonator frequency ω_r by a value that depends on the state of the multilevel systems, which ultimately can be used for readout purposes [163]. However, in addition to the common dispersive Hamiltonian, the regular dispersive coupling terms in the third line of Hamiltonian (5.10) are amended by a different type of interaction terms accounting for inertial errors. The latter scale proportionally to $\dot{\lambda}_k^{(n)}$ – essentially the speed at which the parameters are modulated.

In order that our perturbative expansion, which leads to Hamiltonian (5.10), is valid we need to limit the magnitude of the expansion parameters. They need to meet the conditions

$$\lambda_j^{(m)} \ll 1, \tag{5.12a}$$

$$\dot{\lambda}_j^{(m)}/\delta_j^{(m)} \ll 1, \tag{5.12b}$$

for all values of j and m. Otherwise higher-order terms in equations (5.6) need to be considered, which is straightforward and does not qualitatively change the results. Since equation (5.12b) basically limits the velocity at which λ may change, we refer to $\dot{\lambda}_j^{(m)}/\delta_j^{(m)}$ as *dispersive adiabaticity parameter*.

5.2 Entangling Two Transmon Qubits

As an example, we choose to work with two Transmon qubits [34] coupled to a shared resonator ω_r. From Hamiltonian (5.10) we see that the physical qubits

dispersively couple to each other through the cavity. This interaction provides a common way to implement a controlled-phase gate: The avoided crossing between the $|11\rangle$ and $|20\rangle$ states can be used to control the phase of state $|11\rangle$ [144]. Conventionally, this amounts to keeping one qubit (Q1) at a constant frequency whereas the frequency of qubit two (Q2) changes in time: First being far detuned from Q1 and ω_r, it is tuned to a constant frequency close to resonance with Q1 in order to generate a strong dispersive interaction. Both qubits interact for a certain time t_g and Q2 is tuned back from close-resonance as soon as the interaction time t_g was long enough to implement the desired gate. Optimal control theory has sought fast pulses to produce high-fidelity gates based on the dispersive interaction using a geometric derivation [150], as well as a deeper analysis of the underlying Landau-Zener physics [151]. For convenience, we only work in the relevant $\{|11\rangle, |20\rangle\}$ subspace, where the reduced Hamiltonian $\hat{H}_{\text{red}}^{\text{eff}}$ is given by

$$\hat{H}_{\text{red}}^{\text{eff}} = \frac{\chi_t + \delta\omega - \Delta^{(1)}}{2}\hat{\sigma}_z + \left(g_{0,1}^{(2)}\lambda_1^{(1)} + g_{1,2}^{(1)}\lambda_0^{(2)}\right)\hat{\sigma}_x - \left(\frac{\dot{\lambda}_0^{(2)}g_{1,2}^{(1)}}{\delta_0^{(2)}} - \frac{\dot{\lambda}_1^{(1)}g_{0,1}^{(2)}}{\delta_1^{(1)}}\right)\hat{\sigma}_y. \tag{5.13}$$

Here, we denote the anharmonicity of the first Transmon by $\Delta^{(1)}$, and use the definitions $\delta\omega = \omega_1^{(2)} - \omega_1^{(1)}$ and $\chi_t = \chi_{0,1}^{(1)} + \chi_{0,1}^{(2)} + \chi_{1,2}^{(1)}$. In order to speed up the conventional implementation of two-qubit gates [144] – which is based on the formalism explained above – tremendously, real-time control of frequencies via modulating the applied magnetic flux Φ [150, 151] is required. The qubit frequencies ω_j as well as the couplings $g_{j,j+1}$ scale with the applied magnetic flux, which changes the Josephson energy E_J of the Josephson junctions [34],

$$E_J(\Phi) = E_{J\Sigma}\cos\left(\frac{\pi\Phi}{\Phi_0}\right)\sqrt{1 + d^2\tan\left(\frac{\pi\Phi}{\Phi_0}\right)} \tag{5.14}$$

$$g_{j,j+1}(\Phi) \propto \sqrt{\frac{j+1}{2}}\left(E_J(\Phi)\right)^{1/4} \tag{5.15}$$

$$\omega_j(\Phi) = j\sqrt{8E_c E_J(\Phi)} + \Delta_j, \tag{5.16}$$

whereby Φ_0 is the magnetic flux quantum, E_c the charging energy and d is the junction asymmetry. Without loss of generality we focus on symmetric junctions, i.e. $d = 0$. The anharmonicities Δ_j in case of a Duffing oscillator – which is a good approximation for Transmon qubits – are given by [41]

$$\Delta_j = \frac{j(j-1)}{2}\Delta_2. \tag{5.17}$$

5.2.1 Relevance of Time-Dependent Effects

If advanced controls [150, 151] are used, explicit time-dependence in form of real-time flux control enters the problem. Specifically, the qubit frequencies (and hence the detunings δ_j) depend on time. Moreover, as given by equation (5.15), the coupling strengths $g_{j,j+1}$ also depend on the applied flux. It is crucial to note that especially the flux-dependence of g is usually not considered in literature, and so the effective Hamiltonians are derived without taking into account the effect of real-time parameter control in the SWT [164]. However, we will show that it is inevitable to rigorously incorporate these effects if implementations of high-fidelity gates, compatible with current error thresholds, are desired. Along these lines, it is also important to question the assumption of constant off-diagonal elements in Hamiltonian (5.13), as is for instance used in Refs. [150, 151].

The parameters we use to simulate the Transmon system yield moderate couplings $g/2\pi \approx 27\,\mathrm{MHz}$ and qubit frequencies on the order of 7 GHz around the bias points. We proceed to show that (i) the full TDSWT needs to be applied as soon as one aims at high-fidelity gates and (ii) that the assumption of constant off-diagonal elements severely deteriorates results. The exemplary waveforms we consider are smooth and slow sinusoidal (Φ_s) as well as tangential (Φ_t) controls, both with flux changes of $\Delta\Phi = 60\,\mathrm{m}\Phi_0$ at maximum, i.e.

$$\Phi_s(t) = \Phi_{\mathrm{bias}} + A \cdot \sin(2\pi\nu t + \varphi) \tag{5.18a}$$

$$\Phi_t(t) = \Phi_{\mathrm{bias}} + A \cdot \tan\left(B \cdot \mathrm{Erf}\left(C \left(t - \frac{t_g}{2} \right) \right) \right), \tag{5.18b}$$

where A, B, C, ν and φ are constants, Φ_{bias} is a static bias and $\mathrm{Erf}(x)$ is the Gauss error function. Tangential pulses and pulses with sinusoidal modulations were used explicitly in [151]. We evolve $\hat{H}_{\mathrm{red}}^{\mathrm{eff}}$ with both of these controls and quantify the effects in question by considering three different situations, represented by the three unitaries

- $\hat{U}_1$: Full simulation of $\hat{H}_{\mathrm{red}}^{\mathrm{eff}}$,

- $\hat{U}_2$: Neglect terms proportional to $\dot{\lambda}$ in $\hat{H}_{\mathrm{red}}^{\mathrm{eff}}$,

- $\hat{U}_3$: Neglect terms proportional to $\dot{\lambda}$ in $\hat{H}_{\mathrm{red}}^{\mathrm{eff}}$ and approximate all instances of g, χ and δ as their mean values.

To measure the individual gate errors derived from those three models, we use the common gate overlap fidelity

$$F_1(\hat{U}) = \frac{1}{d_Q^2} \left| \mathrm{Tr}\left(\hat{U}^\dagger \hat{U}_t \right) \right|^2 \tag{4.1}$$

and choose a set of $N_s = 10000$ random target unitaries $\hat{U}_t$ of dimension $d_Q = 2$, that are parametrized by the angles $\vec{\varphi} \equiv (\varphi_1, \varphi_2, \varphi_3)$ and given in the representation

$$\hat{U}_t = \hat{U}(\vec{\varphi}) \equiv \begin{pmatrix} e^{i\varphi_1}\cos(\varphi_3) & e^{i\varphi_2}\sin(\varphi_3) \\ -e^{-i\varphi_2}\sin(\varphi_3) & e^{-i\varphi_1}\cos(\varphi_3) \end{pmatrix} \tag{5.19}$$

for an arbitrary 2×2 unitary matrix. We evaluate fidelity (4.1) for each of the $\hat{U}_j$ ($j = 1, 2, 3$) with respect to the N_s different random target unitaries and compute the fidelity differences

$$\Delta F(\hat{U}_1, \hat{U}_n) = F_1(\hat{U}_1) - F_1(\hat{U}_n) \tag{5.20}$$

to quantify errors corresponding to the approximations upon which the propagators $\hat{U}_2$ and $\hat{U}_3$ are based. The corresponding normalized histograms are plotted in FIG. 5.1 for sinusoidal and tangential modulations with realistic gate times of $t_g = 30\,\text{ns}$. The top row of FIG. 5.1 reveals that even for smooth pulses without any fast modulation, an incorrect frame transformation (SWT vs. TDSWT) translates into average discrepancies between fidelities on the order of 10^{-3}. For models that assume constant off-diagonal components in the reduced Hamiltonian (5.13), as was done in earlier studies [150, 151], discrepancies in gate fidelities are even on the order of 10^{-2} (bottom row of FIG. 5.1). To substantiate the importance of the results, we highlight that the pulses we used for simulations are significantly smoother (and free from fast oscillations) than usual control shapes, for instance obtained via methods of optimal control theory. Those pulses typically exhibit relatively fast changes, which in turn lead to increasing values for the velocities $\dot{\lambda}_j^{(m)}$ and thereby even higher mismatches in gate fidelities.

5.2.2 Error Estimation via Magnus Expansion

A second order Magnus expansion [158, 159] can be used to understand the error statistics depicted in FIG. 5.1. In general, the Magnus expansion is a way to analytically express the unitary propagator of a quantum system at time t_g, subject to a time-dependent Hamiltonian $\hat{H}$ as

$$\hat{\bar{U}} = \exp\left(-it_g \sum_{k=1}^{\infty} \hat{\bar{H}}^{(k)}\right). \tag{5.21}$$

Explicit forms for the so-called *averaged Hamiltonians* $\hat{\bar{H}}^{(k)}$ exist [158, 159] and account for time-ordering issues. We use a second order Magnus expansion
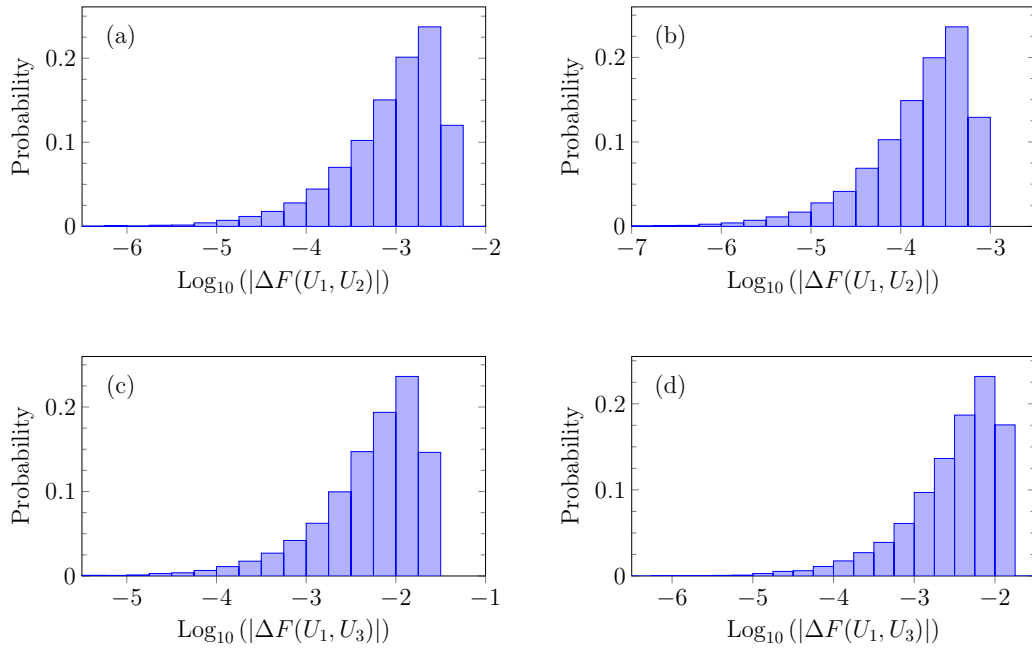
FIG. 5.1 – Normalized histograms for the differences in fidelity ΔF with respect to $N_s = 10000$ random unitaries. Neglecting the time-dependent part of the dispersive transformation ($\propto \dot{\lambda}$) leads to errors on the order of 10^{-3} (top row). Models as were used before [150, 151] – that assume all instances of g, χ and δ to be constant – lead to errors on the order of 10^{-2} (bottom row). Parts (a) and (c) belong to sinusoidal pulses Φ_s, (b) and (d) to tangential ones (Φ_t) given by equations (5.18). The discrepancies associated to nonadiabatic corrections to the Hamiltonian are of great relevance for high-fidelity gates.

to approximate the unitaries $\hat{U}_1$ and $\hat{U}_2$. That is, we truncate series (5.21) at $k = 2$, so that only the first and second order averaged Hamiltonians

$$\bar{\hat{H}}^{(1)} = \frac{1}{t_g} \int\limits_0^{t_g} dt \, \hat{H}(t), \tag{5.22a}$$

$$\bar{\hat{H}}^{(2)} = -\frac{i}{2t_g} \int\limits_0^{t_g} dt_2 \int\limits_0^{t_2} dt_1 \left[\hat{H}(t_2), \hat{H}(t_1) \right], \tag{5.22b}$$

are required. For convenience we introduce the shorthand notation

$$\omega = \left\langle 11 \left| \hat{H}_{\text{red}}^{\text{eff}} \right| 11 \right\rangle, \tag{5.23a}$$

$$g_r = \text{Re} \left\{ \left\langle 11 \left| \hat{H}_{\text{red}}^{\text{eff}} \right| 20 \right\rangle \right\}, \tag{5.23b}$$

$$g_i = -\text{Im} \left\{ \left\langle 11 \left| \hat{H}_{\text{red}}^{\text{eff}} \right| 20 \right\rangle \right\}, \tag{5.23c}$$

to simplify Hamiltonian (5.13). After employing identity (1.5) we end up with a closed analytic expression for the error ΔF,

$$\begin{aligned}
\Delta F(\bar{\hat{U}}_1, \bar{\hat{U}}_2) = \ & f(\alpha_1, \bar{\omega} + \delta_{g_i,g_r}, \delta_{\omega,g_r} - \bar{g}_i, \bar{g}_r + \delta_{\omega,g_i}, \vec{\varphi}) \\
& - f(\alpha_2, \bar{\omega}, \delta_{\omega,g_r}, \bar{g}_r, \vec{\varphi}).
\end{aligned} \tag{5.24}$$

Here, the time-averaged mean of a function $s(t)$ is denoted by a stacked bar, i.e. $\bar{s} \equiv \frac{1}{t_g} \int_0^{t_g} dt \, s(t)$. Information about the unitary's phases enters through the second order Magnus terms, which are determined by the quantities

$$\delta_{\omega,g_r} = \int\limits_0^{t_g} dt_2 \int\limits_0^{t_2} dt_1 \, (\omega(t_2)g_r(t_1) - \omega(t_1)g_r(t_2)), \tag{5.25a}$$

$$\delta_{\omega,g_i} = \int\limits_0^{t_g} dt_2 \int\limits_0^{t_2} dt_1 \, (\omega(t_2)g_i(t_1) - \omega(t_1)g_i(t_2)), \tag{5.25b}$$

$$\delta_{g_i,g_r} = \int\limits_0^{t_g} dt_2 \int\limits_0^{t_2} dt_1 \, (g_i(t_2)g_r(t_1) - g_i(t_1)g_r(t_2)). \tag{5.25c}$$

The rotation angles of unitaries $\bar{\hat{U}}_1$ and $\bar{\hat{U}}_2$ are set by the constants

$$\alpha_1 = \sqrt{(\bar{\omega} + \delta_{g_i,g_r})^2 + (\delta_{\omega,g_r} - \bar{g}_i)^2 + (\bar{g}_r + \delta_{\omega,g_i})^2}, \tag{5.26a}$$

$$\alpha_2 = \sqrt{\bar{\omega}^2 + \delta_{\omega,g_r}^2 + \bar{g}_r^2}, \tag{5.26b}$$
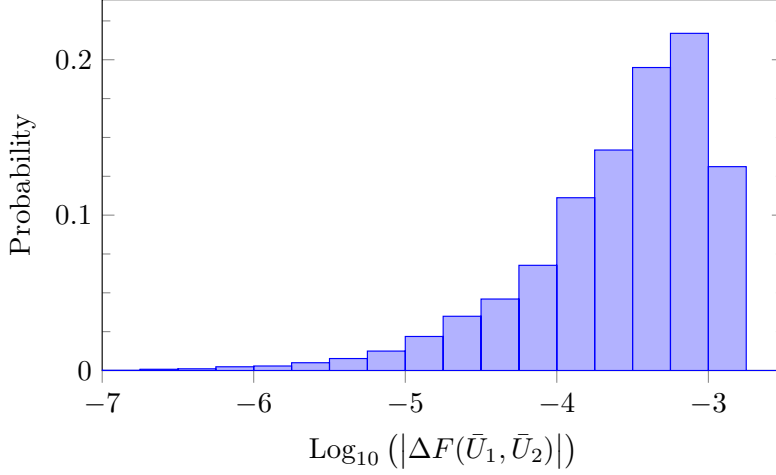
FIG. 5.2 – Normalized histogram for the difference in fidelity ΔF with respect to $N_s = 10000$ random unitaries obtained from a second order Magnus expansion, see equation (5.24). The statistics are based on a tangential pulse and reproduce those of FIG. 5.1a very well.

respectively. The function $f(\alpha, a_1, a_2, a_3, \vec{\varphi})$ in equation (5.24) is defined as

$$
\begin{aligned}
f(\alpha, a_1, a_2, a_3, \vec{\varphi}) =\frac{4}{\alpha^2}\{&\alpha\cos(\varphi_1)\cos(\alpha)\cos(\varphi_3) - \sin(\alpha)\{a_1\cos(\varphi_3)\sin(\varphi_1) \\
&+ a_2\cos(\varphi_2)\sin(\varphi_3) + a_3\sin(\varphi_2)\sin(\varphi_3)\}\}^2 .
\end{aligned}
\tag{5.27}
$$

Indeed, as shown in FIG. 5.2 for tangential pulses, equation (5.24) reproduces the statistics of a numerically exact simulation, shown in FIG. 5.1a, very well. The mean error, independent of $\vec{\varphi}$, is obtained via averaging $\Delta F(\hat{\bar{U}}_1, \hat{\bar{U}}_2)$ over $\vec{\varphi} \in [0, 2\pi]^{\otimes 3}$, and yields a value of $\overline{\Delta F} \sim 10^{-3.21}$ for the situation considered in FIG. 5.2.

5.3 Conclusion

We have given a detailed outline of the time-dependent Schrieffer-Wolff transformation and applied it to derive a general expression for the dispersive Hamiltonian of arbitrarily many multilevel systems coupled to a cavity via a Jaynes-Cummings type of interaction. The usual dispersive coupling between the multilevel systems is altered by terms that scale with the dispersive adiabaticity parameter – essentially the speed at which parameters change in time.

As a specific example, we provide a simple but accurate model to implement dispersive entangling two-qubit gates using only $\hat{\sigma}_z$-control of the qubits. Fidelities based on previous models are shown (numerically and analytically) to differ from those based on our extended model by up to 10^{-2} for control fields without fast modulation. Given state-of-the-art error thresholds for scalable fault-tolerant architectures, we remark that the nonadiabatic corrections we derived are of substantial importance for accurate simulations. In case of high-frequency controls, or pulses with fast flux sweeps, higher-order terms of the TDSWT need to be considered, and estimated gate fidelities based on previous models become even more erroneous. Note that the discussion in this chapter does not address the determination of optimal waveforms. Instead, it provides a general toolset to derive simplified but accurate models which then may be used for accurate simulations, for instance in order to apply quantum optimal control.

As a final note, we highlight that the fundamental effects considered in this chapter are not only apparent in the dispersive frame: For instance the dependence of qubit-cavity coupling strengths g on the applied magnetic flux are also relevant in simulations of the full Jaynes-Cummings Hamiltonian. These effects should be carefully analyzed in order to provide accurate simulations of the real dynamics.

Chapter 6

Derivative-based Analytical Optimal Control

The optimization algorithms that were introduced in section 4.2 find optimal solutions to control fields with the aid of numerical assistance: Typically, they require numerically exact solutions to the system dynamics, and update the control fields based on these numerical computations. In certain cases, however, it is also possible to find optimal solutions that achieve a desired result solely by analytical techniques. In this chapter we will review the *Derivative Removal by Adiabatic Gate* (DRAG) framework [40, 41, 165] and present state-of-the-art insights regarding the underlying theory and its applications. The majority of this chapter deals with effective frame transformations in order to derive optimal solutions, directly connecting to the concept presented in chapter 5.

The DRAG technique [40, 41, 165] was developed in the context of the emerging technology of high-precision superconducting quantum devices. With coherence times of these systems improving dramatically towards the end of the first decade in twenty-first century, it became a promising possibility to address desired quantum transitions in these systems with increasing spectral resolution [166–169]. However, very fast pulses were needed to operate below the limits imposed by decoherence, which was a problem both in terms

---

This chapter was published as an invited *Focus* article in "L.S. Theis, F. Motzoi, S. Machnes and F.K. Wilhelm, EPL **123**, 60001 (2018)". The majority of the text was written by L.S. Theis and F. Motzoi. S. Machnes provided the calibration data for FIG. 6.3 and contributed the majority of text in the calibration subsection 6.4.3. The chapter mostly reviews known techniques, but also provides new information; particularly: (i) Connection between derivative-based control and related methodologies, (ii) Exact, instructive formulation of the problem, e.g. equations (6.7) and (6.8), (iii) Connection between spectral engineering and adiabaticity, and (iv) Recommendations based on previous experience.

of microwave shaping technology in a highly cooled environment [170] and in terms of the rich level structure of nonlinear superconducting quantum circuits, which involves unwanted coupling to quantum states outside the computational subspace – typically referred to as *leakage* levels [171, 172]. The basic DRAG idea was to augment a simple smooth Rabi pulse $\Omega(t)\hat{\sigma}_x$ with an off-quadrature auxiliary pulse with a simple dependence $\propto \partial_t\Omega(t)\hat{\sigma}_y/\Delta$, where Δ is the gap energy to the nearest excited state.

The basic mechanism behind the correction is the removal of diabatic errors so that the system couples to the leakage subspace only adiabatically, returning back to the computational space by the end of the pulse. Such ideas have a rich history, including the first application to removing leakage from STIRAP pulses [173], to its generalization to a broader class of problems in [174, 175], to the formulation in terms of transitionless dynamics in [176], and finally to a general categorization under the framework of *Shortcuts to Adiabaticity* (STA) [177].

Although DRAG is closely related to these ideas, they are not interchangeable and functionally solve different kinds of problems in quantum mechanics: (i) The DRAG framework is a convergent expansion that allows removing series of errors that differently affect different portions of the Hilbert space and operators therein. Thus, functionally, it is perhaps closest to the transitionless superadiabatic driving technique of [178], based on the superadiabatic expansion [179, 180]. (ii) The DRAG expansion allows the solution of not just one STA but can remove a system of diabatic errors to a manifold of unwanted low-lying gap states. In this sense, it is a powerful extension of STA methodology. (iii) While STA usually deals with problems of adiabatic passage techniques, DRAG is equally well applicable to resonant driving problems, also known as spectral selectivity problems, where one can think of an *adiabatic elimination* of fast subspaces (closely related to the method presented in chapter 5) while only perturbatively affecting the near-degenerate subspace where resonant driving occurs.

The method was first tested in [181, 182]. Since then it has become a standard tool in superconducting qubit experiments [144, 152, 183–190]. There have been numerous implementations, extensions, and applications to different physical systems in the intervening ten years since the first presentation of the ideas. Other techniques to deal with harmful transitions were developed [191, 192] but do not feature the flexibility of DRAG pulses, particularly with regards to spectral selectivity. We review here some of the main developments, including: (i) Connections drawn to other STA methods [177], (ii) a better understanding of the convergence properties of the expansion [165], (iii) the application to spins, optical lattices and Rydberg atoms [98, 165, 193, 194], (iv) and the development of the closely related technique of *Weak AnHarmonicity*

With Average Hamiltonian (WAHWAH) [122, 195].

The chapter is structured as follows: We first introduce the reader to relevant and related control frameworks, in particular the adiabatic theorem, superadiabaticity and counterdiabaticity. In the subsequent section 6.2, we then present a general mathematical formulation of how DRAG solutions can be derived exactly, using iterated frames. In particular, we show how to deal with diabatic errors on multiple and/or uncontrolled transitions. However, for typical multi-level problems, it can be intractable to exactly solve the equations obtained from this general theory. We therefore continue to present three useful expansions to obtain perturbative DRAG solutions in section 6.3. Section 6.4 ends the discussion with a review of significant, experimentally motivated examples to demonstrate the general applicability of DRAG, and show how perturbative solutions are obtained for a given system.

6.1   Review of Adiabatic Control Techniques

Consider a Hamiltonian $\hat{H}_0(t)$ with eigenvalues $E_n(t)$ and eigenstates $|n_0(t)\rangle$, respectively. The adiabatic theorem [180, 196–198] states that if the system is initially prepared in some instantaneous eigenstate $|n_0(t)\rangle$, the state evolved according to Schrödinger's equation $i\partial_t |\psi(t)\rangle = \hat{H}_0(t) |\psi(t)\rangle$ will follow this eigenstate, i.e. $|\psi(t)\rangle = |n_0(t)\rangle$ up to a phase, provided the Hamiltonian $\hat{H}_0(t)$ changes sufficiently slowly ($\hbar \equiv 1$). This is referred to as adiabatic evolution. We refer the reader to Ref. [199] for a detailed and rigorous analysis of different formulations of the theorem. It is convenient to transform to the adiabatic frame of $\hat{H}_0$, that is the diagonal basis $\{|\phi_n\rangle\}$, by a unitary transformation $\hat{V}_0(t) = \sum_n e^{i\varphi_n(t)} |n_0(t)\rangle\langle\phi_n|$, according to

$$\hat{H}_{\text{eff}}(t) = \hat{V}_0^\dagger(t)\hat{H}_0(t)\hat{V}_0(t) + i\dot{\hat{V}}_0^\dagger(t)\hat{V}_0(t). \tag{6.1}$$

The *inertial term* $\hat{I}(t) \equiv i(\partial_t \hat{V}_0^\dagger(t))\hat{V}_0(t)$ is the source of transitions between instantaneous eigenstates of $\hat{H}_0$ (we refer to these as *diabatic* or *nonadiabatic* errors, as introduced in a slightly different context in chapter 5). If the adiabatic theorem can be applied, we may neglect the inertial term $\hat{I}(t)$ in equation (6.1) up to a geometric phase [200], canceled for convenience via the free phase $\varphi_n(t) = \int_0^t \langle n(t')|\partial_{t'} n(t')\rangle \, \mathrm{d}t'$. Time evolution of the diagonal Hamiltonian $\hat{D}(t) \equiv \hat{V}_0^\dagger(t)\hat{H}_0(t)\hat{V}_0(t) = E_n(t) |\phi_n\rangle\langle\phi_n|$ is then given straightforwardly by

$$\hat{U}(t) = \sum_n e^{-i\int_0^t E_n(t')\mathrm{d}t'} |\phi_n\rangle\langle\phi_n| , \tag{6.2}$$

where the evolution in the original basis is $\hat{V}_0(t)\hat{U}(t)\hat{V}_0^\dagger(0)$.

6.1.1   Superadiabaticity

For practical applications of system control, Hamiltonians often do not change slowly enough to justify an adiabatic approximation as given by equation (6.2), i.e. neglecting the diabatic term $\hat{I}(t)$. In order to properly quantify the finite rate of change theory needs to be extended accordingly. To this end, Berry provided a useful framework under the name of *superadiabaticity* [180, 201], formulated also 20 years earlier by Garrido [179] in the context of adiabatic invariants. The method amounts to finding corrections to the Hamiltonian that account for finite inertial terms, by utilizing a sequence of iterative adiabatic transformations. That is, analogously to equation (6.1), we define the j-th adiabatic frame Hamiltonian recursively as

$$\hat{H}_j = \hat{V}_{j-1}^\dagger \hat{H}_{j-1} \hat{V}_{j-1} + i\dot{\hat{V}}_{j-1}^\dagger \hat{V}_{j-1}, \quad j \geq 1. \tag{6.3}$$

We assume all operators are (implicitly) time-dependent from this point onward. Each $\hat{V}_j$ diagonalizes the error term $\hat{I}_{j-1} \equiv i(\partial_t \hat{V}_{j-1}^\dagger)\hat{V}_{j-1}$ from previous order, producing a new diagonal Hamiltonian $\hat{D}_j \equiv \hat{V}_j^\dagger \hat{H}_j \hat{V}_j$ and a new inertial term $\hat{I}_j$.

Unfortunately, these iterative transformations eventually begin to diverge [201] from the actual dynamics of $\hat{H}_0$ and so the expansion must be truncated. The accuracy of a given frame can be quantified by the adiabatic quality factor $Q_j \equiv \int_0^{t_g} \|\hat{D}_j\|/\|\hat{I}_j\|$. The highest value of Q_j corresponds to the optimal frame, after which the series starts to diverge. However, for the purposes of high-fidelity quantum control, this frame will often be insufficient to meet accuracy requirements and therefore motivated the development of more accurate control methods over the last twenty years. Nonetheless, the insight from the superadiabatic expansion will be crucial to using the DRAG framework which relies on the existence of such equivalent-frame adiabatic transformations.

6.1.2   Counterdiabaticity

Counterdiabaticity, also known as *transitionless quantum driving* [176, 177], comprises a technique to construct a Hamiltonian which drives states that exactly follow a desired trajectory. There are many choices for this counterdiabatic Hamiltonian $\hat{H}_{\mathrm{cd}}$, for instance due to different possible phases in the exponent of equation (6.2), but the most straightforward one is to exactly cancel the diabatic error term $\hat{I}(t)$. To this end, we augment the Hamiltonian

$\hat{H}_0$ to become

$$\hat{\tilde{H}}_0(t) = \hat{H}_0(t) + \hat{H}_{\text{cd}}(t),$$
$$\hat{H}_{\text{cd}}(t) = -\hat{V}_0(t)\hat{I}(t)\hat{V}_0^\dagger(t) \tag{6.4}$$

which renders equation (6.2) exact.

6.2 Removing Systems of Inertial Terms

Combining the superadiabatic series with counterdiabaticity gives rise to the ability to solve systems with many unwanted diabatic transitions, including those that are not contained in the control Hamiltonian. This basic idea underlies the DRAG framework [40, 41, 165] and related methodology [178]. The DRAG transformations can take the form of a single dressing transformation, or an iterative frame expansion like the superadiabatic one.

6.2.1 Basic Iterative Framework

Using equation (6.3), we successively diagonalize the initial Hamiltonian as before. The expansion is now truncated at the N-th frame, which we refer to as the *DRAG frame*, and rendered exact by the addition of a driving term which cancels $\hat{I}_N = i(\partial_t \hat{V}_N^\dagger)\hat{V}_N$. Thus, transforming back to the initial Schrödinger picture, i.e. the frame of $\hat{H}_0$ (the *lab frame*), the respective counterdiabatic correction is

$$\hat{H}_{\text{cd}} = -i\hat{W}_N\hat{I}_N\hat{W}_N^\dagger = -i\hat{W}_N\dot{\hat{V}}_N^\dagger\hat{W}_{N-1}^\dagger, \tag{6.5}$$

where $\hat{W}_j \equiv \prod_{m=0}^j \hat{V}_m$ gives the transformation from first to j-th frame. A necessary condition for equations (6.3) and (6.5) to match the intended dynamics is that the DRAG frame must coincide with the lab frame at initial and final time, i.e. $\hat{W}_N(0) = \hat{W}_N(t_g) = \hat{\mathbb{1}}$. In this frame, equation (6.5) ensures that the effective Hamiltonian is leakage-less with respect to unwanted couplings, i.e. $\langle m|\hat{\tilde{H}}_N|n\rangle = 0$ for all relevant states $|m\rangle \neq |n\rangle$. One should note, however, that the DRAG frame is a dressed frame, and only the DRAG frame is transitionless throughout: All others exhibit leakage during intermediate times. Nonetheless, if the DRAG frame is equivalent to the lab frame at the boundaries of the time window, this ensures that no population remains in the unwanted states of the lab frame as well. This condition can typically be met if the control fields smoothly vanish for $t \in \{0, t_g\}$.

Next, we apply the DRAG methodology to two important cases of quantum control: First, when the diabatic error $\hat{I}_N$, and hence the desired correction, do

not match the operator form of a physical control in the lab. Second, when two different diabatic error terms ($\hat{I}_N = \hat{I}_N^{(1)} \oplus \hat{I}_N^{(2)}$) need to be corrected by operator terms sharing a single time dependence, e.g. a single laser field. We will refer to these situations as *uncontrolled* and *overconstrained* transitions, respectively. Though these two problems are in fact operationally quite different, most systems will exhibit both kinds of diabaticities.

6.2.2 Uncontrolled Diabaticities

In order to find solutions that are confined to attainable controls of the system we decompose the correction Hamiltonian (6.5) in terms of some available set of $k = 1, \ldots, M$ non-overlapping controls. That is, we decompose the controllable Hamiltonian as $\hat{H}^{\text{ctrl}}(t) = \sum_k u_k(t)\hat{h}_k + \text{h.c.}$ with control fields u_k and coupling terms $\hat{h}_k = |\psi_k^{(\text{to})}\rangle\langle\psi_k^{(\text{from})}|$, so that

$$\hat{H}_{\text{cd}}(t) \equiv -i \sum_{k=1}^{M} \left[u_k(t)\hat{h}_k + u_k^*(t)\hat{h}_k^\dagger \right]. \tag{6.6}$$

We iteratively apply superadiabatic transformations to determine the control fields $u_k = \sum_j u_{k,j}$ in the counterdiabatic Hamiltonian (6.6). The $u_{k,j}$ are contributions to the optimal control fields in the lab frame which cancel diabatic errors from the j-th superadiabatic frame. To confine the corrections to the attainable controls, we calculate the respective overlap with the diabatic error $\hat{I}_j$ for each successive superadiabatic iteration j, i.e.

$$\begin{aligned} u_{k,j}(t) &= -i \left\langle \psi_k^{(\text{from})} \left| \hat{W}_j \hat{I}_j \hat{W}_j^\dagger \right| \psi_k^{(\text{to})} \right\rangle, \\ \hat{I}_j^{\text{red}} &= i \dot{\hat{V}}_j^\dagger \hat{V}_j - \sum_k \hat{W}_j^\dagger \left[u_{k,j}\hat{h}_k + u_{k,j}^* \hat{h}_k^\dagger \right] \hat{W}_j. \end{aligned} \tag{6.7}$$

The inertial term $\hat{I}_j$ is now generally reduced with DRAG to $\hat{I}_j^{\text{red}}$ for $j > 0$, i.e. there is a partial cancellation if the counterdiabatic corrections do not perfectly map to attainable controls. Subsequent superadiabatic iterations are used to diagonalize $\hat{I}_j^{\text{red}}$ along the lines of (6.3), where $\hat{I}_j^{\text{red}}$ now replaces $i(\partial_t \hat{V}_j^\dagger)\hat{V}_j$. Whereas the standard sequence of superadiabatic transformations may often diverge ($Q_\infty \to 0$), series (6.7) will (typically) converge to zero error as the diabatic error is iteratively reduced. For example, a three-level system where one transition is driven and a second remains constant and uncontrolled will exhibit this feature [202].

   In practice, some transitions may share a common time-dependence. However, we omit this case here for clarity because it typically results in overconstrained transitions – which will be treated in the next subsection.

6.2.3   Overconstrained Diabaticities

When error terms are not independently controlled (as is usually the case), this can lead to counterdiabatic expansions that do not converge, similarly to the superadiabatic series (6.3). This can be understood as a consequence of the fact that for long times $|\hat{I}_{j+1}| \geq |\hat{I}_j|$ [165, 201], and so we must proceed carefully. For clarity, we consider here the case where all transitions in the system are controlled with a single global field, i.e. $u_k(t) = u(t)$. The direct recursive solution (6.7) will now be replaced with the simultaneous constraints

$$u(t) = \sum_j v_j(t) \ \text{ and } \ \left\langle m \,\middle|\, \hat{I}_N^{\text{red}} \,\middle|\, n \right\rangle = 0, \quad \forall m \neq n,$$

$$\text{where again} \quad \hat{I}_j^{\text{red}} = i\dot{\hat{V}}_j^{\dagger}\hat{V}_j - \sum_k \hat{W}_j^{\dagger} \left[v_j \hat{h}_k + v_j^* \hat{h}_k^{\dagger} \right] \hat{W}_j. \tag{6.8}$$

Here, the $u_{k,j}$ from the previous case (6.7) were replaced by v_j to emphasize the independence of k. The system (6.8) becomes fully constrained when the total number of frames N equals the number of unwanted transitions M. A larger frame number can also be used, for example if some controls are not attainable. Usually it is possible to obtain solutions for all times simultaneously through a single system of M algebraic equations (see also [203] where it is exact).

6.3   Perturbation methods with DRAG

The formulation of the counterdiabatic correction to the superadiabatic expansion is not generally analytically solvable, and for infinite dimensional systems even numerical solutions are intractable. However, for durations much shorter than the adiabatic limit (but still longer than the inverse of the smallest energy gaps), it is still possible to obtain very high-fidelity solutions in the perturbative limit. We discuss three approximation methods, recalling that we restrict ourselves to non-overlapping, traceless controls for simplicity.

6.3.1   Schrieffer-Wolff (SW) Expansion

To expand the exact multi-state, DRAG solutions in (6.5), (6.7) and (6.8) one can use a power series in the inverse gap energies, which we shall refer to as Δ_j. We express the diagonalization operator in the SW form [135], $\hat{W}(t) = \exp(\hat{S}(t))$. Since the transition elements (the controls) are time-dependent, the SW transformation must be amended to include time-dependence [41, 204]. As detailed in chapter 5 the effective Hamiltonian is

then given by

$$\hat{H}_{\text{eff}} = \sum_n \frac{1}{n!}[\hat{H}, \hat{S}]_n - i \sum_n \frac{1}{(n+1)!}[\dot{\hat{S}}, \hat{S}]_n, \qquad (5.3)$$

where $[\hat{A}, \hat{B}]_n = [[\hat{A}, \hat{B}]_{n-1}, \hat{B}]$ and $[\hat{A}, \hat{B}]_0 = \hat{A}$. Contrary to the exact DRAG solutions in (6.5), (6.7) and (6.8), the standard SW method determines a *single* frame transformation $\hat{S} = \sum_j \hat{S}^{(j)}$ to orders j in the small parameter u/Δ. Let us start with the case of canceling a single harmful transition Δ_k, corresponding to a term $u_k(t)\hat{h}_k + u_k^*(t)\hat{h}_k^\dagger$ in the initial frame. The required generator of $\hat{W}$ that diagonalizes the j-th order error is $\hat{S}_k^{(j)}(t) = (w_{k,j}(t)\hat{h}_k - w_{k,j}^*(t)\hat{h}_k^\dagger)/\Delta_k$. The $w_{k,j}$ correspond to j-th order error terms in the dressed frame (so $w_{k,0} = u_k$). In general, multiple transitions will be detrimental, and their total effect can be captured by $\hat{S}^{(j)} = \sum_k \hat{S}_k^{(j)}$.

To guarantee convergence one must be sure to count orders correctly [165]. In the next subsection we proceed to show that $\mathcal{O}(\partial_t u_{k,j}(t)) = \mathcal{O}(u_{k,j}(t)\Delta_k)$, so that the inertial term in (5.3) can be as important as the first term – as is true for the superadiabatic expansion – thus making counterdiabatic terms crucial. Given this ordering of errors, one can determine counterdiabatic corrections $u_{k,j}$ to control k from the dressed error $w_{k,j}$, either by direct application or by j-th order Taylor expansion of the inverse transformations.

In the spirit of the superadiabatic expansion one may alternatively cancel $k = 1, \ldots, M$ transitions Δ_k using MN generators $\hat{S}_k^{(j)}$ iteratively with $j = 1, \ldots, N$. The analog to the superadiabatic expansion is to pick instead $\hat{W} = \prod \hat{V}_l$ with $\hat{V}_l = \exp(\hat{S}_k^{(j)})$, where the indices k and j are uniquely combined into a single index $l \equiv (k, j)$ running from $1, \ldots, MN$. We compute the l-th effective Hamiltonian recursively via the relation

$$\hat{H}_l = \sum_n \frac{1}{n!}[\hat{H}_{l-1}, \hat{S}_l]_n - i\dot{\hat{S}}_l \qquad (6.9)$$

and require that all j-th order terms be canceled before diagonalizing the next order in the small parameter. Indeed, for $j = 1$, this corresponds to the first-order error expansion of the superadiabatic series, where transitions as before can also be uncontrolled or overconstrained. Thus, when a diabatic term cannot be canceled with a counterdiabatic Hamiltonian, it remains the same order in the small parameter, but of one higher iteration order in the superadiabatic frame numbering. Depending on the available controls or chosen superadiabatic frame, the SW procedure may feature several solutions to remove a given order of error [41].

6.3.2 Fourier Spectrum

A common method in spectroscopy [158] is to use the Fourier transform
(FT) of the input fields to estimate the excitation of transition elements in
the Hamiltonian. Remarkably, this approach reproduces [165] the first order
($j = 1$) transitionless SW expansion, connecting the concepts of adiabaticity
and spectroscopy.

In the rotating frame of the energies in the system, transition elements will
take the form $u_k(t)e^{-i\Delta_k t}\hat{h}_k + u_k^*(t)e^{i\Delta_k t}\hat{h}_k^\dagger$. The spectral response is given by
the finite-time FT, that is $\mathcal{F}(u,\Delta) \equiv \int_0^{t_g} u(t)e^{-i\Delta t}\,\mathrm{d}t$. The counterdiabaticity
condition can be rephrased via the identity

$$\mathcal{F}(u,\Delta) = \mathcal{F}\left(\frac{i^r}{\Delta^r}\frac{\mathrm{d}^r u(t)}{\mathrm{d}t^r}, \Delta\right) = 0, \quad \forall r \geq 1, \tag{6.10}$$

which follows directly from r-fold integration by parts when all r boundary
terms go to zero. Thus, the spectrum of a single control u at frequency Δ_k
will be canceled out when we add the counterdiabatic Hamiltonian $\hat{H}_{\mathrm{cd}}(t) =
-\frac{i}{\Delta_k}\frac{\mathrm{d}}{\mathrm{d}t}(u(t)\hat{h}_k - \mathrm{h.c.})$, corresponding to $r = 1$ in equation (6.10), or any of the
higher derivative corrections. Equality (6.10) also explains why both terms
in (6.9) are of the same order. In particular, where the FT describes the
dynamics well (small error terms, or $\mathcal{F}(u,\Delta) \ll 1$) is also where the effect of
$|\hat{\check{S}}_l\Delta|$ and $|\partial_t\hat{S}_l|$ should be very similar. This corresponds to the regime of high
quality Q for the optimal superadiabatic frame (6.3), where the divergence
of the series can be explained by the additional harmful effect of higher order
terms in SW beyond the FT approximation.

The n-th derivative in the FT solution (6.10) corresponds to the supera-
diabatic corrections from the n-th iteration [203], and, as in the cases above,
we can combine these to solve for multiple unwanted diabatic terms simul-
taneously, with gaps Δ_k respectively. We choose the ansatz control field
$u(t) = b(t) + \sum_{r=1}^N a_r i^r \frac{\mathrm{d}^r}{\mathrm{d}t^r}b(t)$, where $b(t)$ is any smooth base waveform such
as a Gaussian pulse, to find the linear system of algebraic equations

$$1 + \sum_r a_r(\Delta_k)^r = 0 \qquad \forall k, \tag{6.11}$$

and solve for the coefficients a_r. The base waveform $b(t)$ and its derivatives
need to start and end at zero for equation (6.10) to hold. Solving system
(6.11) for N transitions gives

$$u = b - i\sum_k \frac{\partial_t b}{\Delta_k} - \sum_k \sum_{j>k} \frac{\partial_t^2 b}{\Delta_k \Delta_j} + \ldots + \frac{(-i)^N \partial_t^N b}{\Delta_1 \Delta_2 \cdots \Delta_N}. \tag{6.12}$$

Other possible solutions exist when derivatives of higher order than N are used. Equation (6.11) also corresponds to the exact DRAG solution when driving systems of harmonic oscillators [203].

6.3.3 Magnus Expansion

The FT forms the first order (average Hamiltonian) term in the so-called Magnus series [159, 205] which gives an exact analytic expression for the propagator over a finite time window, as introduced in equation (5.21). The series has different convergence criteria than SW, because the integrals, rather than the time-instantaneous terms, need to be small. The Magnus series generally takes a more involved iterative form than SW, but often it is sufficient to truncate the series at the second order. Note that the series does not intrinsically enforce adiabaticity, but counterdiabaticity can be built in via relation (6.10).

In addition to counterdiabatic terms, unwanted transitions can be removed by solving the (underconstrained) diagonalization conditions obtained from the Magnus Hamiltonian terms using any extra controls (similarly to SW). In particular, any off-resonant error term can be directly removed by driving at the transition frequency with the opposite weight, i.e. spectral shaping [158, 165]. A solution that combines counterdiabaticity with spectral shaping using the Magnus expansion is the Weak AnHarmonicity With Average Hamiltonian (WAHWAH) pulse sequence [122, 195], which will be discussed in the next section. To improve experimental practicality, it is often desirable to work with a small smooth basis of time-domain waveforms, such as derivatives of Gaussians or Fourier components [195].

6.4 Physical Examples

We review some experimentally relevant applications of the DRAG framework. The basic motivations and results are summarized for each.

6.4.1 Single-qubit Leakage via Schrieffer-Wolff

State-of-the-art superconducting qubits, such as Transmon qubits, are well modeled by a standard nonlinear oscillator [34, 169] as introduced in section 5.2. Their j-th energy level in the rotating frame is given by $\omega_j(t) = j\delta(t) + \Delta_j$, with anharmonicities Δ_j (cf. equation (5.17)), and $\delta(t) = \omega_q(t) - \omega_d$ is the detuning of qubit ω_q from the carrier ω_d. Typically, $|\Delta_2| \sim 0.05\omega_q$, so that leakage to higher near-resonant states deteriorates performance. The rotating
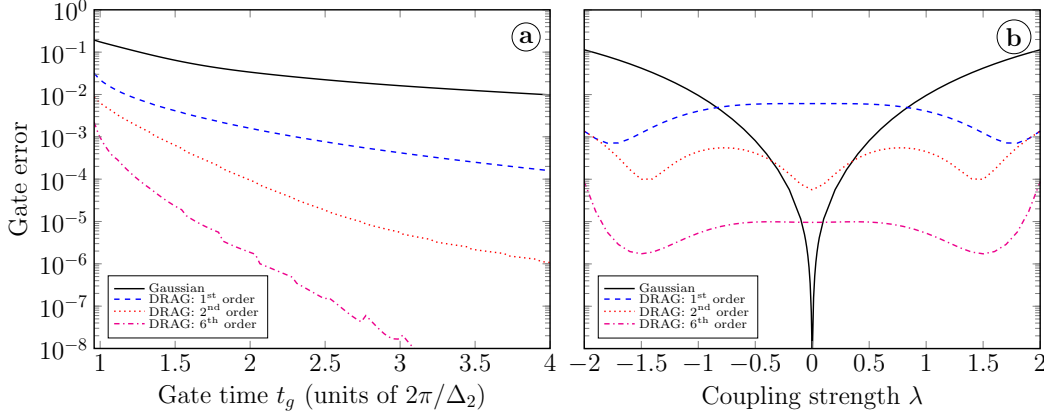
FIG. 6.1 – (a): Performance of unoptimized DRAG variants as a function of gate time, derived from an iterative Schrieffer-Wolff expansion (6.3) to higher orders. Target : $\hat{\sigma}_x$ rotation of a single qubit described by the lowest three levels of Hamiltonian (6.13). – (b): Performance of the DRAG pulses used in (a) for a fixed gate time $t_g = 4\pi/\Delta_2$ as a function of coupling strength λ to the leakage level.

frame Hamiltonian can be written as [41]

$$\hat{H}(t) = \sum_{j=1}^{d-1} \left[\omega_j(t)\hat{\Pi}_j + \sum_{\alpha}^{x,y} \lambda_{j-1} \frac{u_\alpha(t)}{2} \hat{\sigma}_{j-1,j}^\alpha \right]. \tag{6.13}$$

Here, we used the effective Pauli spin operators $\hat{\sigma}_{j,k}^x = |j\rangle\langle k| + |k\rangle\langle j|$ and $\hat{\sigma}_{j,k}^y = -i\,|j\rangle\langle k| + i\,|k\rangle\langle j|$ for $k > j$ and the projector $\hat{\Pi}_j = |j\rangle\langle j|$. The coupling constants λ_j are well approximated by those of a harmonic oscillator, i.e. $\lambda_j \approx \sqrt{j}$. Utilizing expansion (5.3) we decouple the qubit subspace $\{|0\rangle, |1\rangle\}$ from the remaining Hilbert space by choosing $\hat{V} = \exp(-i\hat{S})$ with

$$\hat{S}(t) = \sum_j s_{z,j}(t)\hat{\Pi}_j + \sum_{\alpha}^{x,y} \sum_{j<k} s_{\alpha,j,k}(t)\hat{\sigma}_{j,k}^\alpha. \tag{6.14}$$

Based on the discussion in 6.3.1 we expand each $s_{\alpha,j,k}(t)$ in a power series of a small parameter $\epsilon = 1/\Delta_2 t_g$ to obtain respective solutions $s_{\alpha,j,k}^{(n)}(t)$ to arbitrary order n. Following the calculations in Ref. [41] we find conditional equations for the $s_{\alpha,j,k}^{(n)}(t)$ to any order. Note that these equations reveal a set of free parameters, allowing for multiple solutions to the same order in ϵ. For instance, a prominent solution in lowest order features a y-only correction, that is $u_y = -\dot{u}_x \lambda_1/2\Delta_2$ and $\delta = 0$.
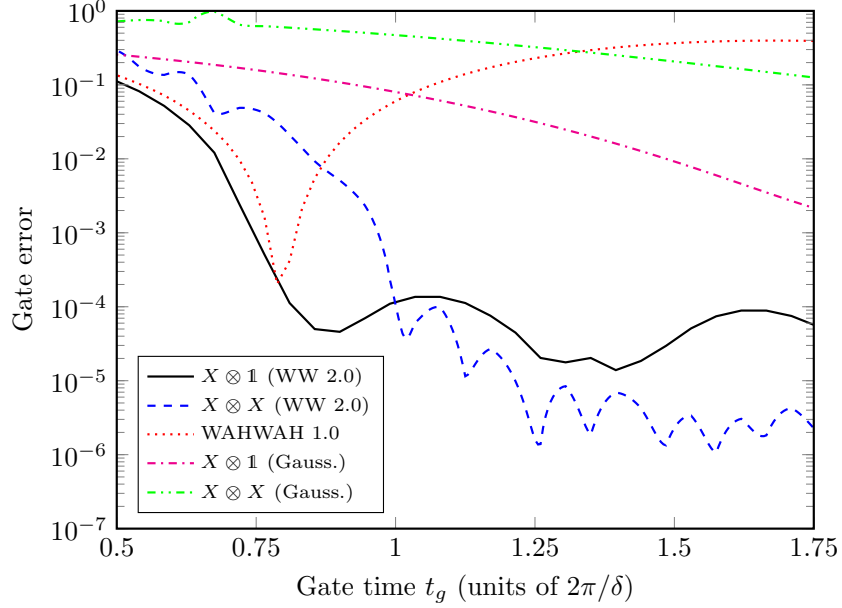
FIG. 6.2 – Gate error as a function of gate time for WAHWAH controls (1.0 and 2.0). Separate single-qubit rotations and simultaneous rotations both share a speed limit at about $2\pi/\delta$. Gaussian pulses perform orders of magnitude worse than WAHWAH control, both for separate and simultaneous rotations. Performance of derivative-based DRAG pulses is similar to that of Gaussians.

To obtain higher order solutions it is preferable to use iterative transformations along the lines of equation (6.9). The performance of solutions to different orders, obtained via iterative transformations, is depicted in FIG. 6.1a as a function of pulse length, and in FIG. 6.1b as a function of coupling strength λ for a fixed gate time $t_g = 4\pi/\Delta_2$. Higher order solutions are taken from [165]. Note also that when the $|0\rangle \leftrightarrow |2\rangle$ transition is controlled via an additional corresponding frequency component, exact solutions to the three-level system exist (cf. chapter 8 in [206]).

6.4.2 Crosstalk in Multi-Qubit and Qutrit Systems

A standard quantum control problem is the selective addressability of a two-level system in the spectral vicinity of other such systems, as occurs for instance in nuclear magnetic resonance (NMR) [207]. This problem is well adapted to a multi-diabatic control solution where weighted sums of different derivatives cancel all excitations in aggregate on the unwanted transitions [165], as in solutions (6.8) or more simply (6.12).

When additional, crowded leakage levels are present, it has been shown to be advantageous to use sideband modulated controls, based on the Magnus expansion methodology in section 6.4.2. This so-called WAHWAH solution [122, 195] uses a sideband modulated Gaussian principle control in conjunction with an auxiliary DRAG pulse. Typical parameters of such a scenario are qubit frequencies $\omega_{q,j} \sim 5$GHz, anharmonicities $|\Delta_2| \sim 300$MHz and crowded transitions $\omega_{q,2} + \Delta_2 = \omega_{q,1} + \delta$ with $\delta \sim \omega_q/100$. The x-quadrature of the control field is supported by first order DRAG $u_y = -\dot{u}_x/2\Delta_2$ to minimize leakage within a qubit, and sideband modulated to cancel crowded transitions,

$$u_x(t) = A_0 e^{-\frac{(t-t_g/2)^2}{2\sigma^2}} \left\{ 1 - \cos\left(\omega_x \left[t - \frac{t_g}{2} \right] \right) \right\}. \qquad (6.15)$$

Here, A_0 enforces the desired rotation angle and σ gives the standard deviation. At first [122], a modulation with $\omega_x = \delta/2$ was suggested (we refer to this as WAHWAH 1.0). As shown in FIG. 6.2, these controls can achieve errors $\mathcal{O}(10^{-4})$, below conventional error thresholds. However, WAHWAH 1.0 is limited to work for specific gate durations t_g, and only one qubit may be driven at once. To overcome these limitations, the method was generalized in [195], suggesting an optimal sideband modulation $\omega_x = \omega_x(t_g, \delta)$. The significant improvement over Gaussian controls is illustrated in FIG. 6.2 for the original (1.0) and improved version (2.0) of WAHWAH pulses. For details, particularly about the implementation of simultaneous gates using a smooth basis of Sine functions, we refer the reader to Ref. [195]. WAHWAH 1.0 was experimentally demonstrated in [208].

6.4.3 Experimental DRAG and Pulse Calibration

Turning to the experimental implementation [181, 182] of DRAG pulses: In practice, actual system parameters differ somewhat from those assumed in theory due to characterization gaps, system drift, or unknown transfer functions affecting the input field shapes [170]. As a simplification, we assume the low order terms in DRAG are easier to implement as their shape will be mostly maintained on entry into the dilution fridge. Even so, many different low-order variants of DRAG have been found in the literature for third-level leakage [40, 41, 165, 182]. This reduced functional form can further be optimized theoretically [195] and/or through a closed-loop process experimentally [129, 130] to account for the effect of higher order terms and experimental uncertainties (preferably using more advanced gradient-free algorithms such as CMA-ES [125]). A systematic experimental study of the tune-up of the prefactors in front of the functional forms for the control operators was performed in [190].
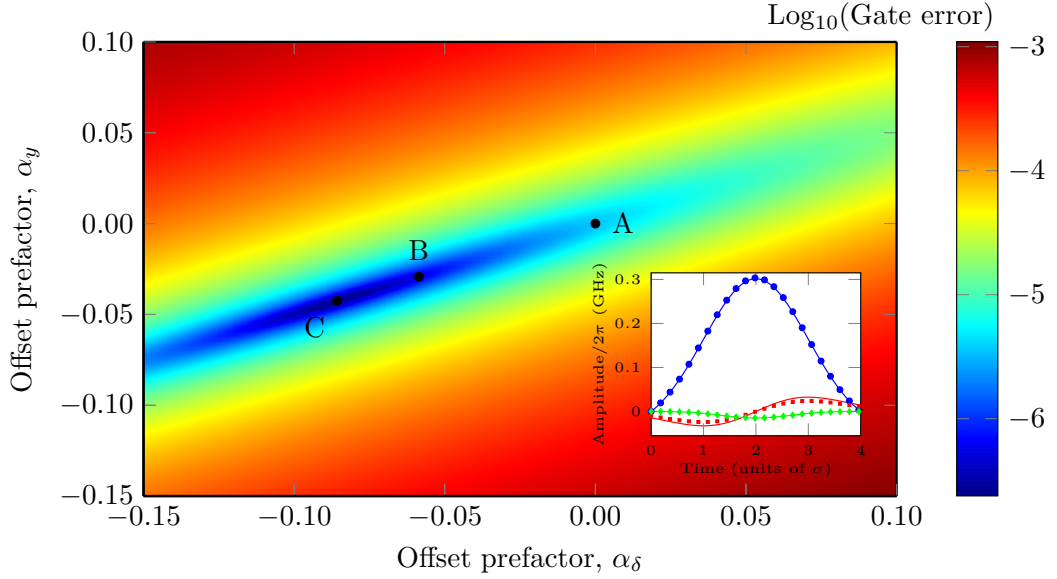
FIG. 6.3 – A slice of the 3D calibration landscape for DRAG solution up to the first order in the small parameter to the qubit σ_x-gate leakage problem. Point A and B denote [40]'s and [41]'s first-order solutions, respectively. Point C is the optimum for this control function subspace (here $\alpha_x = -0.0069$), with infidelity of $10^{-6.63}$. A successful calibration process will typically start at a known DRAG solution, i.e. points A or B, and conclude in point C. The inset illustrates the associated pulse shapes: markers represent the unoptimized shapes (u_x: ●, u_y: ■, δ: ♦) whereas solid lines depict the corresponding optimal solution (C).

For instance, let us denote the Gaussian pulse implementing a $\hat{\sigma}_x$ gate for the qubit by $G(t)$. Then the first order solutions described in [40, 41, 165] are parameterized by the limited functional basis $u_x \propto G$, $u_y \propto \partial_t G$ and $\delta \propto G^2$, which mimics the limited shaping control that can exist in experiment. None of the reported solutions are optimal within this functional basis: For typical example parameters, infidelities may be further reduced from $10^{-5.28}$ to $10^{-6.63}$ by slightly adjusting the prefactors of the control fields. For example, [40]'s first order DRAG solution may be transformed according to $u_x \to (1 + \alpha_x)u_x$ and similarly for u_y and δ, and then the constants α_x, α_y and α_δ are optimized. A discussion for why optimization within a severely restricted functional subspace may often be sufficient is given in [209] and follow-up publications. A schematic of the the optimization task involved in the calibration, as well as the shape of the associated controls, is shown in FIG. 6.3.

6.4.4 Interacting Spectrally-Crowded Rydberg Atoms

While DRAG has its origin in the field of superconducting qubits, it has also shown promise in atomic systems (specifically trapped Rydberg atoms): Using a combination of DRAG control shaping and analytical optimization of the trap design, a proposal for errors below the conventional error threshold of 10^{-4} in a room temperature environment for entangling gates based on the Rydberg-blockade was made in [98] and will be detailed in chapter 7. Spectral shaping of the control field in form of equation (6.12) is used to reduce leakage into several nearby Rydberg states other than the target state, and to further minimize blockade leakage. Such shaping techniques can also reduce gate times and leakage errors in other Rydberg-level based proposals for entanglement [202].

6.4.5 Motional States of Atoms

The anharmonic oscillator states that describe Josephson junction qubits are isomorphic to vibrational states of atoms in optical lattice potentials [210]. Thus, most of the techniques in the above examples directly translate to non-harmonic traps [193].

6.4.6 Microwave-Entangled Transmons

Because coupled superconducting quantum systems retain their dense level structures, the ideas from the DRAG counterdiabatic framework are applicable to entangling operations as well (cf. chapters 9 and 10 in [206]). This includes adiabatic passage type gates, often used with Xmon qubits [150], but it is especially applicable to microwave entangling gates [187, 192, 211–214], which are transition-selective, e.g. the cross-resonance gate [215]. Together with applications in high-fidelity single-qubit gates [183, 190] DRAG controls made a crucial contribution to the demonstration of a universal gate set in superconducting qubits [185].

6.4.7 Rotating Wave Approximation (RWA)

The ubiquitous approximation is used when resonantly driving quantum transitions [170]. Physically, it corresponds to neglecting diabatic multi-photon transitions (e.g. in Floquet theory [191]) and these errors can also be suppressed [165]. For counter-rotating terms at frequency 2ω, the DRAG solution amounts to correcting the Rabi drive with $\Omega(t)\hat{\sigma}_x - \dot{\Omega}(t)\hat{\sigma}_y/2\omega$.

6.4.8 Spin Resonance Systems

The above treatments can also apply to two-level systems, for example to suppress crosstalk e.g. from global magnetic fields in NMR [165]. Besides, DRAG has potential applications in quantum dots [194].

6.4.9 Λ-Systems and Sideband Transitions

Multi-photon transitions are also used in adiabatic and resonant pulses, and can also suffer from diabatic errors to unwanted states [152]. This has inspired DRAG-like extensions to STIRAP pulses [216] as well as similar solutions to multi-photon Raman pulses (cf. chapter 10 in [206]).

6.4.10 Fast Dispersive Measurement

DRAG pulses have also found use for open-system control, being valuable in measurement dynamics where the readout apparatus must be used and reset quickly to avoid relaxation [183, 189]. In particular, equation (6.12) gives a solution to measuring N qubit states via corresponding readout resonator modes where we replace the gap energies by inverse Lorentzians, $\Delta_j \equiv \delta_j + i\kappa/2$ [203]. This forces fast (super)adiabatic following on a network of one or more decaying cavities, thereby exactly solving equation (6.8).

6.5 Conclusion

The DRAG framework can be understood as an iterative counterdiabatic expansion which specifically allows to confine the solution space to attainable controls of a given system. DRAG solutions are constructed to simultaneously allow suppression of multiple transitions, also if available controls affect transitions other than intentionally driven ones. In general, exact analytic solutions to the underlying systems of equations are intractable. We presented three common perturbative approaches to derive DRAG solutions of different orders: Via an adiabatic Schrieffer-Wolff expansion, a spectral engineering approach and solutions derived from average Hamiltonian theory. Whereas the first two are based purely on expansions in terms of derivatives, the latter constitutes a different family of solutions (WAHWAH) which incorporates sideband modulations. We note that different expansion methods treat higher orders differently: For instance, while a lowest order Magnus expansion reproduces the spectral engineering solutions that can be derived from a superadiabatic expansion, higher orders of both expansions differ significantly.

Chapter 7

Few-parameter Entanglement of Rydberg Atoms

The work presented in this chapter shows how a combination of the DRAG method, as introduced in chapter 6, and optimized trap parameters can be used to significantly improve fidelities of the Rydberg blockade entangling gate compared to previous implementations. The Rydberg blockade mechanism introduced in [217] allows for the implementation of a controlled phase gate which, by the use of Hadamard gates, recovers a maximally entangling CNOT gate. We will now briefly discuss the basics of the Rydberg blockade gate before moving to a more elaborate analysis. As illustrated in FIG. 7.1 the controlled phase gate is implemented with a sequence of three pulses, each of which resonant to the transition $|1\rangle \leftrightarrow |r\rangle$: First, a π pulse acts on the control atom, followed by a 2π rotation on the target atom. The last pulse is another π rotation on the control atom. From FIG. 7.1a we see that the pulse sequence induces zero phase $\Delta\varphi_t = 0$ since, when the system is initialized in state $|00\rangle$, none of the pulses is capable of exciting the atoms to their Rydberg state. For input states $|10\rangle$ and $|01\rangle$ either only the two π pulses or only the full 2π rotation drive population through the Rydberg state $|r\rangle$ and thereby induce a net phase change $\Delta\varphi_t = \pi$. Now, as shown in FIG. 7.1b, for input state $|11\rangle$ the first π pulse excites the control atom to its Rydberg state. The strong dipole-dipole interaction between Rydberg states (see section 2.3) leads to an energy shift of the Rydberg state of the target atom. We refer to this energy shift as the *Rydberg blockade* $\mathsf{B_0}$. If the

---
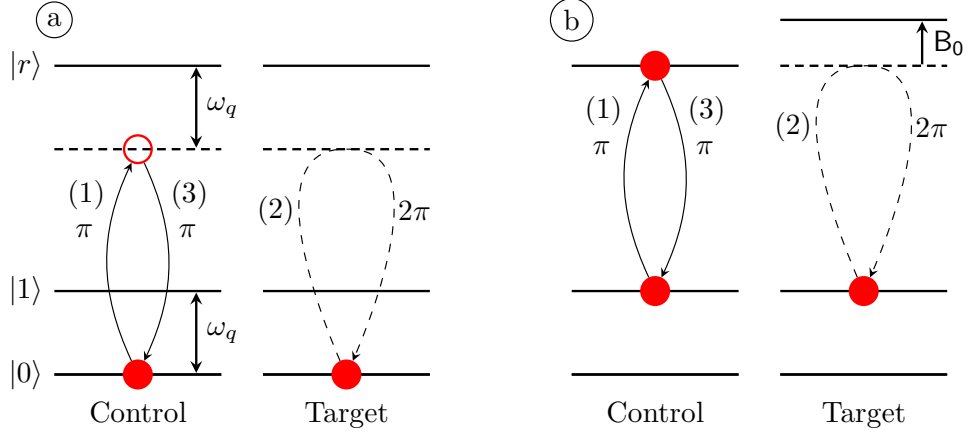
FIG. 7.1 – Pulse sequence that implements a controlled phase gate via the Rydberg blockade, operating on the input states $|00\rangle$ (a) and $|11\rangle$ (b). All pulses are resonant with the $|1\rangle \leftrightarrow |r\rangle$ transition. (a): Neither of the atoms is excited to their Rydberg states, hence the net phase change $\Delta\varphi_t$ is zero. (b): The control atom is excited to its Rydberg state. The Rydberg blockade shift prevents excitation of the target atom to its Rydberg state so that the total phase acquired is $\Delta\varphi_t = \pi$.

blockade shift is large enough, there is no excitation of the target and only the control atom picks up a phase of π. In conclusion, under ideal evolution the discussed three pulse sequence implements the controlled phase gate in the form $C_Z = |00\rangle\langle 00| - |01\rangle\langle 01| - |10\rangle\langle 10| - |11\rangle\langle 11|$.

The Rydberg blockade mechanism as discussed above has been demonstrated to be capable of creating bipartite entanglement with fidelities of about 70% to 80% [89, 91]. There is good reason to believe that the fidelity achieved to date is not a fundamental limit, but is due to experimental perturbations and the high sensitivity of Rydberg states to external fields [92]. With the expectation that experimental techniques will continue to improve, it is important to address the question of the intrinsic fidelity limit of the Rydberg blockade gate. Detailed analysis with constant amplitude Rydberg excitation pulses revealed a Bell state fidelity limit of $F_B \sim 0.999$ in Rb or Cs atoms in a $300\,\mathrm{K}$ environment [218]. Other work has sought to improve on this with optimal control pulse shapes [219, 220], adiabatic excitation [221, 222], or simplified protocols that use a single Rydberg pulse [223, 224]. However, none of the analyses to date that consistently account for Rydberg decay and excitation leakage to neighboring Rydberg states have provided a fidelity better than 0.999. This leaves open the question of whether or not the Rydberg gate will be capable of reaching the 0.9999 level or better that

appears necessary for scalable quantum computation with a realistic overhead in terms of qubit numbers for logical encoding [157].

In this chapter we show that entangling Rydberg gates with fidelities $F_B > 0.9999$ are possible with Cs atoms in a $300\,\text{K}$ environment and $F_B > 0.99999$ in a $4\,\text{K}$ environment. This advance is made possible using simple and smooth analytic shaped pulses that are designed to suppress leakage at a discrete set of frequencies [40] corresponding to neighboring Rydberg states. By suppressing the leakage orders of magnitude more effectively than is possible with square, or simple Gaussian pulses, we are able to run the gate at least an order of magnitude faster than previous protocols, which is fast enough to keep the spontaneous emission error low and achieve high fidelity. Drastically reducing the gate time also has advantages in the short term, by avoiding the onset of other experimental errors that increase with time, such as technical noise. We find a gate time close to $50\,\text{ns}$, which is fast enough to be competitive with superconducting qubits while retaining much longer coherence times [214, 225].

7.1 Rydberg Excitation

The free evolution and gate Hamiltonians $\hat{H}_d$ and $\hat{H}_g$, respectively, of a single Rydberg atom in its lab frame, are given by ($\hbar \equiv 1$ everywhere)

$$\hat{H}_d = \omega_g \,|g\rangle\langle g| + \omega_q \,|1\rangle\langle 1| + \sum_{r'} \omega_{r'} \,|r'\rangle\langle r'| \tag{7.1a}$$

$$\hat{H}_g = u(t) \sum_{r'} \left(\frac{n}{n'}\right)^{3/2} \left(|r'\rangle\langle 0| + |r'\rangle\langle 1|\right) + \text{h.c.} \tag{7.1b}$$

whereby $|g\rangle$ denotes some auxiliary level we will use later to model decay. Here r' is shorthand for the set of quantum numbers specifying the Rydberg states and n, n' are the corresponding principal quantum numbers. The matrix elements and the Rabi coupling for single photon excitation to high lying Rydberg states scale as $n^{-3/2}$. For Cs, the ground hyperfine splitting is $\omega_q/2\pi = 9.1926\,\text{GHz}$. The set of states $\{|r'\rangle\}$ describes all relevant Rydberg states. We assume that the control $u(t)$ only negligibly couples any of these states to $|g\rangle$ and hence, without loss of generality, we set the energy of $|g\rangle$ to zero, i.e. $\omega_g = 0$. The control field has in-phase quadrature only,

$$u(t) = u_x(t)\cos(\omega_d t)\,. \tag{7.2}$$

Usually, atoms are driven on resonance with the $|1\rangle \leftrightarrow |r\rangle$ transition, so that the carrier frequency is $\omega_d = \omega_r - \omega_1$ with ω_r being the frequency of the
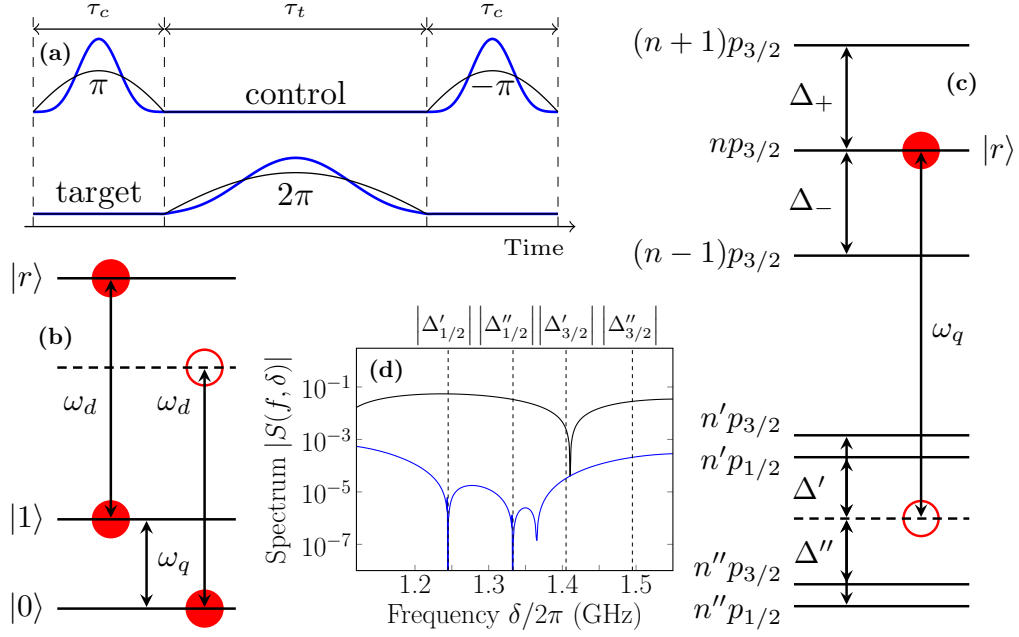
FIG. 7.2 – (a): DRAG pulse sequence (blue) and initial Gaussian waveform, (thin black) to implement a two-qubit entangling gate. Pulse lengths are τ_c and τ_t for the control and target atoms, respectively. The control amplitudes are shown on the same scale. – (b): Level diagram for one-photon Rydberg excitation with laser frequency ω_d. – (c): Detailed Rydberg level structure and detunings. The dashed line corresponds to that in part b – (d): Spectrum of pulse on control atom for Gaussian (black) and DRAG (blue) waveforms.

target Rydberg state $|r\rangle$. In order to remove any fast oscillation on the order of ω_d from the dynamics, we choose to work in a frame rotating with ω_d in the remainder of this chapter. The pulse sequence which we will use to implement a two-qubit entangling gate is illustrated in FIG. 7.2a. As we have seen earlier, this scheme implements a controlled phase gate C_Z [217], which in the computational basis $\{|00\rangle, |01\rangle, |10\rangle, |11\rangle\}$ reads $C_Z = \mathrm{diag}(1, -1, 1, 1)$. Note that this differs from the phase gate matrix of [217] due to our use of $-\pi$ instead of π for the last pulse, which eventually results in slightly better gate fidelity.

The Hamiltonian of the compound system, control and target atom, can be written as

$$\hat{H} = \hat{H}_{\mathrm{control}} \otimes \hat{\mathbb{1}} + \hat{\mathbb{1}} \otimes \hat{H}_{\mathrm{target}} + \sum_{i,j} \mathsf{B}_{r_i, r_j} |r_i, r_j\rangle\langle r_i, r_j|. \qquad (7.3)$$

Here, the B_{r_i, r_j} quantify the Rydberg interaction strength between all relevant Rydberg states $|r_i\rangle$ of the control atom and $|r_j\rangle$ of the target atom, including

all possible leakage levels depicted in FIG. 7.2c. The desired excitation is
resonant with the transition from $|1\rangle$ to $|r\rangle$, with possible leakage channels
to the $(n \pm 1)p_{3/2}$ states. The associated detunings are denoted Δ_+ and Δ_-,
respectively.

To remove leakage to $np_{1/2}$ states we assume a specific implementation in
Cs atoms where qubit state $|1\rangle$ is mapped to $|1'\rangle = |f = 4, m = 4\rangle$ before and
after the Rydberg gate. With σ_+ polarized excitation light $|1'\rangle$ only couples to
states $|np_{3/2}, f = 5, m_f = 5\rangle$ so there is no leakage to $np_{1/2}$ states, and errors
originating from couplings to multiple hyperfine states within the $np_{3/2}$ levels
are also suppressed. For compactness of notation we refer to $|1'\rangle$ as $|1\rangle$ in the
following.

In addition to leakage to the blockaded target Rydberg state during the
2π pulse, significant leakage channels (represented by the subset of states
around the dashed horizontal line in FIG. 7.2c) exist for the π pulse when the
control qubit is initialized in state $|0\rangle$. The $|0\rangle$ state is coupled to Rydberg
states $|n'p_{1/2,3/2}\rangle$ and $|n''p_{1/2,3/2}\rangle$. The Cs $6s_{1/2} - np_{1/2}$ oscillator strength is
anomalously small, as was first explained by Fermi [226], and for the states
S1, S2 of primary interest in TAB. 8.1 we estimate the ratio of Rabi coupling
strengths to $np_{1/2}$ states as compared to $np_{3/2}$ states as $< 1/300$ [227]. The
leakage to $np_{1/2}$ states in Cs with Gaussian pulses is therefore negligible.
Nevertheless, we have still included possible leakage to $np_{1/2}$ states in order
to substantiate the generality of our approach. The detunings for these tran-
sitions to $np_{1/2,3/2}$ states are denoted Δ', Δ''. In what follows we will refer to
the interaction between two target Rydberg states $|np_{3/2}\rangle$ as B_0.

7.2   Design of Control Pulses

Accurate selectivity of densely crowded Rydberg states, and corresponding
leakage errors, as described above, is a fundamental concern in quantum
information with Rydberg atoms. Hence, we will adapt the DRAG method
introduced in detail in chapter 6 to minimize these effects. Specifically, we
will engineer the spectrum of the control pulses such that blockade leakage
and leakage to neighboring Rydberg states are reduced. We will explicitly
utilize only a shaped in-phase control $u_x(t)$ and no additional out-of-phase
quadrature $u_y(t)$, which has already been suggested in earlier work [41]. This
simplifies the experimental implementation significantly.

For convenience, we briefly review the fundamental properties of such
DRAG controls. Suppose the spectral power at certain frequencies $\{\delta_j\}$ with
$j = 1, \ldots, m$ is to be canceled. Hereto, closely related to the procedure in

section 6.3.2, we choose the ansatz

$$u_x(t) = u_x^{(0)}(t) + \sum_{k=1}^{N/2} \alpha_{2k} \frac{\mathrm{d}^{2k} u_x^{(0)}(t)}{\mathrm{d}t^{2k}}, \tag{7.4}$$

where $N = 2m$ and $u_x^{(0)}(t)$ is some smooth initial shape, e.g. a Gaussian pulse, which meets the necessary requirements for the Fourier transform expansion (6.10) to be applicable. The analog to the system of equations (6.11) then becomes

$$1 + \sum_{k=1}^{N/2} \alpha_{2k} \left(-i\delta_j\right)^{2k} = 0, \quad j = 1, \ldots, m. \tag{7.5}$$

For instance, if two leakage transitions at frequencies δ_1 and δ_2 are to be suppressed, the corresponding real-valued solutions for the coefficients α_k in equation (7.4) read $\alpha_2 = 1/\delta_1^2 + 1/\delta_2^2$ and $\alpha_4 = 1/(\delta_1^2 \delta_2^2)$. Formally, solutions to the system of equations (7.5) will feature imaginary degrees of freedom: For the given example of $m = 2$, there will be free parameters α_1 and α_3 that correspond to potential out-of-phase controls. Yet, they can be chosen at will and are set to zero in order for the control pulses to be restricted to the in-phase quadrature only.

7.3 Gate Analysis

7.3.1 Population Error

We proceed to demonstrate how Gaussian pulses with DRAG components help to improve over previous methods by several orders of magnitude. Since the main advantage of Gaussian and DRAG shapes is an exponential suppression of leakage, we first focus on population error arising from leakage channels to other Rydberg states, as illustrated in FIG. 7.2c. For our simulations we use the system parameters that are listed in TAB. 8.1. The two different settings, S1 and S2, respectively, belong to two possible one-photon-excitation schemes starting from the Cs $6s_{1/2}$ state. Leakage errors are expected to be worse in S2 due to smaller energy splittings at higher Rydberg states, whilst lifetimes in S2 are better by roughly a factor of two. As initial pulses for DRAG and Gaussian control, we utilize generalized Gaussians of duration t_g

$$u_x^{(0)}(t) = G(t) \equiv A_\theta \left[\exp\left(-\frac{(t - t_g/2)^2}{2\sigma^2}\right) - \exp\left(-\frac{(t_g/2)^2}{2\sigma^2}\right)\right]^{N+1} \tag{7.6}$$

Parameter	Value		Parameter	Value	
	S1	S2		S1	S2
n	107	141	τ_n (μs)	538	969
n'	106	138	$\Delta_+/2\pi$ (GHz)	-5.534	-2.507
n''	105	137	$\Delta_-/2\pi$ (GHz)	5.694	2.562
$\Delta'_{1/2}/2\pi$ (GHz)	-2.961	-1.245	$\Delta'_{3/2}/2\pi$ (GHz)	-3.161	-1.333
$\Delta''_{1/2}/2\pi$ (GHz)	3.256	1.495	$\Delta''_{3/2}/2\pi$ (GHz)	3.051	1.405
$\mathsf{B}_0/2\pi$ (GHz)	1.54	0.68	$b_{n,n}$	1	
$b_{n,n'}$	0.85		$b_{n,n''}$	0.80	
$b_{n,n+1}$	1.02		$b_{n,n-1}$	0.97	

Table 7.1 – System parameters for the simulation of Rydberg blockade entangling gates using $np_{3/2}$ states in Cs for two different single-photon excitation schemes, S1 and S2, at temperature $T = 300$ K. Lifetimes are calculated using expressions in [229]. The relative blockades $b_{n,m}$ between Rydberg states $|r\rangle$ and $|r_i\rangle$ with principal quantum numbers n, m are given in units of B_0.

with a standard deviation $\sigma = 2t_g/3$ and a pulse area θ determined by the value of A_θ [228]. The exponent $N + 1$ ensures that the first $N = 2m$ derivatives of the Gaussian vanish at the boundaries of the time window, $t = 0$ and $t = t_g$. Note that N here is the same as for instance in equation (7.4), so that we meet the conditions for equation (7.5) to hold. Unless stated otherwise, we fix the pulse length τ_c for the $\pm\pi$-pulses on the control atom to $\tau_c = \tau_t/2$. In FIG. 7.3 we show the overall population error for a Rydberg blockade entangling gate according to the pulse sequence given in FIG. 7.2a. Conventional square pulses perform very poorly due to a high degree of leakage. Gaussian pulses (we always compare Gaussian and DRAG pulses with equal values of N) show an improvement by two to two and a half orders of magnitude over the square pulse sequence. This is attributed to Gaussians exponentially suppressing excitations to off-resonant transitions in the Fourier space, whilst square pulses only achieve a polynomial suppression.

Leakage can further be reduced by minimizing the main leakage channel into the $|n'\rangle$ subset of the control atom while also avoiding blockade leakage into the target Rydberg state $|r\rangle$ of the target atom with the aid of analytical DRAG pulses, whereby control and target pulses can be shaped independently of each other. Hence, for the area π pulses we use $N = 4$ in equation (7.4) to simultaneously suppress both Δ' transitions, whereas $N = 2$ is sufficient for the 2π pulse since only leakage to the blockade-shifted target Rydberg state is significant. Note, however, that overall the error from the 2π rotation is more significant than that from the π pulse since B_0 is about half the value of Δ'.
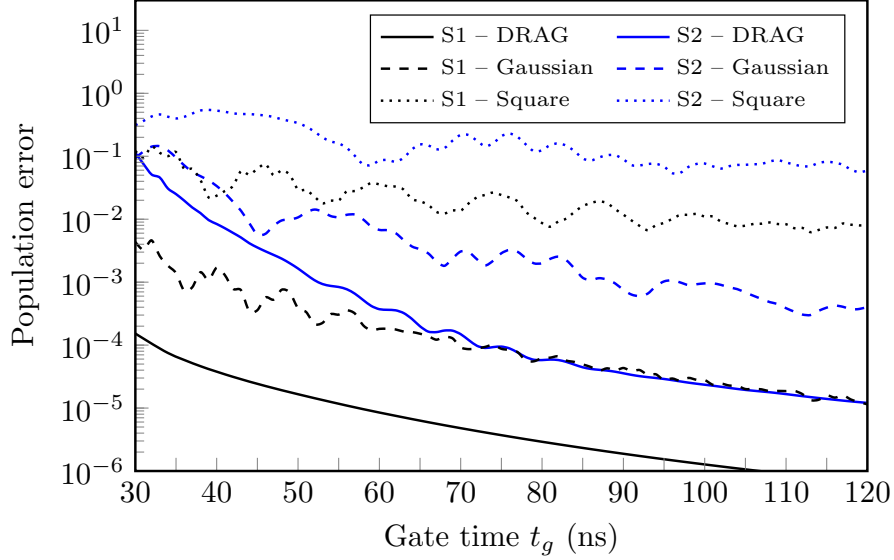
FIG. 7.3 – Population error for a two-qubit Rydberg blockade entangling gate as a function of gate time $t_g = \tau_t + 2\tau_c$. Gaussian pulses reduce leakage errors by up to 2.5 orders of magnitude compared to conventional square controls, while additional supplementation with DRAG further improves by another 1.5 orders of magnitude for reasonable gate times. The DRAG pulses are designed to minimize primarily leakage into the $|n'\rangle$ subset of the control atom as well as blockade leakage in the target atom. The Rydberg blockades $B_0/2\pi$ are 1.54 GHz and 0.68 GHz for S1 and S2, respectively.

Note also that we do not suppress the $|n''\rangle$ subset since this would require us to use $N = 8$, which in turn increases the amplitude of the control pulse u_x. The spectral argument that leads to our pulses only holds for $u_x/\delta \ll 1$ (δ being the smallest detuning) so that increasing amplitudes deteriorate the gate. Owing to the frequencies Δ' and Δ'' being very similar, the spectral power at both Δ'' transitions is sufficiently low even though they are not explicitly nulled out, as depicted in the spectrum shown in FIG. 7.2d. Using these frequency-selective shapes additionally yields another one and a half orders of magnitude improvement over Gaussians, hence improving over square pulses by up to four orders of magnitude. As expected, the best population errors are achieved in setting S1, owing to larger separations between atomic levels. Under these conditions, DRAG pulses allow to speed up gates by a factor of three compared to Gaussians, while achieving the same error. Compared to conventionally used square pulses, the speed up lies in the range of several orders of magnitude.
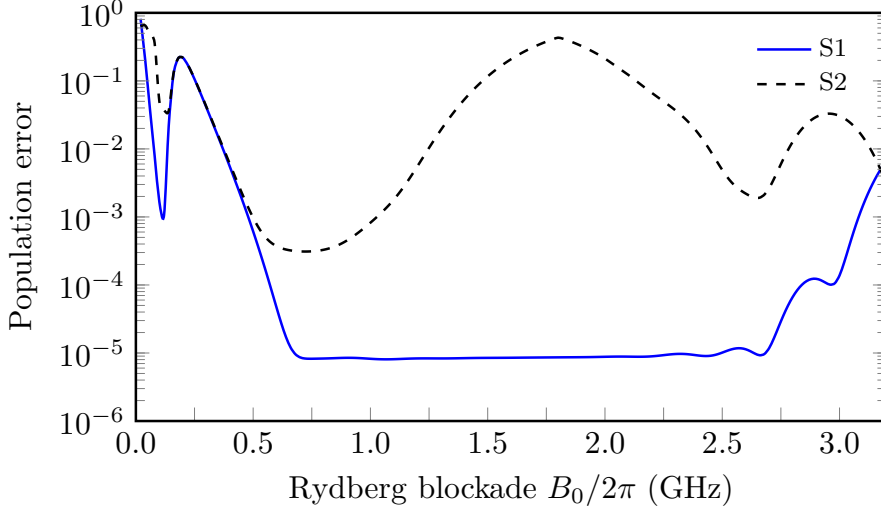
FIG. 7.4 – Population error for a fixed gate time $\tau_t = 30\,\text{ns}$ as a function of the blockade shift B_0 in settings S1 and S2. The error is minimized for a value of $\mathsf{B}_0/2\pi \sim 0.7\,\text{GHz}$ in S2. In S1, the population error is optimal for blockade shifts in the range of $0.7 - 2.7\,\text{GHz}$.

7.3.2 Optimal Rydberg Blockade

The performance of the Rydberg entangling gate strongly depends on the value of the blockade shifts. Scanning over the value of B_0 for a fixed gate time of $\tau_t = 30\,\text{ns}$ reveals that the optimal value for $\mathsf{B}_0/2\pi$ is around $1.5\,\text{GHz}$ for setting S1 and $0.7\,\text{GHz}$ for setting S2, as shown in FIG. 7.4. A qualitative explanation is based on analyzing the energy landscape of all involved Rydberg states. For this purpose, we assume for simplicity that all blockade shifts equal the target blockade, i.e. $\mathsf{B}_{r_i,r_j} \sim \mathsf{B}_0$. Starting in the initial state $\rho_{in} = |10\rangle\langle 10|$ we notice that due to Rydberg excitation by the first π-pulse, the Rydberg levels of the target atom are blockade-shifted by B_0. As a consequence, for instance the leakage transitions into the $|n''\rangle$ subset are almost resonantly driven by the 2π-pulse if $\mathsf{B}_0 \sim (\Delta''_{1/2} + \Delta''_{3/2})/2$, leading to even more undesired excitation. On the other hand, if the initial state is $|11\rangle$, too small a blockade will produce large population errors in the target Rydberg state since the 2π-pulse will significantly excite the only marginally shifted $|np_{3/2}\rangle$ state. This motivates a careful analysis of the Rydberg energies since an unsophisticated choice of B_0 might introduce severe frequency crowding issues and tremendously lower gate fidelities.

Analytically estimating the optimal value for the blockade shift is possible by minimizing excitation to harmful levels [218]. The matrix element for a transition to a Rydberg state $|n\rangle$ is proportional to $n^{-3/2}$. On the other hand,

the probability of exciting a state at detuning Δ_k scales proportionally to Δ_k^{-2} so that we can write the total probability of exciting harmful leakage states as

$$
\begin{aligned}
P_{\text{leak}} \propto{} & \frac{1}{(n+1)^3(\Delta_1 + \mathsf{B}_0)^2} + \frac{1}{(n-1)^3(\Delta_1 - \mathsf{B}_0)^2} \\
& + \frac{1}{(n')^3(\Delta_2 - \mathsf{B}_0)^2} + \frac{1}{(n'')^3(\Delta_2 + \mathsf{B}_0)^2} + \frac{1}{n^3 \mathsf{B}_0^2}.
\end{aligned}
\tag{7.7}
$$

Here, we have set $\Delta_1 = (\Delta_+ + \Delta_-)/2$ and $\Delta_2 = (\Delta'_{1/2} + \Delta'_{3/2} + \Delta''_{1/2} + \Delta''_{3/2})/4$. Finding the roots of $\mathrm{d}P_{\text{leak}}/\mathrm{d}\mathsf{B}_0$ in order to minimize the leakage probability (7.7), for instance for the parameters of setting S2, yields an optimal value for the blockade $\mathsf{B}_0/2\pi \approx 0.68\,\text{GHz}$, which is in very good agreement with the optimal value found numerically in FIG. 7.4. Note that the shape of P_{leak} can be quite flat around its exact minimum. As a consequence, it may be possible for certain setups to achieve similar performance with blockade shifts that are below the analytical estimate. The blue line in FIG. 7.4 demonstrates that setting S1 is an example of this situation: The analytical estimate is $1.54\,\text{GHz}$, which is about twice as much as the lowest optimal value $0.7\,\text{GHz}$ found via numerical optimization.

7.3.3 Entanglement Fidelity

Due to intermediate population of other Rydberg states, the ideal unitary after the sequence in FIG. 7.2a will not equal the C_Z gate that was discussed in the beginning of this chapter. Instead, the ideal evolution is given by

$$
\hat{U}_{\mathrm{C_Z}, \vec{\phi}} = \operatorname{diag}(e^{i\phi_{00}}, e^{i\phi_{01}}, e^{i\phi_{10}}, e^{i\phi_{11}}),
\tag{7.8}
$$

where $\phi_{ij} \equiv \phi_{ij,ij}$ is a shorthand notation for phases on the diagonal elements. To turn the C_Z-like gate in equation (7.8) into an entangling CNOT-like gate we follow the procedure that turns a common C_Z into a CNOT gate: Applying a Hadamard gate on the target qubit before and after the C_Z operation recovers a CNOT. Similarly for our case, we find that, instead of a Hadamard gate, a general $\pi/2$ rotation

$$
\hat{R}(\vec{h}) = \frac{1}{\sqrt{2}} \begin{pmatrix} e^{ih_{00}} & e^{ih_{01}} \\ e^{ih_{10}} & e^{ih_{11}} \end{pmatrix}
\tag{7.9}
$$

with phases $\vec{h} = (h_{00}, h_{01}, h_{10}, h_{11})$ can be used to turn, up to relative phases, the C_Z-like gate (7.8) into a CNOT. If the corresponding entangling phase $\phi_{\text{ent}} = \phi_{00} - \phi_{01} - \phi_{10} + \phi_{11}$ equals exactly π, the transformation

$$
\left(\hat{\mathbb{1}} \otimes \hat{R}(\pi, \tilde{\phi}, -\tilde{\phi}, 0) \right) \hat{U}_{\mathrm{C_Z}, \phi} \left(\hat{\mathbb{1}} \otimes \hat{R}(0, 0, 0, \pi) \right)
\tag{7.10}
$$
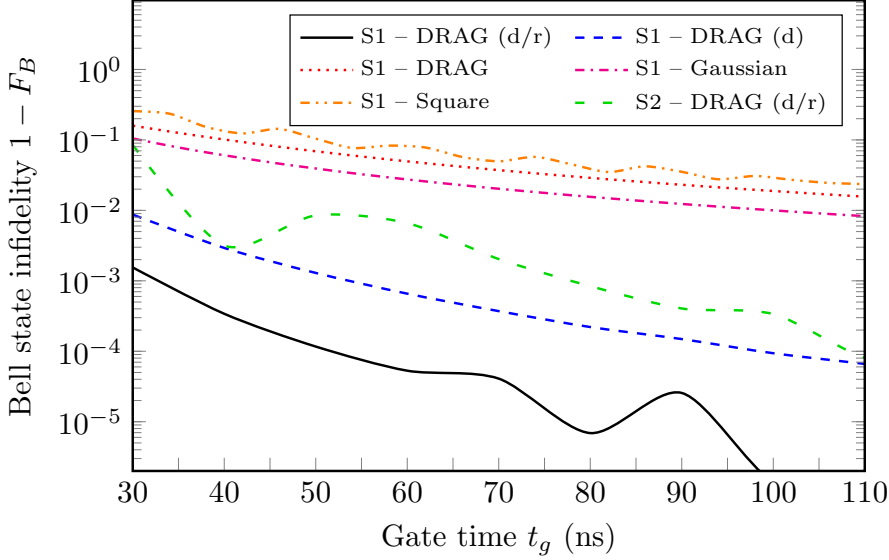
FIG. 7.5 – Unitary Bell state infidelity as a measure for entanglement generated by the pulse sequence in FIG. 7.2 using square pulses, Gaussians, DRAG, detuned (d) DRAG controls and detuned DRAG controls with rescaled (r) amplitude for setting S1, as well as optimal DRAG controls in S2. Detuning DRAG pulses on the target atom accounts for wrong phases and combines less leakage with high degrees of entanglement. The necessary detuning Λ decreases proportionally to $1/\tau_t^2$ with a value of $\Lambda/2\pi = 124.07\,\text{MHz}$ at $\tau_t = 25\,\text{ns}$.

with $\tilde{\phi} = \phi_{10} - \phi_{11}$ produces a maximally entangling CNOT-like gate. In order to quantify the degree of entanglement of our pulse sequence, we pick $(|00\rangle + |10\rangle)/\sqrt{2}$ as an initial state. Ideally, under evolution (7.10) this yields, up to local phases, the maximally entangled Bell state $|\Phi_+\rangle = (|00\rangle + |11\rangle)/\sqrt{2}$. To quantify the performance we evaluate the state overlap fidelity (4.2) between two density matrices ρ and ρ_t according to

$$F_2 = \left(\text{Tr}_\mathcal{Q} \left\{ \sqrt{\sqrt{\rho}\rho_\text{id}\sqrt{\rho}} \right\} \right)^2. \tag{4.2}$$

Here, we partially trace over the computational subspace $\mathcal{Q}$, spanned by the computational basis states $\{|00\rangle, |01\rangle, |10\rangle, |11\rangle\}$, to disregard irrelevant information about non-computational states.

For the specific target state $\rho_\text{t} = |\Phi_+\rangle\langle\Phi_+|$ we refer to the fidelity as *Bell state fidelity* F_B. The corresponding results are depicted in FIG. 7.5, whereby we assume that the $\pi/2$ gates on the qubit subspace are perfect. We observe that Gaussian controls seem to achieve better results than a naive DRAG

control. However, the main reason for DRAG pulses to perform poorly at a first glance is wrong phases. In the first publication of DRAG, a real-time control of the carrier frequency ω_d accounts for such phase errors [40].

However, it is also possible to employ a constant detuning Λ from resonance, i.e. $\omega_d = \omega_r - \omega_q + \Lambda$ [195], with the benefit of less experimental effort being required. We find that detuning only the 2π rotation of the target atom is sufficient to achieve low enough errors. As a consequence of off-resonant driving, rotation errors will be induced which can be compensated by slightly rescaling the pulse amplitudes (up to at most 3% for the fastest gates). The difference between the solid black and the dotted red lines in FIG. 7.5 demonstrates that the combination of constant detuning and a rescaled amplitude indeed account for both errors, yielding at least two orders of magnitude improvement over Gaussian waveforms. As one would expect from previous results [40], the optimal detuning is proportional to the Rabi frequency squared, yielding approximately a $1/\tau_t^2$ power law. In order to obtain the optimal detuning Λ as a function of gate time we ran a single-parameter optimization using the Nelder-Mead algorithm described in section 4.2.1. The functional dependence of the optimal detuning is illustrated in FIG. 7.6. We find that we are able to produce Bell states with a fidelity of 0.9999 for $t_g \sim 50$ ns using detuned DRAG pulses with amplitude correction.

An alternate approach to account for phase issues is by waiting an appropriate time t_{gap} between the pulses [89], or to track phases in software and correct for them afterwards. The former approach will noticeably prolong the gate times compared to our approach. Overall, detuned DRAG pulses yield an improvement of more than two orders of magnitude compared to conventional shapes. Furthermore, the necessary gate times are less than 10^{-7} of the few second coherence times that have been demonstrated with neutral atom qubits [86], substantiating that Rydberg gates are a promising approach for scalable quantum computing.

7.3.4 Including Spontaneous Emission

All results in the previous section are based on unitary evolution of the atoms. A more realistic model incorporates decay due to finite lifetimes of the energy levels. We employ Lindbladian dynamics to simulate the effects of decoherence, whereby we assume that population of Rydberg levels decays by a fraction of 7/8 into some auxiliary level $|g\rangle$ that has no effect on the rest of the dynamics. The residual part equally decays into the qubit states $|0\rangle$ and $|1\rangle$. Hence, the full dynamics of our system are governed by the Lindblad
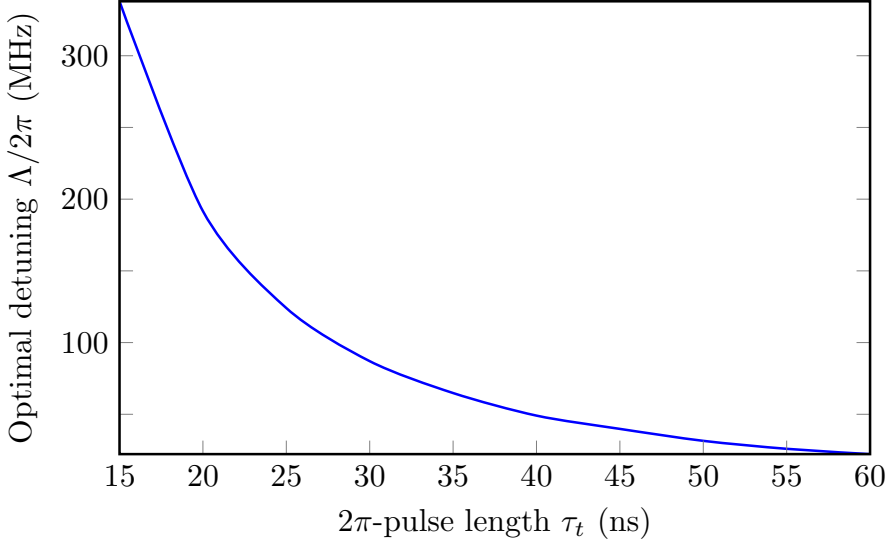
FIG. 7.6 – Optimal detuning of the 2π DRAG pulse on the target Rydberg atom as a function of pulse length for the parameters of setting S1, found via a single-parameter Nelder-Mead optimization. The detuning Λ decreases proportionally to $1/\tau_t^2$ with a value of $\Lambda/2\pi = 124.07\,\mathrm{MHz}$ at $\tau_t = 25\,\mathrm{ns}$, which is in agreement with related results [40] that suggest the optimal detuning to be proportional to the squared Rabi amplitude.

master equation (3.4) for the density operator $\hat{\rho}$,

$$\dot{\hat{\rho}} = -i[\hat{H}, \hat{\rho}] + \sum_r \gamma_r \left(\hat{L}_r \hat{\rho}_Q(t) \hat{L}_r^\dagger - \frac{1}{2} \left\{ \hat{L}_r^\dagger \hat{L}_r, \hat{\rho}_Q(t) \right\} \right). \qquad (3.4)$$

Here, the operators $\hat{L}_r = \hat{l}_r \otimes \hat{\mathbb{1}} + \hat{\mathbb{1}} \otimes \hat{l}_r$ describe decay of all relevant Rydberg states $|r\rangle$ in both atoms into the states $|g\rangle$, $|0\rangle$ and $|1\rangle$, whereby the $\hat{l}_r$ are given by

$$\hat{l}_r = \frac{7}{8} |g\rangle\langle r| + \frac{1}{16} |0\rangle\langle r| + \frac{1}{16} |1\rangle\langle r|. \qquad (7.11)$$

The decay rate γ_r is the inverse of the lifetime τ_r of Rydberg state $|r\rangle$. Corresponding values for the target Rydberg states in both settings are given in TAB. 8.1. For an experiment at room temperature ($\sim 300\,\mathrm{K}$) in setting S1, we find that Bell states are generated with a fidelity of better than 0.9999 at a gate time slightly below 60 ns. The results for optimized DRAG pulses are plotted in FIG. 7.7. Since lifetimes are shorter in setting S1, corresponding gate fidelities start to become limited by non-unitary errors at gate times
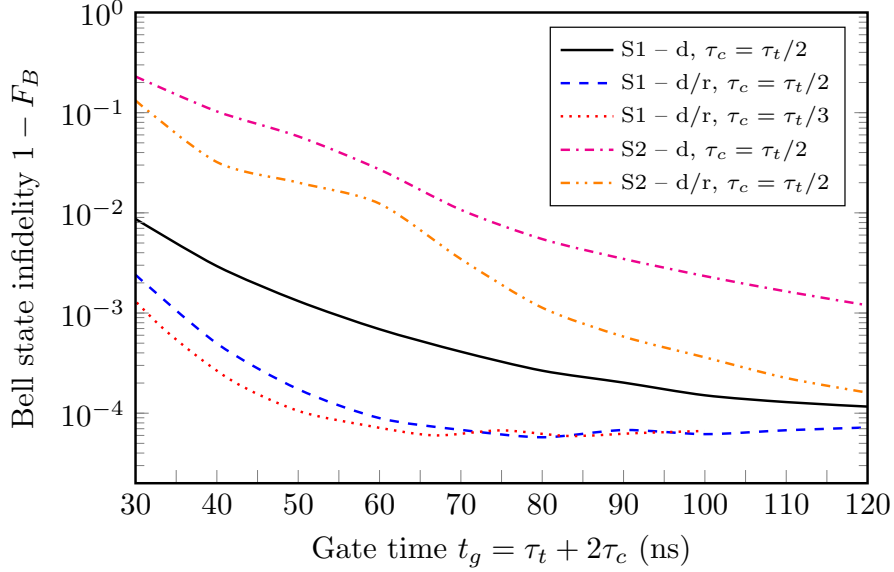
FIG. 7.7 – Bell state infidelity including decay out of all Rydberg levels for optimized DRAG controls in both settings S1 and S2. Phase errors and amplitude errors are accounted for by detuning (d) and rescaling (r) the analytically obtained DRAG sequences, as described above. Bell states are generated with a fidelity of 0.9999 at a total gate time of only 50 ns.

shorter than those where pulses in setting S2 suffer from limitation by dissipation. Overall, however, unitary errors are dominant, so that gates in setting S1 appear to be more promising than those in S2, despite shorter lifetimes. Since π pulses on the control atom do not require blockade effects, we may run them faster without losing performance. The dotted red curve in FIG. 7.7 confirms this observation: For $\tau_c = \tau_t/3$ we achieve slightly better results, yielding 10^{-4} errors at only 50 ns gate time. In a 4 K environment lifetimes will be on the order of a few milliseconds, allowing for performance very similar to that for the unitary analysis.

We have characterized the gate performance in terms of the Bell state fidelity. While the specific choice of fidelity (4.2) is the most widely used measure of gate performance, others have been proposed [230]. In particular the trace distance has been shown to be linearly sensitive to Rydberg gate phase errors that affect the fidelity only quadratically [218]. Using the rescaled (r) and detuned (d) DRAG gates that optimize the fidelity, we find that the trace distance error is an order of magnitude larger. As it is an open question as to which performance measure is most relevant for specific quantum computational tasks we have not studied the trace distance in more detail, although we anticipate that the trace distance error could also be reduced

with appropriate pulse design.

7.4   Conclusion

In conclusion we have presented DRAG pulses with pure x-quadrature control for Rydberg blockade gates that lead to a Bell state fidelity larger than 99.99% at gate times of only 50 ns. The pulses are designed based on an analytical method that could readily be extended to the level structure of other atoms. The results fully account for all dominant leakage channels as well as Rydberg decay in a room temperature environment. The 50 ns gate time is orders of magnitude faster than high-fidelity trapped ion gates, and about the same speed as state-of-the-art superconducting qubit gates, while the ratio of coherence time to gate time is orders of magnitude better.

Together with recent progress in high-fidelity single-qubit gates [86, 87] in neutral atom platforms, DRAG pulses establish neutral atom qubits with Rydberg blockade gates as a promising candidate for scalable quantum computation. Our result specifically applies to the case of one-photon Rydberg excitation. We leave extension to the more common case of two-photon excitation for future work. We also emphasize that the predicted gate fidelity assumes no technical errors and ground state laser cooling. Demonstrating real performance close to the theoretical level established here remains an outstanding challenge.

Chapter 8

Coherent Entanglement of Trapped Ions

In the previous chapter we showed how controls and parameters obtained via analytical derivation can be used to implement desired processes with high fidelity. Such approaches are typically only possible if the system's degree of complexity is manageable via analytical methods, such as accurate enough effective models. If analytic derivations are intractable, or if one intends to explore the full power of quantum optimal control, numerically assisted optimization algorithms as introduced in section 4.2 are the method of choice. In this chapter we will utilize the GOAT algorithm [131], which combines the benefits of analytic pulse parametrization and numerically assisted optimization, to study the generation of Greenberger-Horne-Zeilinger states ($|\text{GHZ}\rangle$) in a linear chain of trapped $^9\text{Be}^+$ ions.

Generation of entangled quantum states is key to applications in quantum information processing. When Cirac and Zoller first proposed linearly trapped ions as an architecture for quantum computing [76], they also showed how multi-qubit gates between trapped ions can be realized by coupling different ions through their vibrational modes which were introduced in section 2.2.2. A more elaborate way to generate entanglement is the Mølmer-Sørensen gate [77], which in contrast to the proposal by Cirac and Zoller does not require the ions to be completely cooled to their motional ground state. In both approaches, lasers provide the fundamental resource to achieve the necessary couplings. Both schemes coherently control the trapped ion system in order to generate entanglement deterministically. As this requires high-fidelity state preparation and sufficient reduction of decoherence errors, other ap-

---

This chapter is based on work done in collaboration with Shai Machnes, Giovanna Morigi and Frank Wilhelm-Mauch. In preparation.

proaches based on active feedback [231, 232] or dissipative state preparation [233–235] appear to be promising alternatives to bare unitary control: Feedback techniques on large scale will still require active error correction, and hence suffer from immense qubit overhead. Dissipative preparation schemes typically amount to constructing a Liouvillian such that the target state becomes the steady state of the driven master equation, and are hence also referred to as *quantum reservoir engineering*. As a consequence, quantum reservoir engineering protocols tend to be intrinsically robust with respect to many experimental noises, such as variability in initial conditions and control fluctuations. Such schemes operate on timescales of the system's dissipative processes, which, by design, are usually much longer than the timescale for unitary control. In contrast, relevant rates for state preparation via coherent coherent control are often only limited by the available power.

Dissipative state preparation of trapped $^9\mathrm{Be}^+$ ions achieved fidelities no better than 90% on timescales of a few hundred microseconds up to milliseconds [234, 236]. Recent work [237] applied optimal control theory to improve on these results by finding optimal parameter settings, thereby enhancing fidelities up to 98.7% in 6 ms operational time. Due to the exceedingly long time, however, dissipative preparation might be vulnerable to other processes in the system, such as dephasing and parameter drifts. Work based on coherent state preparation demonstrates the generation of maximally entangled states with infidelities of $8 \cdot 10^{-4}$ [238] and 10^{-3} [51] on timescales of $100\,\mu$s. The goal of this chapter is to better understand if there is a clear advantage for either the dissipative or coherent approach. To this end we shall apply the GOAT algorithm in order to find robust Raman laser envelopes that generate maximally entangled $|\mathrm{GHZ}\rangle$ states with infidelities comparable to previous protocols, but in significantly shorter times than is currently available. We then examine the resulting pulse robustness to realistic levels of control noise and initial state variability, allowing us to determine, in this instance, whether dissipative or coherent state preparation is advantageous.

8.1 The System Model

Commonly, dynamics of trapped ions are described by effective models that are based on adiabatic elimination [239, 240], the rotating wave approximation and a Lamb-Dicke approximation [60, 241]. The latter corresponds to an approximation which allows to significantly simplify coupling terms between ions and their vibrational modes by utilizing that the recoil energy of photons is smaller than a motional energy quantum. If sophisticated laser envelopes are applied, careful analysis of the validity of all approximations
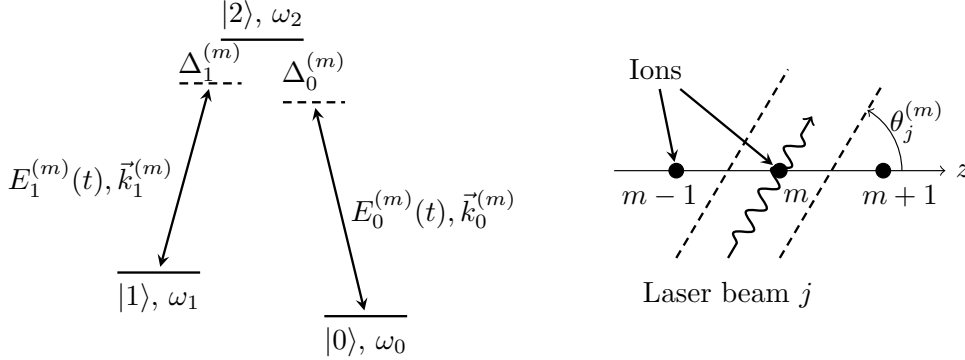
FIG. 8.1 – Each ion is modeled as a Λ-system where transitions between the computational states $|0\rangle$ and $|1\rangle$ are driven by Raman lasers with amplitudes $E_j(t)$ and wave vectors $|\vec{k}_j| = \omega_{L,j}/c$ (left). The ions are confined in a linear chain along the z-axis, whereby ion m is irradiated at an angle $\theta_j^{(m)}$ with laser $E_j^{(m)}(t)$. The width of the laser beams and the associated angles $\theta_j^{(m)}$ need to be chosen such that individual control of every ion is possible.

is required. For instance, effects as discussed in chapter 5 become relevant and cannot be captured by adiabatic elimination theory. Moreover, certain limits on the maximum control amplitudes need to be enforced in order for the approximations to hold. Therefore, our goal is to work in a model that is as generic as possible. This also has the advantage of alleviating experimental requirements which stem from more restrictive models, for instance the $\hat{\sigma}_z \hat{\sigma}_z$ interaction described in [235, 242]. We encode the computational states $\{|0\rangle, |1\rangle\}$ in the magnetic hyperfine manifold and use two respective Raman lasers per ion m with amplitude $E_j^{(m)}(t)$, as illustrated in FIG. 8.1, to drive transitions between the computational states via the *stratospheric* state $|2\rangle$. In the remainder of this chapter, subscript j labels which computational state couples to the stratospheric state and superscript (m) denotes the ion index. The free evolution Hamiltonian $\hat{H}_0$ of N ions and their associated N vibrational modes is given by

$$\hat{H}_0 = \sum_{m=1}^{N} \sum_{j=0}^{2} \hbar\omega_j |j\rangle\langle j|^{(m)} + \sum_{p=1}^{N} \hbar\omega_{z,p}\hat{a}_{z,p}^\dagger\hat{a}_{z,p}. \tag{8.1}$$

Here, as detailed in section 2.2.2, $\omega_{z,p}$ is the frequency of the p-th mode along the axis of the chain, described by the harmonic ladder operators $\hat{a}_{z,p}$ and $\hat{a}_{z,p}^\dagger$. Note that we assume strong binding of the ion chain so that relevant vibrational modes are restricted to those along the axis of the chain. Coupling terms, mediated by individual Raman lasers $E_j^{(m)}(t)$ with associated carrier

frequencies $\omega_{L,j}^{(m)} = c\,|\vec{k}_j^{(m)}|$, are modeled by the interaction Hamiltonian

$$\hat{H}_I = \hbar \sum_{m=1}^{N} \sum_{j=0}^{1} E_j^{(m)}(t) e^{-i\omega_{L,j}^{(m)}t} e^{i\vec{k}_j^{(m)}\cdot\vec{x}^{(m)}} e^{i\varphi_{L,j}^{(m)}} \,|2\rangle\langle j|^{(m)} + \text{h.c.} \tag{8.2}$$

The $\varphi_{L,j}^{(m)}$ are laser phases associated to the envelopes $E_j^{(m)}$. From the geometry illustrated on the right-hand side of FIG. 8.1 we deduce the identity

$$\begin{aligned}
\vec{k}_j^{(m)} \cdot \vec{x}^{(m)} &= \left|\vec{k}_j^{(m)}\right| z_0^{(m)} \cos\left(\theta_j^{(m)}\right) + \left|\vec{k}_j^{(m)}\right| q^{(m)}(t) \cos\left(\theta_j^{(m)}\right) \\
&= \tilde{\varphi}_j^{(m)} + \left|\vec{k}_j^{(m)}\right| q^{(m)}(t) \cos\left(\theta_j^{(m)}\right),
\end{aligned} \tag{8.3}$$

where $q^{(m)}(t)$ is the fluctuation of ion m around its equilibrium position $z_0^{(m)}$. We use identity (8.3), introduce an arbitrary phase $\phi_j^{(m)} \equiv \tilde{\varphi}_j^{(m)} + \varphi_{L,j}^{(m)}$ and quantize the ion motion following the theory in 2.2.2 to rewrite the interaction Hamiltonian in the form

$$\begin{aligned}
\hat{H}_I = \hbar \sum_{m=1}^{N} \sum_{j=0}^{1} & E_j^{(m)}(t) e^{-i\omega_{L,j}^{(m)}t} \\
& \times \exp\left(i\left[\phi_j^{(m)} + \eta_j^{(m)} \sum_{p=1}^{N} s_m^{(p)}\left(\hat{a}_{z,p}^\dagger e^{i\omega_{z,p}t} + \text{h.c.}\right)\right]\right) |2\rangle\langle j|^{(m)} + \text{h.c.}
\end{aligned} \tag{8.4}$$

In Hamiltonian (8.4) we introduced the common Lamb-Dicke parameter

$$\eta_j^{(m)} \equiv \sqrt{\frac{\hbar}{2M\omega_z}} |\vec{k}_j^{(m)}| \cos\left(\theta_j^{(m)}\right) \tag{8.5}$$

which typically is small enough to warrant an expansion of the exponent for $\eta_j^{(m)} \ll 1$, corresponding to the Lamb-Dicke approximation described above. The second line of equation (8.4) illustrates the major advantage of the Lamb-Dicke approximation: The associated expansion avoids to exponentiate the infinite-dimensional mode operators and hence allows for further analytical simplification. However, we intentionally refrain from using such an approximation.

A More Convenient Frame

The exact parameters and frequencies that describe our system are given in TAB. 8.1. With reference to section 4.3 we note that the energy separation of the stratospheric state $|2\rangle$ to the computational subspace is about six

orders of magnitude larger than the splitting of both computational states, inevitably hampering computations of the eigendecomposition needed for PWC propagation since it is very error-prone for ill-conditioned matrices (for instance matrices with dramatic differences in scales). Said difference in scales also poses problems to other ODE integration methods: The computational time to obtain reliable results will be unacceptable for OCT purposes since the step size of the ODE solver needs to be extremely small in order to accurately follow the high-frequency components induced by the high energy of state $|2\rangle$.

In order to alleviate numerical propagation we transform the Hamiltonian to a frame where the vibrational modes are co-rotating at their respective frequencies. Additionally, we rotate each ion subspace such that the oscillatory terms $e^{i\omega_{L,j}^{(m)}t}$ in Hamiltonian (8.4) vanish and the time-dependence is solely encoded in the laser amplitudes $E_j^{(m)}(t)$. The associated transformation that we apply along the lines of equation (3.3) reads

$$\hat{V}_{\text{rot}} = \left[\bigotimes_{m=1}^{N} e^{-i\hat{\bar{H}}^{(m)}t/\hbar} \right] \otimes \left[\bigotimes_{p=1}^{N} e^{i\omega_{z,p}t\hat{a}_{z,p}^{\dagger}\hat{a}_{z,p}} \right], \qquad (8.6)$$

where we introduce the carrier detunings such that $\omega_{L,j}^{(m)} \equiv \omega_2 - \Delta_j^{(m)} - \omega_j$ and have used the definition

$$\hat{\bar{H}}^{(m)} \equiv \hbar \operatorname{diag}\left(\omega_0 + \Delta_0^{(m)}, \omega_1 + \Delta_1^{(m)}, \omega_2 \right). \qquad (8.7)$$

Note that the transformation of the vibrational modes in equation (8.6) is different from the conventional interaction picture transformation where one usually moves to a counter-rotating frame in order to cancel the contribution of motional states to the drift Hamiltonian. Instead, we move to a frame in which the subspace of each motional mode is co-rotating with its respective frequency. The identity

$$e^{-i\omega t\hat{a}^{\dagger}\hat{a}}\exp\left(c_0 \left[e^{i\omega t}\hat{a}^{\dagger} + e^{-i\omega t}\hat{a} \right] \right) e^{-i\omega t\hat{a}^{\dagger}\hat{a}} = \exp\left(c_0 \left[\hat{a}^{\dagger} + \hat{a} \right] \right) \qquad (8.8)$$

with arbitrary $c_0 \in \mathbb{C}$ is useful to understand the effect of transformation (8.6). Eventually, we cancel the $e^{\pm i\omega_{z,p}t}$ terms in Hamiltonian (8.4), but are effectively left with motional states with twice the frequency as in the lab frame.

The full rotating frame Hamiltonian after applying transformation (8.6)

Parameter	Value	Parameter	Value
Z	1	e (C)	$1.6021766208 \cdot 10^{-19}$
M (u)	9u	u (kg)	$1.660539040 \cdot 10^{-27}$
ϵ_0 (As/Vm)	$8.854187817 \cdot 10^{-12}$	$\hbar$ (Js)	$1.054571800 \cdot 10^{-34}$
$\omega_z/2\pi$ (MHz) [60]	~ 5	l (μm)	5.36
$\omega_0/2\pi$ (GHz)	0	$\omega_1/2\pi$ (GHz)	1.207496
$\omega_2/2\pi$ (GHz)	957804.5877	$\lambda_{|0\rangle\leftrightarrow|2\rangle}$ (nm) [238]	313
c (m/s)	$2.99792458 \cdot 10^8$		

Table 8.1 – Numerical parameters used for our simulations. Spectral information about the ^{9}Be$^+$ ions is taken from [238]. See also section 2.2 for more details.

reads

$$
\hat{H}_{\text{rot}} = 2 \sum_{p=1}^{N_p} \hbar \omega_{z,p} \hat{a}_{z,p}^\dagger \hat{a}_{z,p} + \hbar \sum_{m=1}^{N} \sum_{j=0}^{1} \left[\left(-\Delta_j^{(m)} \right) |j\rangle\langle j|^{(m)} \right.
$$
$$
\left. + \left\{ E_j^{(m)}(t) \cos\left(\phi_j^{(m)} + \eta_j^{(m)} \sum_{p=1}^{N} s_m^{(p)} \left(\hat{a}_{z,p} + \hat{a}_{z,p}^\dagger \right) \right) |2\rangle\langle j|^{(m)} + \text{h.c.} \right\} \right]
$$
$$
(8.9)
$$

which is indeed free of any rapid oscillations on the order of ω_2 (and $\omega_{L,j}^{(m)}$). Moreover, the control fields $E_j^{(m)}(t)$ are its only time-dependent components. We stress that Hamiltonian (8.9) does *not* involve any type of rotating wave or other approximation. As we refrain from applying a Lamb-Dicke approximation, we will compute the cosine term in Hamiltonian (8.9) numerically exact. Hereto, we need to truncate the Hilbert space to finite dimensions, which we will detail below.

8.2   General OCT Procedure

In this section we will describe further details about the optimization procedure, for which we use an advanced implementation of the GOAT algorithm (c.f. section 4.2.2) in MATLAB. We will first focus on implications of the truncated Hilbert space and then provide a proper definition of the target goal function, as well as an outline of the control parametrizations we use. Regarding propagation, a PWC propagator with $\mathcal{O}\left(10^4\right)$ segments is the preferred method of choice.

8.2.1 Hilbert Space Cutoff

In order to numerically propagate Hamiltonian (8.9) we need to truncate the infinite-dimensional Hilbert space associated to the vibrational modes of the ion chain. We denote the basis states of the full system $|i_1 i_2 \cdots i_N m_1 m_2 \cdots m_N\rangle$ where $i_k \in \{0, 1, 2\}$ labels the internal state of ion k, and the vibrational state of mode k is given by $m_k \leq M_k$. Here, M_k denotes the highest level of vibrational mode k after which the respective Hilbert space is truncated. To ensure that our results remain valid in the real system without cutoff, we need to ensure that population in all highest vibrational levels $|M_k\rangle$ with $k = 1, \ldots N$ is negligible over the entire propagation time. This guarantees that higher modes have no substantial contribution to the dynamics, since the ladder operators $\hat{a}_{z,p}$ and $\hat{a}_{z,p}^\dagger$ only couple adjacent levels, and the Hilbert space cutoff does not impact our results. In order to enforce this constraint on the populations in our optimization routine, we introduce a penalty term

$$Q(\vec{x}) = \log_{10}\left(\frac{1}{t_g} \int\limits_0^{t_g} \sum_{l=1}^{N_\Psi} \langle \Psi_l(\vec{x}, t) | \hat{\mathbb{P}}_p | \Psi_l(\vec{x}, t) \rangle \, \mathrm{d}t \right) \qquad (8.10)$$

where $\hat{\mathbb{P}}_p = \sum_n |\Phi_n\rangle\langle\Phi_n|$ describes the projector onto all penalized states, i.e. any state where at least one mode is excited to its highest level, and $\{|\Psi_l(\vec{x}, t)\rangle\}$ is the set of all propagated states at times $t \in [0, t_g]$ depending on the parameters $\vec{x}$. Hence, Q essentially measures the total amount of intermediate excitation to undesired states, whereby $Q \to -\infty$ if there is no occupation of the forbidden subspace and $Q = \log_{10}(N_\Psi)$ if the $\{|\Psi_l\rangle\}$ lie inside said subspace for the entire duration. In addition to penalizing the highest vibrational modes we will also need to include the stratospheric state $|2\rangle$ into the penalty term, as will be discussed below.

8.2.2 Multi-Goal Optimization

With focus on the situation relevant for this chapter, we need to optimize the overlap between states along the lines of equation (4.5) – where we straightforwardly replace the gates by target and propagated state vectors – and take into account the additional penalty (8.10). That is, we introduce a combined goal function $G(\vec{x})$ which depends on both g and Q. Usually, if additional constraints in form of penalty terms are included in the optimization, the corresponding terms appear as additional summands in the final goal function [120] so that we would have $G(\vec{x}) = g(\vec{x}) + Q(\vec{x})$. However, a downside of this choice of G is that the optimization might only care for either g or Q initially. For difficult optimization tasks, once it converges in the direction of any of
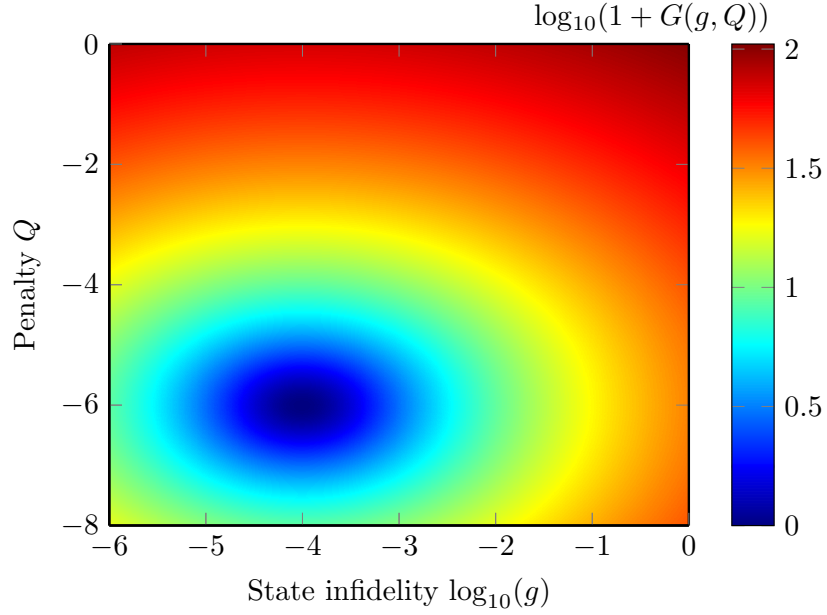
FIG. 8.2 – Landscape of the combined goal function (8.11) in the (g, Q) space for $c_s = c_d = 1$ and $e_s = e_d = 2$. The target values are $Q_0 = -6$ and $g_0 = -4$, and the point $(-4, -6)$ corresponds to the unique global minimum of the multi-goal optimization.

these quantities, this is often accompanied with failure of the algorithm since it is effectively trapped in the optimization landscape.

Combined Goal Function

Our approach to circumvent this issue is a careful construction of the combined goal function G. The optimization will terminate once both g and Q fall below their target thresholds g_0 and Q_0, respectively. To avoid that either g or Q undercut these values significantly (which ultimately reduces the risk of local traps) we found the goal function parametrization

$$G(\vec{x}) = c_s \left(g_{\text{eff}}(\vec{x}) + Q_{\text{eff}}(\vec{x})\right)^{e_s} + c_d \left(g_{\text{eff}}(\vec{x}) - Q_{\text{eff}}(\vec{x})\right)^{e_d} \tag{8.11}$$

to be most efficient. The effective values of g and Q are given by $g_{\text{eff}} \equiv g - g_0$ and $Q_{\text{eff}} \equiv Q - Q_0$, respectively. The constants c_s, c_d, e_s and e_d are free parameters. However, we find the choice $c_s = c_d = 1$ and $e_s = e_d = 2$ to work best for our purposes. FIG. 8.2 illustrates the optimization landscape as a function of g and Q, indicating that $G(g, Q)$ exhibits a unique global minimum at (g_0, Q_0). The advantage over other choices of G is that if, for instance, q falls below its target value, the gradients will actively prevent

further reduction of Q, so that the risk of local trapping in the direction of either g or Q is minimized.

Gradient Computation

In order for the GOAT algorithm to be feasible, efficient computation of the gradient $\partial_{\vec{x}} G(\vec{x})$ is required. The GOAT equations of motion (4.7) now need to be extended by the gradients of Q. For simplicity, we restrict our analysis to the quantity $q = 10^Q$. Gradients of Q are obtained via direct application of the chain rule. Particularly, we know

$$\partial_t q = \frac{1}{t_g} \sum_l \langle \Psi_l | \hat{\mathbb{P}}_p | \Psi_l \rangle \,, \tag{8.12a}$$

$$\partial_t \partial_{\vec{x}} q = \frac{1}{t_g} \sum_l (\partial_{\vec{x}} |\Psi_l\rangle)^\dagger \hat{\mathbb{P}}_p |\Psi_l\rangle + \text{h.c.} \tag{8.12b}$$

We are hence left with a system of coupled equations of motion for the propagated states and their gradients, as well as the penalty terms (8.12). Initial conditions are given by $q(\vec{x}, 0) = 0$ and $\partial_{\vec{x}} q(\vec{x}, 0) = \vec{0}$. The reader is referred to Appendix 8.A for more details on efficient penalty computation for the particular case of PWC propagation, which is crucial to make the implementation of the GOAT algorithm feasible.

8.2.3 Control Parametrization

Generally, the GOAT algorithm allows to utilize any analytical pulse parametrization – provided its gradients exist. In our case, we will use two different control parametrizations: (i) Superpositions of time-window functions based on error functions and (ii) piecewise constant (PWC) controls, where the full time window is divided into N_τ slices of width Δ_τ, whereby the controls are considered constant within each of these slices.

Both approaches are conceptually quite different: While (without additional constraints) PWC controls tend to appear noisy, they allow to explore the limits of the control task since they generally grant most freedom in pulse design. Contrarily, analytic parametrizations, for instance in terms of Fourier components, Gaussians or error functions, can lead to simple and smooth control shapes. The choice of the specific analytical parametrization depends very much on the quantum control problem. We chose a superposition of error functions since their spectrum is well located at distinct frequencies, which alleviates suppression of unwanted excitations in a dense spectrum. This is attributed to the fact that the envelopes $E_j^{(m)}$ are multiplied with their respective carrier signal and hence, if we chose Fourier modes, we would generate
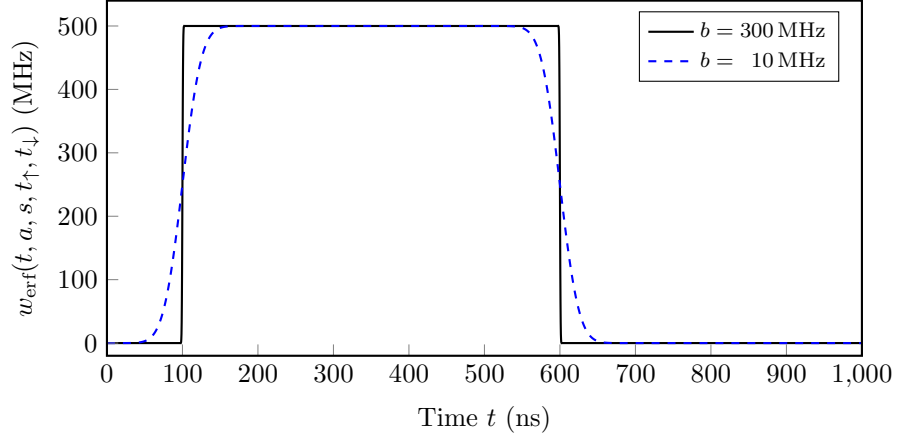
FIG. 8.3 – Window function based on error functions according to equation (8.13). Parameters chosen for the illustration are $a = 500\,\mathrm{MHz}$, $A = 1\,\mathrm{GHz}$, $t_\uparrow = 100\,\mathrm{ns}$ and $t_\downarrow = 600\,\mathrm{ns}$. Decreasing the slope s, here achieved by lowering b while keeping A constant, softens the edges of the window when ramping up/down.

beat frequencies – effectively exciting multiple frequencies other than those that are actually required. FIG. 8.3 illustrates a single error function window

$$w_{\mathrm{erf}}(t, a, s, t_\uparrow, t_\downarrow) = \frac{a}{4} \left(1 - \mathrm{Erf}\left(\frac{\sqrt{\pi}}{a} s(t - t_\downarrow) \right) \right) \left(1 + \mathrm{Erf}\left(\frac{\sqrt{\pi}}{a} s(t - t_\uparrow) \right) \right), \tag{8.13}$$

with amplitude a, slope s and ramp up (down) time $t_\uparrow$ ($t_\downarrow$). $\mathrm{Erf}(x)$ is the Gauss error function. In our optimizations we assume a control bandwidth of $b = 300\,\mathrm{MHz}$ and fix the slope per window to $s = A/(1/b)$ where A is the maximum limit on the amplitude $a \in [-A, A]$. Note that pulse parameters are bounded in order to not exceed feasible limits of pulse shaping capabilities [131]. We parametrize each laser envelope $E_j^{(m)}$ in terms of a superposition of $N_j^{(m)}$ such error function windows whereby amplitude, ramp up and ramp down time of each of these are individually optimized parameters. Hence, the total number of parameters characterizing the laser envelopes is given by $N_{p,c} = 3 \sum_{j,m} N_j^{(m)}$.

8.3   Generation of Entangled States

In this section we will now study the generation of the maximally entangled state $|\mathrm{GHZ}\rangle = (|00aa\rangle + |11aa\rangle)/\sqrt{2}$. In this notation the vibrational mode

levels are labeled in alphabetical order from a onward. As introduced above, we focus on a linear chain of two $^9\text{Be}^+$ ions with a trap frequency $\omega_z/2\pi \sim 5\,\text{MHz}$. In order to design smooth pulses the controls are parametrized in terms of error function windows (8.13): Each Raman amplitude $E_j^{(m)}(t)$ consists of $N_j^{(m)} = 7$ individually optimized window functions, so that the total number of parameters we optimize is $N_{p,c} = 7 \times 2 \times 2 \times 3 = 84$ (two ions, two beams per ion, three parameters per error function window). For now, we assume that the system is initially cooled to the ground state $|00aa\rangle$. This assumption will be revisited later. FIG. 8.6 depicts the performance of optimized Erf controls, as well as their robustness against noise (c.f. section 8.3.2) for operation times t_g of a few hundred nanoseconds (compared to $\mathcal{O}\left(100\mu s\right)$ in [51, 238]). We achieve infidelities of 10^{-4} for operation times around $500\,\text{ns}$. Examples of optimized controls for $t_g = 500\,\text{ns}$ are illustrated in FIG. 8.4. To generate pulses that smoothly start and end in zero, we apply an additional filter on top of the superposition of window functions and compute the final gradient with respect to the parameters by a straightforward application of the chain rule.

Note that, in addition to the discussion in section 8.2.1, the penalty cost function Q we use in our optimizations also inhibits population of the stratospheric state $|2\rangle$. Since it is highly dissipative with a decay constant $\tau_2 \sim 10\,\text{ns}$, it should remain sufficiently unpopulated at all times. As a consequence, we penalize a fraction of $1 - (2/3)^N \prod_k (M_k - 1)/M_k$ of the total Hilbert space, where N is the number of ions and M_k the number of energy levels per vibrational mode. That is, overall, the factor $(2/3)^N$ corresponds to avoiding excitation of any ion m to its respective stratospheric state $|2\rangle^{(m)}$, while $\prod_k (M_k - 1)/M_k$ is associated to suppressing population of vibrational levels at which the Hilbert space is truncated. In our simulations, in order to retain feasible computational times, we use $M_k = 4$ so that for two ions 75% of the total Hilbert space contribute to the penalty cost in terms of the projector $\hat{\mathbb{P}}_p$. FIG. 8.6 demonstrates that optimized Erf controls achieve penalties slightly below 10^{-2}. A closer analysis shows that the final Q is determined largely by population of the stratospheric state; contributions due to the Hilbert space cutoff are negligible – substantiating the numerical accuracy of our model compared to the full, untruncated version.

8.3.1   Effect of Spontaneous Emission

Based on the above analysis, we need to consider implications of intermediate population in the stratospheric state. We estimate the error due to spontaneous emission out of state $|2\rangle$ by means of the achieved penalties: Hereto,
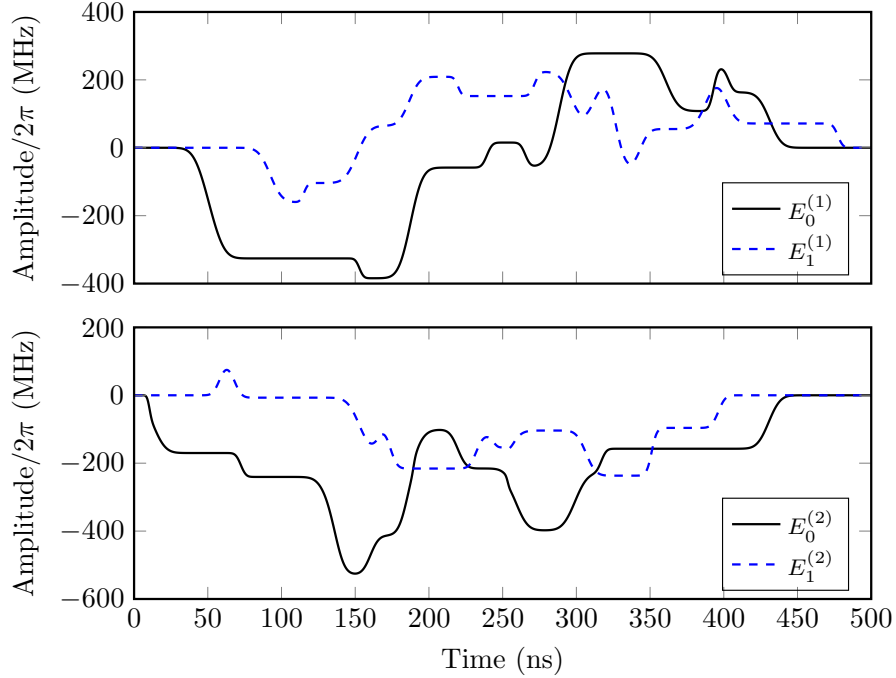
FIG. 8.4 – Optimized Erf-window based control pulses for an operation time of 500ns. The pulses achieve infidelities of $\sim 10^{-4}$ and a penalty $\sim 10^{-2}$. Every Raman laser $E_j^{(m)}$ is parametrized in terms of $N_j^{(m)} = 7$ individual Erf components, yielding a total parameter count of 84 that are optimized.

we focus on PWC propagation with N_τ time slices of equal length and a corresponding slice width $\Delta_\tau = t_g/N_\tau$. At each time step we lose population p_2 to state $|2\rangle$, followed by a dissipative process over time Δ_τ. According to this model, the overall coherent population p_c after N_τ time steps is approximately given by

$$p_c = \left((1 - p_2) + p_2 e^{-\Delta_\tau/\tau_2}\right)^{N_\tau} . \tag{8.14}$$

While this estimate does of course not account for all errors it should provide feasible bounds if $\Delta_\tau \ll \tau$. Unfortunately, the penalties we find in FIG. 8.6 imply spontaneous emission errors of about 14.3% – rendering the quoted infidelities unreliable. Nevertheless, we find that a penalty $Q = 10^{-4}$ already translates into spontaneous emission errors of only $5 \cdot 10^{-3}$. Thus, we expect that by increasing the laser detunings $\Delta_j^{(m)}$ by about one to two orders of magnitude, and a corresponding enhancement of operation time t_g, it should be feasible to achieve penalties of 10^{-4} or below, thereby obtaining reliable infidelities comparable to those reported in literature – but at much shorter times.
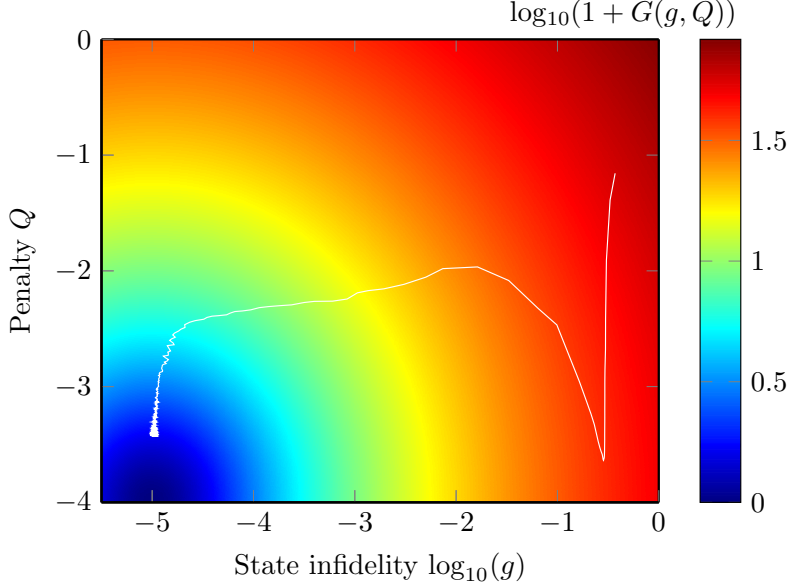
FIG. 8.5 – Trajectory of the multi-goal optimization in the (g, Q) space for piecewise constant control parametrizations with a pulse duration of $500\,\text{ns}$. The Raman lasers are detuned from resonance by $\Delta_j^{(m)} \sim 13\omega_1$.

In order to explore possible intrinsic limitations in our model, we also perform optimizations with PWC controls in a system that is otherwise identical to the one we used for error function based optimizations. To be less restrictive we set the target infidelity to $g_0 = 10^{-5}$. With PWC controls operating for $t_g = 500\,\text{ns}$ and a total number of $N_{p,c} = 200$ parameters per control (the amplitude of each slice counts as a parameter) we are able to produce pulses that generate state infidelities $g = 10^{-5}$ while maintaining a penalty of $Q = 10^{-3.6}$. Using our estimate (8.14) this translates into a spontaneous emission error of 1.22%, which corresponds to a realistic fidelity of 98.78% – almost exactly matching the best fidelity reported in [237]. The associated trajectory of the multi-goal optimization is illustrated in FIG. 8.5.

8.3.2 Robustness of the Solutions

In order to be feasible for practical implementations, control pulses should be robust against the most relevant noise sources. As discussed above, solutions found via quantum reservoir engineering tend to feature the desired robustness. We therefore benchmark our results against two relevant noise sources: Fluctuations of the laser amplitude and variations in the initial state. Fluctuations in the control amplitudes are modeled by an Ornstein-Uhlenbeck

process [243, 244], which is a stochastic process subject to the stochastic differential equation

$$\mathrm{d}x_t = \beta(\mu - x_t)\mathrm{d}t + \sigma\,\mathrm{d}W_t. \tag{8.15}$$

Here, x_t denotes the value of a quantity affected by noise – for instance position of a particle – at time t, μ is the equilibrium value, σ corresponds to the amount of fluctuation, β gives the rate with which the variable reverts back to its mean and W_t is the Wiener process. Realistic amplitude variations are on the order of 1%, which we simulate by the parameters $\beta = 0.1$, $\mu = 1$, $\sigma = 0.002$ and an initial value of $x_0 = 1$. As illustrated in FIG. 8.6a the controls based on error functions are pretty robust against variations of the $E_j^{(m)}(t)$, substantiated by degradations of the infidelity by about one order of magnitude. To simulate variable initial conditions we initialize the system in a state that has 99% overlap with the ideal initial state $|00aa\rangle$, while the remaining 1% is distributed equally among the states $|00ab\rangle$, $|00ba\rangle$ and $|00bb\rangle$. In that case, as depicted in FIG. 8.6b, we achieve infidelities of about $10^{-2.3}$ which is slightly worse compared to noise in the laser amplitude, but still on a tolerable level – comparing to other reported fidelities in literature. We emphasize that the analyzed timescales are on the order of a few hundred nanoseconds, hence orders of magnitude below current proposals.

8.4 Discussion

8.4.1 Conclusion

We derived a Hamiltonian that is far more general than conventional effective models which are based on adiabatic elimination, as well as rotating wave and Lamb-Dicke approximations. This allowed us to explore the limits of entanglement generation via unitary processes in terms of control capabilities via quantum optimal control, which, in conventional models, is only possible to a limited extent due to the restrictions imposed by aforesaid approximations. In order to make use of the state-of-the-art GOAT algorithm for our analysis, we developed an efficient method to compute the gradients of penalty cost functions to suppress population of harmful states.

In summary, we have shown that coherent generation of $|GHZ\rangle$ states with realistic fidelities of about 99% in a linear chain of trapped ion is possible using piecewise constant control parametrizations on a timescale of a few hundred nanoseconds – orders of magnitude faster than conventional proposals, while achieving fidelities comparable to those of state-of-the-art schemes based on dissipative state preparation. The optimized piecewise constant pulse shapes
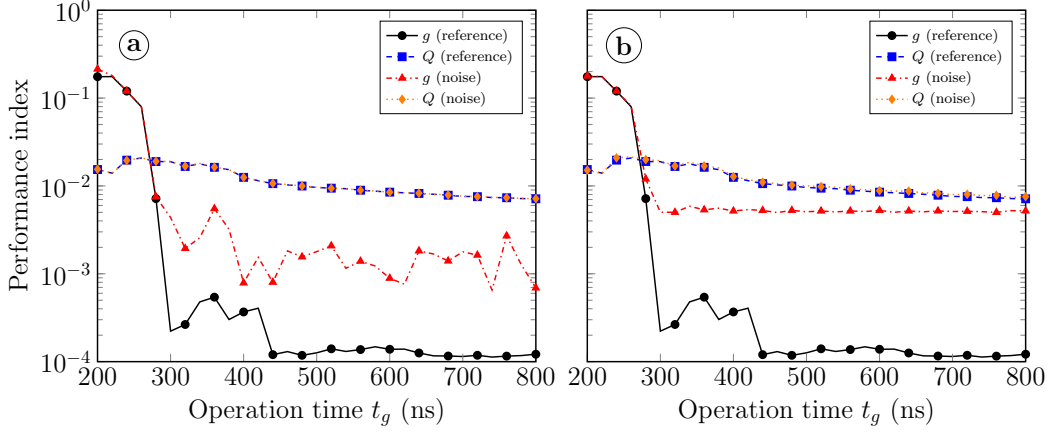
FIG. 8.6 – Infidelity g and penalty Q for preparation of $(|00aa\rangle + |11aa\rangle)/\sqrt{2}$ from initial state $|00aa\rangle$ as a function of operation time with $\omega_z/2\pi = 10\text{MHz}$ and $\Delta_j^{(m)} \approx 2\omega_1$. Each Raman laser amplitude is composed of $N_j^{(m)} = 7$ individual Erf components (8.13). Robustness is analyzed with respect to laser amplitude noise, modeled by an Ornstein-Uhlenbeck process (8.15) with variation of up to 1.5% (a) and with regards to residual phonons, i.e. variable initial condition (b). The "reference" data corresponds to noise-free dynamics. For realistic laser amplitude noise, infidelities are lowered from 10^{-4} to 10^{-3}. In case of variable initial conditions we find the pulses to be less robust. Yet, achieved infidelities of about $10^{-2.3}$ are still on a tolerable level. Saturation of g at about 10^{-4} is due to our choice of g_0 which prevents further, undesired improvement of g.

feature quick and rapid amplitude changes which render them impractical for direct experimental implementation. Nevertheless, they provide important theoretical information about fundamental limits of entanglement capabilities in our model. We also studied the limits of quantum optimal control in the sub-microsecond regime in terms of smooth controls based on error function windows. In that case, we were unable to find results that sufficiently suppress population inside the highly dissipative stratospheric states, so that realistic estimates for the fidelities are no higher than 85%. We found the smooth waveforms to be robust against two relevant noise sources: Amplitude fluctuations and variable initial conditions. Neglecting spontaneous emission errors, we were able to achieve errors as low as 10^{-4}, which is increased to 10^{-3} and $10^{-2.3}$ by amplitude and preparation noise, respectively.

8.4.2   Outlook

We expect that it is feasible to improve the penalty cost by two orders of magnitude (and, hence, enhance realistic entanglement fidelities accordingly) by increasing the laser detunings likewise, accompanied with a respective increase of operation times. This statement holds for both smooth controls and piecewise constant parametrizations. Eventually, this would still correspond to timescales at least one order of magnitude faster than the best current proposals (referring to both unitary and dissipative preparation schemes) while achieving preparation errors of only 0.1% or better, even under realistic considerations of noise. We anticipate that the results of our robustness analysis will also hold for longer timescales, since the functional shape of the controls will remain similar. Our MATLAB implementation of the GOAT algorithm has already been extended to support gradient-assisted optimization of laser detunings, phases and angles along with Raman laser envelopes. As such, future research can directly connect to the methods and results presented in this chapter, with the expectation of achieving significant improvements both in infidelities and penalties. Ultimately, this will allow to better understand if there is a clear preference for either unitary or dissipative entanglement schemes.

Appendix

8.A Propagation of Penalties

In order to perform quantum OCT using the GOAT algorithm with an additional penalty cost Q to suppress population of certain states, we need to simultaneously solve the underlying equations of motions. We focus on a single propagated state $|\Psi(t)\rangle$, subject to the Hamiltonian $\hat{H}(\vec{x}, t)$ where $\vec{x}$ are some controllable parameters. The definition of the penalty term is given in equation (8.10). In this section, we will drop the factor $1/t_g$ from the definition of Q for clarity and consider the gradients of $q = 10^Q$ instead. We combine the regular GOAT equations of motion (4.7) and those for the penalty (8.12) to the set ($\hbar \equiv 1$)

$$\partial_t |\Psi\rangle = -i\hat{H}|\Psi\rangle, \tag{8.16a}$$

$$\partial_t \partial_{\vec{x}} |\Psi\rangle = -i\left((\partial_{\vec{x}}\hat{H})|\Psi\rangle + \hat{H}\partial_{\vec{x}}|\Psi\rangle\right), \tag{8.16b}$$

$$\partial_t q = \langle\Psi|\hat{\mathbb{P}}_p|\Psi\rangle, \tag{8.16c}$$

$$\partial_t \partial_{\vec{x}} q = (\partial_{\vec{x}}\langle\Psi|)\,\hat{\mathbb{P}}_p|\Psi\rangle + \text{h.c.}, \tag{8.16d}$$

of coupled ordinary differential equations that need to be solved efficiently in order for the GOAT algorithm to be feasible. We note that $\partial_t(\langle\Psi|) = (\partial_t|\Psi\rangle)^\dagger$ and $\partial_{\vec{x}}(\langle\Psi|) = (\partial_{\vec{x}}|\Psi\rangle)^\dagger$.

8.A.1 PWC Propagation

The PWC assumption actually consists of two separate assumptions: First, we approximate $H(\vec{x}, t)$ as constant within each time slice, and in addition we assume the controls to be PWC as well. We choose a notation where slice τ starts at $t_{\tau-1}$ and ends at t_τ with a duration of Δ_τ. Without loss of generality we pick the full time interval such that $t_{\tau=0} = 0$ and $t_{\tau=N_T} = t_g$. Limiting ourselves to a single control field, to keep notation simple, we replace the general $\vec{x}$ with a time index x_τ. We can now attempt to solve

the above equations of motion (8.16): Expressions of $|\Psi_\tau\rangle$ and q_τ, as well as their derivatives at t_τ, in terms of $|\Psi_{\tau-1}\rangle$, $q_{\tau-1}$ and their derivatives at time $t_{\tau-1}$ constitute a proper solution to the dynamics. The solution to equation (8.16a) is straightforwardly given by

$$|\Psi_\tau\rangle = \hat{U}_\tau |\Psi_{\tau-1}\rangle , \tag{8.17}$$

$$\hat{U}_\tau = \exp\left(-i\Delta_\tau \hat{H}_\tau\right) . \tag{8.18}$$

For the second equation of motion (8.16b), we need to look at a specific component of $\vec{x}$: The control amplitude x_σ at time slice σ. If $\tau < \sigma$ then we have not yet arrived at slice σ and the respective derivative is zero. If $\tau = \sigma$, then $|\Psi_{\tau-1}\rangle$ is independent of x_σ but $\hat{U}_\sigma$ is not, and we have $|\Psi_\tau\rangle = \hat{U}_\sigma |\Psi_{\tau-1}\rangle$. Lastly, if $\tau > \sigma$ then $\hat{U}_\tau$ is independent of x_σ but $|\Psi_{\tau-1}\rangle$ is not. Hence,

$$\partial_{x_\sigma} |\Psi_\tau\rangle = \begin{cases} 0 & , \tau < \sigma \\ \left(\partial_\sigma \hat{U}_\sigma\right) |\Psi_{\tau-1}\rangle & , \tau = \sigma \\ \hat{U}_\tau \partial_{x_\sigma} |\Psi_{\tau-1}\rangle & , \tau > \sigma. \end{cases} \tag{8.19}$$

For the q equation of motion (8.16c) we make an additional assumption: We assume the value of $|\Psi\rangle$ is fixed for the entire slice, and is equal to $|\Psi_\tau\rangle$. This renders the solution of $\partial_t q = \langle\Psi|\hat{\mathbb{P}}_p|\Psi\rangle$ trivial:

$$q_\tau = \Delta_\tau \langle\Psi_\tau|\hat{\mathbb{P}}_p|\Psi_\tau\rangle + q_{\tau-1} \tag{8.20}$$

Solving the remaining equation of motion (8.16d) follows a logic similar to the one we used for $\partial_{x_\sigma} |\Psi_\tau\rangle$, and derives directly from the derivative of rule (8.20) with respect to x_σ, recalling that $q_\tau = \Delta_\tau \langle\Psi_{\tau-1}\hat{U}_\tau^\dagger|\hat{\mathbb{P}}_p|\hat{U}_\tau\Psi_{\tau-1}\rangle + q_{\tau-1}$, and that only $\hat{U}_\sigma$, $|\Psi_{\tau\geq\sigma}\rangle$ as well as $q_{\tau\geq\sigma}$ depend on x_σ:

$$\partial_{x_\sigma} q_\tau = \begin{cases} 0 & , \tau < \sigma \\ \Delta_\tau \left((\partial_{x_\sigma} |\Psi_\tau\rangle)^\dagger \hat{\mathbb{P}}_p |\Psi_\tau\rangle + \text{h.c.}\right) & , \tau = \sigma \\ \Delta_\tau \left((\partial_{x_\sigma} |\Psi_\tau\rangle)^\dagger \hat{\mathbb{P}}_p |\Psi_\tau\rangle + \text{h.c.}\right) + \partial_{x_\sigma} q_{\tau-1} & , \tau > \sigma. \end{cases} \tag{8.21}$$

8.A.2 Update Algorithm

We summarize all assumptions we make in order to perform the (gradient) propagation with a PWC integration formalism:

- The time interval $[0, t_g]$ is divided into N_τ slices. Slice τ starts at $t_{\tau-1}$ and ends at t_τ, duration Δ_τ. That is, $t_{\tau=0} = 0$ and $t_{\tau=N_\tau} = t_g$. We shall also use σ to enumerate time slices.

- There is a single control Hamiltonian. Extension to multiple controls follows naturally.

- $\hat{H}(\vec{x}, t)$ can be approximated as a constant operator $\hat{H}_\tau$ within each slice. For accuracy considerations, it is recommended (but not required) to sample the continuous control fields at the middle of each slice.

- The controls $\vec{x}$ are PWC, i.e. x_τ is the amplitude of the control Hamiltonian at slice τ. Therefore, $\hat{H}_\tau = \hat{H}_0 + x_\tau \hat{H}_c$.

- For the purposes of computing the penalty q, the value of $|\Psi\rangle$ is considered constant for the entire slice and is equal to $|\Psi_\tau\rangle$.

- We have a black box [118] to compute $\partial_{x_\tau} \exp\left(-i\Delta_\tau \left(\hat{H}_0 + x_\tau \hat{H}_c\right)\right)$

In order to propagate state and penalty, we require knowledge about the initial state $|\Psi_0\rangle$ and the value of the control field at all time slices x_τ for all $\tau = 1, \ldots, N_\tau$. The initial conditions for the propagation are $\partial_{x_\tau} |\Psi_0\rangle = 0$, $q_0 = 0$, $\partial_{x_\tau} q_0 = 0$ for all τ. The actual propagation is a loop on $\tau = 1 \ldots N_\tau$ with essentially five steps per iteration:

1. Compute Hamiltonian at slice τ, $\hat{H}_\tau = \hat{H}_0 + x_\tau \hat{H}_c$

2. Compute the associated propagator, $\hat{U}_\tau = \exp(-i\Delta_\tau H_\tau)$

3. Propagate the state, $|\Psi_\tau\rangle = \hat{U}_\tau |\Psi_{\tau-1}\rangle$

4. Integrate the penalty, $q_\tau = \Delta_\tau \langle\Psi_\tau|\hat{\mathbb{P}}_p|\Psi_\tau\rangle + q_{\tau-1}$

5. For each control parameter x_σ, i.e. for each gradient component, compute

$$\text{(a)} \quad \partial_{x_\sigma} |\Psi_\tau\rangle = \begin{cases} 0 & , \tau < \sigma \\ \left(\partial_\sigma \hat{U}_\sigma\right) |\Psi_{\tau-1}\rangle & , \tau = \sigma \\ \hat{U}_\tau \left(\partial_{x_\sigma} |\Psi_{\tau-1}\rangle\right) & , \tau > \sigma \end{cases}$$

$$\text{(b)} \quad \partial_{x_\sigma} q_\tau = \begin{cases} 0 & , \tau < \sigma \\ \Delta_\tau \left((\partial_{x_\sigma} |\Psi_\tau\rangle)^\dagger \hat{\mathbb{P}}_p |\Psi_\tau\rangle + \text{h.c.}\right) & , \tau = \sigma \\ \Delta_\tau \left((\partial_{x_\sigma} |\Psi_\tau\rangle)^\dagger \hat{\mathbb{P}}_p |\Psi_\tau\rangle + \text{h.c.}\right) + \partial_{x_\sigma} q_{\tau-1} & , \tau > \sigma \end{cases}$$

8.A.3   Improving Propagation Efficiency

So far, we only considered the general task of finding solutions to the equations of motion. However, doing so efficiently is crucial. Straightforward implementation of the above steps 5a and 5b, for the case $\tau > \sigma$, suggest that nested loops with a total of $\frac{1}{2} N_\tau (N_\tau - 1)$ steps are required. Given that, in order for the PWC approximation to be accurate [114, 118], N_τ typically is of order $\mathcal{O}(10^3)$ or higher, and hence the $\mathcal{O}(N_\tau^2)$ complexity to propagate gradients poses serious limitations in terms of efficiency.

We proceed to show that a careful analysis of the propagation scheme allows to reduce complexity from $\mathcal{O}(N_\tau^2)$ to $\mathcal{O}(N_\tau)$. Let $N_\tau > 6$, and examine $\partial_{x_\sigma} |\Psi\rangle$ for $\sigma = 3$, starting with $\tau = 3$ because this corresponds to the first time $\partial_{x_\sigma} |\Psi_\tau\rangle$ is non-zero:

$$\partial_{x_3} |\Psi_3\rangle = \left(\partial_{x_3} \hat{U}_3 \right) |\Psi_2\rangle$$

$$\partial_{x_3} |\Psi_4\rangle = \hat{U}_4 \partial_{x_3} |\Psi_3\rangle = \hat{U}_4 \left(\partial_{x_3} \hat{U}_3 \right) |\Psi_2\rangle$$

$$\partial_{x_3} |\Psi_5\rangle = \hat{U}_5 \partial_{x_3} |\Psi_4\rangle = \hat{U}_5 \hat{U}_4 \left(\partial_{x_3} \hat{U}_3 \right) |\Psi_2\rangle$$

$$\partial_{x_3} |\Psi_6\rangle = \hat{U}_6 \partial_{x_3} |\Psi_5\rangle = \hat{U}_6 \hat{U}_5 \hat{U}_4 \left(\partial_{x_3} \hat{U}_3 \right) |\Psi_2\rangle$$

$$\vdots$$

$$\partial_{x_3} |\Psi_{N_\tau}\rangle = \hat{U}_{N_\tau} \partial_{x_3} |\Psi_{N_\tau - 1}\rangle = \hat{U}_{N_\tau} \hat{U}_{N_\tau - 1} \ldots \hat{U}_6 \hat{U}_5 \hat{U}_4 \left(\partial_{x_3} \hat{U}_3 \right) |\Psi_2\rangle \quad (8.22)$$

Equation (8.22) suggests precomputing the terms

$$A_\tau = \hat{U}_\tau \hat{U}_{\tau-1} \hat{U}_{\tau-2} \ldots \hat{U}_2 \hat{U}_1, \tag{8.23}$$

$$B_\tau = \hat{U}_{N_\tau} \hat{U}_{N_\tau - 1} \hat{U}_{N_\tau - 2} \ldots \hat{U}_{\tau+1} \hat{U}_\tau. \tag{8.24}$$

Using the iterative relations $\hat{A}_0 = \hat{\mathbb{1}}$, $\hat{A}_\tau = \hat{U}_\tau \hat{A}_{\tau-1}$ and $\hat{B}_{N_{\tau+1}} = \hat{\mathbb{1}}$, $\hat{B}_\tau = \hat{B}_{\tau+1} \hat{U}_\tau$, which can be done $\mathcal{O}(N_\tau)$ complexity at step 2, we can then compute all $\partial_{x_\sigma} |\Psi_{N_\tau}\rangle$ in $\mathcal{O}(N_\tau)$ time, following

$$\partial_{x_\sigma} |\Psi_{N_\tau}\rangle = \hat{B}_{\sigma+1} \left(\partial_{x_\sigma} \hat{U}_\sigma \right) \hat{A}_{\sigma-1} |\Psi_0\rangle. \tag{8.25}$$

A similar derivation holds for the gradients of q. We note that for $k \geq j$, $\hat{U}_k \hat{U}_{k-1} \hat{U}_{k-2} \ldots \hat{U}_j = \hat{B}_{k+1}^\dagger \hat{B}_j$. In order to reduce complexity the additional condition that $\Delta_\tau = \Delta$, $\forall \tau = 1, \ldots, N_\tau$ is required. The penalty gradients

are given by

$$
\begin{aligned}
\partial_{x_\sigma} q_{N_\tau} &= 2\Delta \operatorname{Re}\left\{ \sum_{\tau=\sigma}^{N_\tau} \left(\hat{B}_{\tau+1}^\dagger \hat{B}_{\sigma+1} \left(\partial_{x_\sigma}\hat{U}_\sigma\right) \hat{A}_{\sigma-1} \left|\Psi_0\right\rangle \right)^\dagger \hat{\mathbb{P}}_p \hat{A}_\tau \left|\Psi_0\right\rangle \right\} \\
&= 2\Delta \operatorname{Re}\left\{ \left\langle\Psi_0\right| \left(\sum_{\tau=\sigma}^{N_\tau} \hat{A}_{\sigma-1}^\dagger \left(\partial_{x_\sigma}\hat{U}_\sigma\right)^\dagger \hat{B}_{\sigma+1}^\dagger \hat{B}_{\tau+1} \hat{\mathbb{P}}_p \hat{A}_\tau \right) \left|\Psi_0\right\rangle \right\} \\
&= 2\Delta \operatorname{Re}\left\{ \left\langle\Psi_0\right| \left(\hat{A}_{\sigma-1}^\dagger \left(\partial_{x_\sigma}\hat{U}_\sigma\right)^\dagger \hat{B}_{\sigma+1}^\dagger \right) \left(\sum_{\tau=\sigma}^{N_\tau} \hat{B}_{\tau+1} \hat{\mathbb{P}}_p \hat{A}_\tau \right) \left|\Psi_0\right\rangle \right\}
\end{aligned}
$$

$$(8.26)$$

We note that $(\hat{A}_{\sigma-1}^\dagger(\partial_{x_\sigma}\hat{U}_\sigma)^\dagger \hat{B}_{\sigma+1}^\dagger)$ is independent of τ and can therefore be evaluated only once per σ at cost $\mathcal{O}(N_\tau)$. Similarly, each term in the summation $\sum_{\tau=\sigma}^{N_\tau} \hat{B}_{\tau+1}\hat{\mathbb{P}}_p\hat{A}_\tau$ is a matrix multiplication of three matrices that are easily computed at runtime. The sum, i.e. the entire expression (8.26) as a function of σ, can be computed one term at a time (starting with $\sigma = N_\tau$ and working back to $\sigma = 1$), again requiring only $\mathcal{O}(N_\tau)$ time.

Part III

Adiabatic Quantum Computation

Chapter 9

Introduction

The majority of the previous part addressed the implementation of accurate gates, and as such focused on discrete quantum gates within the quantum circuit model. We will now discuss Adiabatic Quantum Computation [199] (AQC), which is a promising alternative to the quantum circuit model of computation [16]. The first idea of using adiabatic evolution for solving computational problems appeared in [245] where adiabaticity is used to solve classical combinatorial problems, and was referred to as quantum stochastic optimization. Later on [246] the term Quantum Annealing (QA) was introduced. It essentially describes a quantum extension of the classical simulated annealing algorithm [124], and can natively be implemented in the instruction set of an AQC platform [247]. Similar ideas arose and created terminology such as quantum adiabatic algorithms [248] and adiabatic quantum optimization [249]. When the term AQC first appeared [250] it was solely focused on optimization but has extended its scope to become an alternate approach to the circuit model over the last years.

Essentially, in order to solve certain problems using AQC one needs to encode the solution to a given problem in the ground state of a Hamiltonian $\hat{H}_1$ [199]. For computationally hard problems, this ground state is typically prohibitively slow to reach. Hence, one constructs a Hamiltonian $\hat{H}(s) = (1-s)\hat{H}_0 + s\hat{H}_1$ with a fully characterized Hamiltonian $\hat{H}_0$ and a parameter $s \in [0, 1]$ which represents normalized time. At the beginning of the computation ($s = 0$) the system $\hat{H}(0)$ will be prepared in the easily accessible ground state of $\hat{H}_0$. As explained in section 6.1, adiabatically changing s from 0 to 1 ensures that the Hamiltonian $\hat{H}(s)$ will remain in its ground state, and hence,

at $s = 1$, one can extract the sought ground state of $\hat{H}_1$. This approach to quantum computation has been shown [251] to be conceptually as powerful as the quantum circuit model, and can hence be considered as universal. There are various advantages that make AQC/QA appealing, such as an increased robustness against decoherence [252] and simpler control. Another downside of the quantum circuit model is the effect of finite temperatures: Generally, one wants to operate at the lowest possible temperature in order to reduce harmful effects originating in non-unitary dynamics [253]. In the context of AQC/QA, however, a thermal environment is expected to be actually helpful [254, 255].

At the time of writing, commercialization of quantum annealing devices is pioneered by the Canadian quantum computing company D-Wave Systems. Currently, their newest device features about 2000 qubits [256], arranged in a Chimera topology [257] which only allows for limited couplings since every qubit couples to six others. Whether their quantum annealing devices, which undoubtedly demonstrate impressive engineering achievements, exhibit true quantum speedup is still an open question. An extensive study on the topic was performed in 2014 [258], suggesting that no quantum speedup was found. Recent work confirms these results, showing that claims of quantum speedup are typically based on unfair comparisons, or related to benchmark problems that were specifically designed to give the D-Wave quantum annealer an advantage [259]. A recently initiated multi-institutional collaboration called *Quantum Enhanced Optimization (QEO)* [260], which comprises more than 100 researchers, aims at exploring the limits of coherent quantum annealing devices and improving their quality [261]. One goal of the project is to build a quantum annealer featuring non-stoquastic coupling terms. For instance, the latter are believed to be required in order that the quantum annealer can no longer be efficiently simulated by classical Quantum Monte Carlo methods [262].

We proceed to discuss the fundamentals of an adiabatic quantum algorithm that can be shown to feature a true quantum speedup compared to its classical analog. As an example of quantum speedup via AQC we will review the adiabatic Grover algorithm [263] and follow the discussion given in [199].

9.1   Searching an Unsorted Database

The general idea of the Grover algorithm [5] can be summarized as finding a specific element (or multiple ones) within an unsorted database of N items with the fewest possible number of database queries. Formally, this task can be formulated as follows: A function $f : \{0,1\}^n \to \{0,1\}$ is known to suffice

$f(m) = 1$ and $f(x) = 0 \; \forall x \neq m$, and $N = 2^n$ is the number of bit strings. The Grover algorithm addresses the problem of finding m with the minimum number of evaluations of f. The function f is referred to as an *oracle* and we will consider it as a given black box, so that only the complexity of the actual algorithm is under review.

Classically, the database has to be queried element by element until the marked item m is found. Hence, the average number of queries to find m will scale linearly with the number of elements N. In the adiabatic Grover algorithm we define the oracle in terms of the final Hamiltonian $\hat{H}_1 = \hat{\mathbb{1}} - |m\rangle\langle m|$. Here, $|m\rangle$ represents the marked state corresponding to the item m to be found. The binary representation is associated to the eigenvalues of the Pauli operator $\hat{\sigma}_z$, that is $\hat{\sigma}_z |0\rangle = +|0\rangle$ and $\hat{\sigma}_z |1\rangle = -|1\rangle$. That way, the marked state $|m\rangle$ equals the ground state of Hamiltonian $\hat{H}_1$ with eigenvalue 0, and all other basis states have energy 1. We now proceed to discuss the key elements of the adiabatic Grover algorithm. For a detailed discussion the reader is referred to Refs.[199, 263].

9.2 Initialization of the Algorithm

A successful operation of the quantum Grover algorithm requires an initialization in a well-known initial Hamiltonian $\hat{H}_0$. In case of the Grover search algorithm the initial Hamiltonian is $\hat{H}_0 = \hat{\mathbb{1}} - |\phi\rangle\langle\phi|$, where

$$|\phi\rangle = \frac{1}{\sqrt{N}} \sum_{j=0}^{N-1} |j\rangle = |+\rangle^{\otimes n} \tag{9.1}$$

is a uniform superposition state and $|\pm\rangle = (|0\rangle \pm |1\rangle)/\sqrt{2}$. $|\phi\rangle$ is the ground state of $\hat{H}_0$ so that if the full Hamiltonian $\hat{H}(s) = (1-s)\hat{H}_0 + s\hat{H}_1$ is initially prepared in $|\psi(0)\rangle = |\phi\rangle$ the evolution of the system can be reduced to a two-dimensional subspace $\mathcal{Q}$ which is defined by the span of states $|m\rangle$ and $|m^\perp\rangle$. Here,

$$|m^\perp\rangle = \frac{1}{\sqrt{N-1}} \sum_{j \neq m} |j\rangle \tag{9.2}$$

is the superposition of all states other than $|m\rangle$. The eigensystem of the two-dimensional Hamiltonian $\hat{H}(s)$ in subspace $\mathcal{Q}$ can be solved exactly and reveals an energy gap $\Delta(s)$ between the two lowest-energy states according to [199]

$$\Delta(s) = \sqrt{(1-2s)^2 + \frac{4}{N} s(1-s)}. \tag{9.3}$$

This yields a minimal gap $\Delta_{\min} = 1/\sqrt{N} = 2^{-n/2}$ in the middle of the sweep, i.e. for $s = 1/2$. Applying the adiabatic theorem, the adiabatic condition becomes [199]

$$t_g \gg \frac{3}{\Delta_{\min}^2} = 3N. \tag{9.4}$$

Only if the sweep duration t_g is larger that $3/\Delta_{\min}^2$ the annealing procedure will be adiabatic and return the correct result $|m\rangle$. However, inequality (9.4) suggests a scaling much like in classical algorithms: The minimal time scales linearly with the number of items N in the database.

9.3   Demonstration of Quantum Speedup

Based on the above discussion there is no quantum speedup for the quantum Grover algorithm. Yet, the process can be optimized to achieve a quadratic quantum speedup over the classical database search. To this end we write the full annealing Hamiltonian in the more general form $\hat{H}(s) = (1 - A(s))\hat{H}_0 + A(s)\hat{H}_1$, where $A(s)$ is the so-called *annealing schedule*. Before, we only considered the situation of linear annealing schedules $A(s) = s$. An optimized annealing schedule that slows down near the minimum gap can be used to demonstrate quantum speedup. Similar ideas have a long history in NMR [264] and are also key in recent research [150, 151].

A simple annealing schedule that serves for demonstration purposes is to choose $\partial_t A(t) = c\Delta^2[A(t)]$, where c is a constant, with the necessary boundary condition $A(0) = 0$ and $A(t_g) = 1$. This reflects that the annealing schedule adapts to the energy gap and eventually yields the result [199]

$$t_g = \frac{N}{c\sqrt{N-1}}\text{atan}\left(\sqrt{N-1}\right) \xrightarrow{N \gg 1} \frac{\pi}{2c}\sqrt{N}. \tag{9.5}$$

Indeed, equation (9.5) demonstrates a quadratic quantum speedup of the adiabatic Grover algorithm over the classical scenario which scales proportional to N. Note that from equation (9.5) it seems that the sweep duration can be made arbitrarily small by increasing the constant c. However, the error due to the adiabatic approximation is directly related to the value of c, suggesting that the adiabatic error increases with increasing c [199].

The analysis above assumes exact knowledge of the minimum energy gap to find a better annealing schedule. Generally, for complex problems, the energy spectrum is unknown and hence it is hard to determine optimized annealing schedules *a priori*. Finding optimized annealing schedules will not be part of this thesis and the reader is referred to literature [199, 263, 265–269] for an overview of the current state of the art.

Chapter 10

Hybrid Quantum-Classical Annealing

In chapter 9 we introduced the basics of AQC and mentioned its advantages compared to the quantum circuit model. Nevertheless, there are some downsides that need to be considered when implementing AQC/QA: Perfectly adiabatic sweeps require infinite time. Since, both in numerics and experiments, sweep lengths are inevitably finite, there will always be diabatic excitation errors [151], as can be seen from studies of avoided crossings by means of of Landau-Zener (LZ) physics [270, 271]. Moreover, although there is evidence for thermally assisted AQC (TA-AQC), it remains a general question how thermal excitations of states close to the ground state can be avoided and/or be reverted efficiently. Since the spectral gap Δ between the ground state and the next higher state is generally unknown [253] it remains an important task to find efficient cooling schemes that are independent of Δ. Present cooling schemes such as Sisyphus cooling [272] and evaporative cooling [273] can in principle be used to cool qubits, but unfortunately require knowledge of the energy gap and are hence not well-suited for general applications.

In this chapter we will present a cooling scheme that is independent of the energy gap Δ. Without loss of generality we focus on an annealing platform based on superconducting flux qubits [274] and restrict our analysis to the dynamics of dissipative Landau-Zener systems. We provide a schematic circuit diagram and a set of quantum master equations that accurately describe the associated spin-boson dynamics of the driven dissipative Landau-Zener system, showing that gap-independent cooling can be achieved by coupling the

---
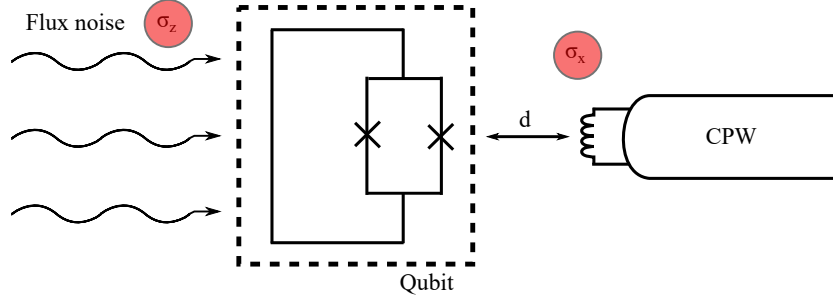
FIG. 10.1 – Schematic circuit diagram to implement both $\hat{\sigma}_x$ and $\hat{\sigma}_z$ coupling to a superconducting flux qubit. While the flux noise ($\hat{\sigma}_z$) is always present, we propose to add an additional $\hat{\sigma}_x$ coupling in terms of a coplanar waveguide (CPW) at distance d from the qubit. The $\hat{\sigma}_x$-coupling strength can be controlled directly by altering d.

qubit transversely to an ohmic environment, in addition to always-present longitudinal thermal noise. Since the effect of the additional transverse coupling can be understood as supplementing the quantum annealing procedure with additional classical annealing, we call the proposed scheme *Hybrid Quantum-Classical Annealing* (HQCA).

10.1 System Model and Equations of Motion

As a toy model we restrict ourselves to a dissipative Landau-Zener problem, governed by a spin-boson model [275]. The bare system Hamiltonian $\hat{H}_Q(t)$ features a generally time-dependent drive $\epsilon(t)$ and a constant tunneling amplitude Δ, i.e.

$$\hat{H}_Q(t) = -\frac{\epsilon(t)}{2}\hat{\sigma}_z - \frac{\Delta}{2}\hat{\sigma}_x, \tag{10.1}$$

where the $\hat{\sigma}_j$ denote the Pauli matrices. In the simplest non-trivial model, $\epsilon(t)$ is linear in time with sweep velocity v and y-intercept ϵ_0, i.e. $\epsilon(t) = vt + \epsilon_0$. Without loss of generality we will assume $\epsilon_0 = 0$ in the remainder of this chapter and let the sweep take place within the time interval $[-t_0, t_0]$ with t_0 chosen such that the initial energy splitting is large compared to the minimal gap Δ. This serves as a proper toy model, especially if the two eigenstates can be mapped to well-isolated adiabatic states of a larger system. In fact, a system that features such an isolated small gap has been engineered and analyzed with respect to the influence of (thermal) noise [276]. The full Hamiltonian of our system is given by the bare qubit $\hat{H}_Q$, the heat bath $\hat{H}_B$

and the qubit-environment coupling terms $\hat{H}_{QB}$. We model each heat bath as harmonic oscillators, and assume that both X- and Z-couplings are present. We will refer to these couplings as *transverse* and *longitudinal*, respectively. The respective Hamiltonians are then given by

$$\hat{H}_{QB} = \sum_{\nu=x,z} \sum_k \hat{\sigma}_\nu \lambda_{k,\nu} \left(\hat{b}_{k,\nu} + \hat{b}_{k,\nu}^\dagger \right), \qquad (10.2a)$$

$$\hat{H}_B = \sum_{\nu=x,z} \sum_k \omega_{k,\nu} \hat{b}_{k,\nu}^\dagger \hat{b}_{k,\nu}. \qquad (10.2b)$$

Based on previous ideas and experiments [277–280] we propose a cooling scheme via an additional $\hat{\sigma}_x$ coupling by using a coplanar waveguide (CPW) as an environment, as shown in FIG. 10.1. The coupling strength to the qubit can be controlled by modifying the distance d between CPW and qubit. In order to derive an analytic set of equations of motions for the qubit subsystem, we follow the core idea of the standard Bloch-Redfield formalism [111]. An adequate model to describe the physics of AQC/QA is the spin-boson model [275], which properly characterizes the coupling of some quantum system with an external environment. In order to obtain analytic expressions for the equations of motion in case of generic time-dependent Hamiltonians we apply an appropriate formulation [281, 282] of the Bloch-Redfield theory. Following Refs.[255, 281] we transform to a frame defined by the time-dependent rotation $\hat{R}(t) = \exp\left(i\phi(t)\hat{\sigma}_y/2\right)$. Since the transformation is time-dependent the qubit Hamiltonian acquires an additional inertial term, which can be related to non-stoquastic interactions in a multi-qubit scenario [262], so that the Landau-Zener Hamiltonian in the rotating frame reads

$$\hat{\tilde{H}}_Q(t) = \hat{R}^\dagger(t)\hat{H}_Q(t)\hat{R}(t) + i\dot{\hat{R}}^\dagger(t)\hat{R}(t) = -\frac{E(t)}{2}\hat{\sigma}_x + \frac{\dot{\phi}(t)}{2}\hat{\sigma}_y, \qquad (10.3)$$

where we use the mixing angle $\phi(t) = \mathrm{atan}(\epsilon(t)/\Delta)$ and the instantaneous energy splitting $E(t) = \sqrt{\Delta^2 + \epsilon^2(t)}$. We denote all other operators in that frame by a tilde, i.e. $\hat{\tilde{O}}(t) = \hat{R}^\dagger(t)\hat{O}(t)\hat{R}(t)$. For later use we define $\hat{\tilde{H}}_0(t) \equiv -E(t)\hat{\sigma}_x/2$. Analogously, the qubit-environment coupling becomes

$$\hat{\tilde{H}}_{QB}(t) = \sum_{\nu=x,z} \sum_k \hat{\tilde{\sigma}}_\nu(t)\lambda_{k,\nu}\left(\hat{b}_{k,\nu} + \hat{b}_{k,\nu}^\dagger \right) \qquad (10.4)$$

with $\hat{\tilde{\sigma}}_\nu(t)$ being the Pauli matrices in the rotating frame. By introducing the weights $f_1(t) = \sin(\phi(t))$ and $f_2(t) = \cos(\phi(t))$ we can express the rotating-frame-matrices as $\hat{\tilde{\sigma}}_x(t) = -f_1(t)\hat{\sigma}_z + f_2(t)\hat{\sigma}_x$ and $\hat{\tilde{\sigma}}_z(t) = f_2(t)\hat{\sigma}_z + f_1(t)\hat{\sigma}_x$, respectively. In order to provide closed analytical expressions for the equations

of motion, one employs standard Markovian approximations and an additional adiabatic-Markovian approximation [281] (AMA). The latter is inevitable to deal with the interaction picture transformation needed to carry out the time-dependent Bloch-Redfield formalism. A detailed derivation of the equations of motion is given in Appendix 10.A. The AMA features two important parts: (i) the memory time τ_{mem} of the bath is assumed to be much smaller than any system time scale and (ii) the drive $\epsilon(t)$ acts only on timescales much larger than τ_{mem} so that it has no significant contribution to the rates. This, in turn, allows to derive the Bloch equations for the density matrix $\hat{\bar{\rho}}_Q(t) = (\hat{\mathbb{1}} + \sum_n b_n(t)\hat{\sigma}_n)/2$ associated to the qubit subsystem (10.3). The Bloch vector (b_x, b_y, b_z) is determined by the set of quantum master equations (QME)

$$\dot{b}_x = \left(\dot{\phi} - \gamma_{xz}\right) b_z - \gamma_r \left(b_x - \bar{b}_x\right), \tag{10.5a}$$

$$\dot{b}_y = E_t b_z - \left(\gamma_d + \gamma_r\right) b_y, \tag{10.5b}$$

$$\dot{b}_z = -\dot{\phi} b_x - E_t b_y - \gamma_d b_z - \gamma_{zx} \left(b_x - \bar{b}_x\right). \tag{10.5c}$$

Here, we use the shorthand notation $E_t \equiv E(t), \bar{b}_x \equiv \tanh(\beta E_t/2)$ and defined the set of rates

$$\gamma_r = 2\pi\coth\left(\frac{\beta E_t}{2}\right) \left(\sin^2(\phi)J_x(E_t) + \cos^2(\phi)J_z(E_t)\right), \tag{10.6a}$$

$$\gamma_d = 4\pi \lim_{\omega \to 0} \bar{n}(\omega) \left(J_z(\omega) + J_x(\omega)\right), \tag{10.6b}$$

$$\gamma_{xz} = 4\pi\sin(\phi)\cos(\phi) \lim_{\omega \to 0} \bar{n}(\omega) \left(J_x(\omega) - J_z(\omega)\right), \tag{10.6c}$$

$$\gamma_{zx} = 2\pi\sin(\phi)\cos(\phi)\coth\left(\frac{\beta E_t}{2}\right) \left(J_x(E_t) - J_z(E_t)\right), \tag{10.6d}$$

that depend on the spectral densities $J_\nu(\omega)$ of the respective environments, and the Bose distribution $\bar{n}(\omega) = 1/(e^{\beta\omega} - 1)$, where $\beta = 1/k_B T$. Relaxation is encoded in γ_r, while γ_d and $\gamma_{zx,xz}$ describe pure dephasing and cross-dephasing, respectively. We stress that the Bloch-type equations (10.5) are based on a proper treatment of external drives. The performed AMA might suggest that the QME are only valid inside the adiabatic regime, i.e. when $v \ll \Delta^2$. However, even for non-adiabatic drives they are still a good approximation. This has been verified numerically for a similar Hamiltonian in Ref. [255] by comparing the numerical solutions of their equivalent of equations (10.5) to a numerically exact solution obtained via the path integral based method QUAPI [283]. Furthermore, a detailed analysis of the assumptions that lead to the QME in terms of different timescales was carried out in Ref. [282].
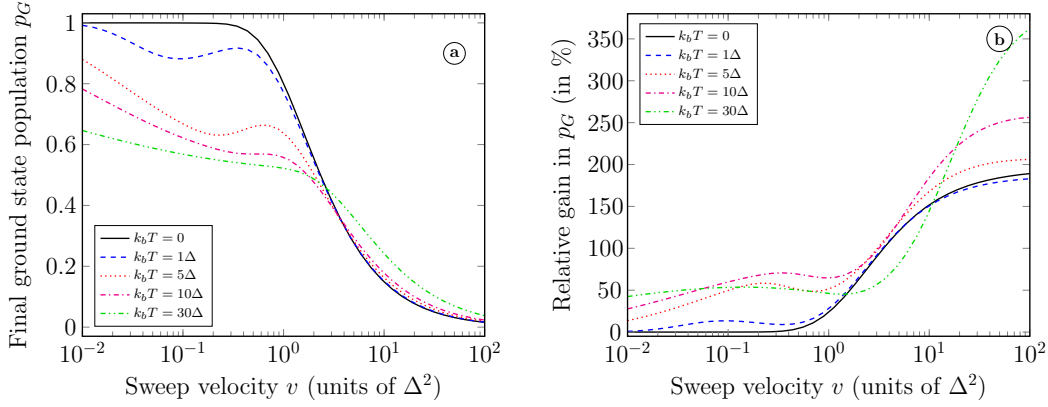
FIG. 10.2 – (a): Final ground state population p_G as a function of sweep velocity v for a $\hat{\sigma}_z$-only coupling with coupling strength $\alpha_z = 5 \cdot 10^{-3}$ at different temperatures. Clearly, even for small velocities and small temperatures, a significant amount of population is lost into the excited state owing to heating. (b): Relative improvement of p_G compared to the data in (a) if an additional CPW is used as a transversely coupled ($\hat{\sigma}_x$) heat bath with coupling strength $\alpha_x = \alpha_z$, i.e. we plot $(p_G^{(x,z)} - p_G^{(z)})/p_G^{(z)}$ where the superscript indicates the type of couplings in the system. In the adiabatic regime we find improvements of about 50% while the cooling effect in the non-adiabatic regime is even more pronounced with gains of a few hundred percent. Generally, the gain increases with temperature – indicating proper TA-AQC.

10.2 Environmental engineering

In our analysis we restrict ourselves to the case of ohmic heat baths [284, 285]. That is, the spectral densities $J_\nu(\omega)$ depend linearly on ω. However, this model is only valid up to some high-frequency cutoff $\omega_{c,\nu}$. For our purpose, we choose to work with an exponential cutoff at frequencies $\omega_{c,\nu} = 10\Delta$ whereby the exact numerical value has an irrelevant impact on the quality of our results. Different coupling strengths are modeled by the parameter α_ν, so that the spectral density is eventually given by $J_\nu(\omega) = \alpha_\nu \omega e^{-\omega/\omega_{c,\nu}}$. With this explicit form of $J(\omega)$ we compute the limit $\lim_{\omega \to 0} \bar{n}(\omega) J_\nu(\omega)$, needed in equations (10.6), to be equal to α_ν/β. We simulate the QME (10.5) with initial conditions set up such that the system will always start in the exact ground state of Hamiltonian (10.3). We use the final ground state population p_G after a full Landau-Zener sweep as our figure of merit to evaluate cooling effects.

FIG. 10.2a shows the dependence of p_G on sweep velocity v and temperature T, for pure $\hat{\sigma}_z$ coupling with $\alpha_z = 5 \cdot 10^{-3}$. As expected, heating

in form of thermal excitations increases with temperature, substantiated by significant population loss compared to coherent dynamics. If temperatures are not too high, i.e. $k_B T \lesssim 5\Delta$, there is a locally optimal velocity v_0 at which the sum of diabatic errors due to finite sweep length and thermal excitations are minimized [286, 287]. However, since both v_0 and $p_G(v_0)$ strongly depend on α_z and temperature T, a sweep with velocity v_0 would be a tradeoff which generally still features poor performance. Instead, we deduce from FIG. 10.2b that an additional CPW, coupled transversely via $\hat{\sigma}_x$ with $\alpha_x = \alpha_z$, generally performs significantly better compared to the situation where only longitudinal thermal noise is present. The relative gain is defined as $(p_G^{(x,z)} - p_G^{(z)})/p_G^{(z)}$, where the superscript indicates which types of environment couple to the system. Moreover, we find that – except for a small subset of velocities – higher temperatures lead to better results than low-temperature simulations. We therefore argue that an additional transversely coupled heat bath not only reduces heating – it also properly demonstrates TA-AQC [254]: The benefit of a thermal environment during open system dynamics. We observe this effect even for $\alpha_z > \alpha_x$, remarking that it is slightly attenuated compared to the situation $\alpha_z \leq \alpha_x$. Aside, we note that the results for higher temperatures serve as a mock-up for small energy gaps.

In case of pure thermal noise $(\hat{\sigma}_z)$, the effect of TA-AQC in the non-adiabatic regime is negligible for any reasonable values of α_z. Nevertheless, for $\alpha_z \gtrsim \mathcal{O}(0.01)$, we find appreciable indications for TA-AQC even without an additional CPW. A detailed numerical study of how the final ground state population depends on both coupling constants, for fixed temperature $k_B T = 5\Delta$ and fixed velocity $v = 0.5\Delta^2$, is depicted in FIG. 10.3a. Comparing to the behavior of $p_G(\alpha_z)$ without a CPW, as shown in FIG. 10.3b, the advantage of an additional $\hat{\sigma}_x$ heat bath becomes apparent: As soon as even small couplings α_x are present, pronounced relaxation after sweeping through the avoided crossing leads to significant cooling of the system. This is substantiated by equation (10.6a): Contributions to the relaxation rate γ_r are non-negative, so that additional transverse coupling overall amplifies relaxation processes.

Based on the concept of frustrated decoherence [277, 278] one might suspect that excitations into the excited state are effectively blocked due to the non-commutativity of $\hat{\sigma}_x$ and $\hat{\sigma}_z$. However, we do not observe such quantum effects (which are similar to the Zeno blockade [288]) and attribute the efficiency of the cooling scheme solely to enhanced relaxation, as evidenced by the numerics in Appendix 10.B. Hence, the general quantum annealing process is supported by relaxation at finite temperatures which must be smaller than $E(t)$ well outside the avoided crossing regime. The presence of energy relaxation is reminiscent of classical simulated annealing [124]. We therefore refer to our method as *Hybrid Quantum-Classical Annealing* (HQCA).
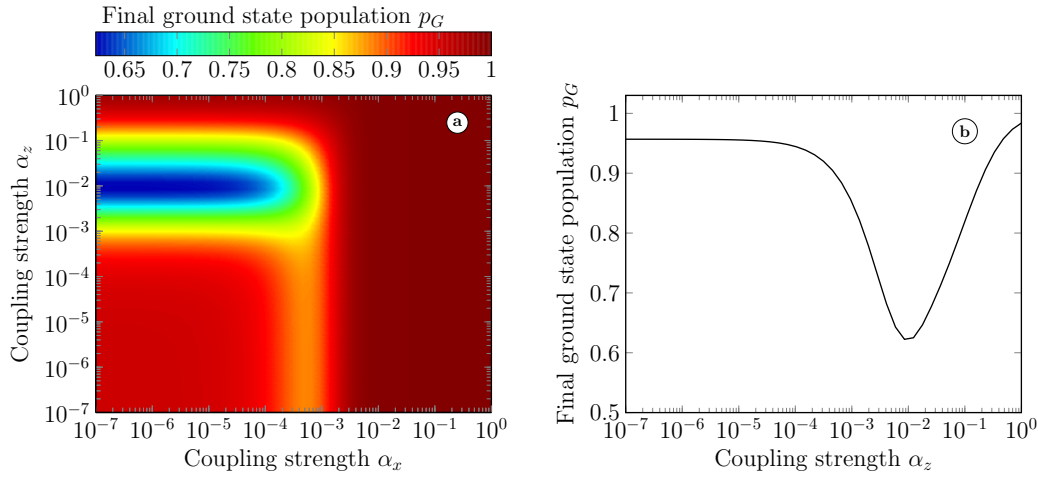
FIG. 10.3 – (a) Dependence of the final ground state population p_G on the coupling strengths α_x and α_z for a temperature of $k_B T = 5\Delta$ at a sweep velocity $v = 0.5\Delta^2$. The velocity is chosen such that it corresponds to a local optimum of $p_G(v)$ as extracted from FIG. 10.2a. (b) Dependence of p_G on α_z without the existence of an additional CPW, i.e. for $\alpha_x = 0$, with identical parameters as in (a). The minimum is reached at $\alpha_{z,0} \approx 0.01$.

If the transverse coupling exceeds $\alpha_x \gtrsim 5 \cdot 10^{-3}$, roughly all population has relaxed back to the ground state by the end of the sweep – irrespective of α_z. The value $\alpha_{z,0}$ where the curve $p_G(\alpha_z)$ reaches its minimum decreases with increasing temperature. Note that the non-monotonic behavior of $p_G(\alpha_z)$ in FIG. 10.3b can be explained using a key result of Ref. [289], where the authors show how dissipative dynamics merge into semiclassical dynamics if the associated rates exceed a certain temperature-dependent value: In that case, the final ground state population will be approximately given by the result of coherent dynamics – which can be estimated via the Landau-Zener formula $p_{\mathrm{LZ}} = 1 - e^{-\pi\Delta^2/2v}$ [270, 271]. For the parameters in FIG. 10.3 this corresponds to a semiclassical limit of about 0.95, which is in good agreement with the curve in FIG. 10.3b for $\alpha_z \approx 1$.

10.3   Conclusion

In conclusion, we presented a gap-independent cooling scheme for a quantum system affected by thermal $\hat{\sigma}_z$ noise. The method outlined in this chapter generally increases the ground state population after sweeping through an avoided crossing at finite temperatures, owing to enhanced relaxation processes induced by an additional transversely coupled heat bath in form of

a coplanar waveguide. We find significant numerical evidence of thermally assisted quantum annealing, and numerically demonstrated that the proposed cooling scheme is capable of improving ground state populations by up to a few hundred percent. Thereby we developed a method that has the potential to improve the quality of current quantum annealing devices. Recall that all parameters are independent of the energy gap, so that our cooling scheme is intrinsically robust against energy fluctuations.

Our results suggest that the optimal annealing device is hybridizes quantum and classical annealing: While quantum annealing allows to circumvent local traps at constant energy, classical annealing (in form of relaxation induced by transverse couplings to an environment) ultimately lowers the energy. We hence refer to our scheme as Hybrid Quantum-Classical Annealing (HQCA). For further details on the derivation of the underlying QME (10.5) and numerical details that illustrate enhanced relaxation processes, we refer the reader to appendices 10.A and 10.B, respectively.

Appendix

10.A Derivation of the Quantum Master Equations

We provide details on the derivation of the quantum master equation. The total Hamiltonian is decomposed as

$$\hat{H}(t) = \hat{H}_Q(t) + \hat{H}_{QB} + \hat{H}_B, \text{ with} \tag{10.7}$$

$$\hat{H}_Q(t) = -\frac{\epsilon(t)}{2}\hat{\sigma}_z - \frac{\Delta}{2}\hat{\sigma}_x \tag{10.8}$$

$$\hat{H}_{QB} = \sum_{\nu=x,z}\sum_k \hat{\sigma}_\nu \lambda_{k,\nu} \left(\hat{b}_{k,\nu} + \hat{b}_{k,\nu}^\dagger \right), \tag{10.9}$$

$$\hat{H}_B = \sum_{\nu=x,z}\sum_k \omega_{k,\nu} \hat{b}_{k,\nu}^\dagger \hat{b}_{k,\nu}. \tag{10.10}$$

Following Ref. [281], we move to the rotating frame defined by the transformation $\hat{R}(t) = \exp\left(i\phi(t)\hat{\sigma}_y/2\right)$ with $\phi(t) = \mathrm{atan}(\epsilon(t)/\Delta)$. With the instantaneous energy splitting $E(t) = \sqrt{\epsilon^2(t) + \Delta^2}$ the bare system Hamiltonian and the coupling term become

$$\hat{\tilde{H}}_Q(t) = -\frac{E(t)}{2}\hat{\sigma}_x + \frac{\dot{\phi}(t)}{2}\hat{\sigma}_y \equiv \hat{\tilde{H}}_0 + \frac{\dot{\phi}(t)}{2}\hat{\sigma}_y, \tag{10.11}$$

$$\hat{\tilde{H}}_{QB}(t) = \sum_{\nu=x,z}\sum_k \hat{\tilde{\sigma}}_\nu(t) \lambda_{k,\nu} \left(\hat{b}_{k,\nu} + \hat{b}_{k,\nu}^\dagger \right). \tag{10.12}$$

All operators other than $\hat{\tilde{H}}_Q$ in that frame follow the transformation rule $\hat{\tilde{O}}(t) = \hat{R}^\dagger(t)\hat{O}(t)\hat{R}(t)$. By introducing the weights $f_1(t) = \sin(\phi(t))$ and $f_2(t) = \cos(\phi(t))$ we express the rotating-frame Pauli matrices as

$$\hat{\tilde{\sigma}}_x(t) = -f_1(t)\hat{\sigma}_z + f_2(t)\hat{\sigma}_x, \quad \hat{\tilde{\sigma}}_z(t) = f_2(t)\hat{\sigma}_z + f_1(t)\hat{\sigma}_x. \tag{10.13}$$

Following standard Bloch-Redfield theory (cf. section 3.3 in [111]) we start in the interaction frame with respect to $\hat{\tilde{H}}_Q$ and $\hat{\tilde{H}}_B$. Hence, the coupling Hamiltonian in the interaction picture is given by

$$\hat{\tilde{H}}_{QB,I}(t) = \sum_{\nu=x,z} \hat{\tilde{U}}_Q^\dagger(t)\hat{\tilde{\sigma}}_\nu(t)\hat{\tilde{U}}_Q(t) \otimes \hat{B}_\nu(t)$$

$$\hat{B}_\nu(t) = \sum_k \lambda_{k,\nu} \left(e^{i\omega_{k,\nu}t}\hat{b}_{k,\nu}^\dagger + e^{-i\omega_{k,\nu}t}\hat{b}_{k,\nu} \right) \tag{10.14}$$

with some bath operator $\hat{B}_\nu$ and the free propagator of the bare qubit $\hat{\tilde{U}}_Q(t) = \hat{\mathcal{T}}\exp\left(-i\int_0^t \hat{\tilde{H}}_Q(t')\mathrm{d}t'\right)$. The equation of motion for the density matrix of the reduced qubit subsystem is hence given by

$$\dot{\hat{\tilde{\rho}}}_{Q,I}(t) = -\int_0^\infty \mathrm{d}s \, \mathrm{Tr}_B \left\{ \left[\hat{\tilde{H}}_{QB,I}(t), \left[\hat{\tilde{H}}_{QB,I}(t-s), \hat{\tilde{\rho}}_{Q,I}(t) \otimes \hat{\rho}_B \right] \right] \right\}$$

$$= -\int_0^\infty \mathrm{d}s \sum_{\nu,\nu'} \left\{ \hat{\tilde{\sigma}}_{\nu,I}(t)\hat{\tilde{\sigma}}_{\nu',I}(t-s)\hat{\tilde{\rho}}_{Q,I}(t) \langle \hat{B}_\nu(t)\hat{B}_{\nu'}(t-s)\rangle \right.$$

$$\left. -\hat{\tilde{\sigma}}_{\nu,I}(t)\hat{\tilde{\rho}}_{Q,I}(t)\hat{\tilde{\sigma}}_{\nu',I}(t-s) \langle \hat{B}_{\nu'}(t-s)\hat{B}_\nu(t)\rangle + \mathrm{h.c.} \right\}$$

In the above equation we have already included (i) a weak-coupling approximation (Born approximation), which states that the reservoir is negligibly affected by the system so that we may write the full density matrix as a tensor product $\hat{\tilde{\rho}}(t) = \hat{\tilde{\rho}}_Q(t) \otimes \hat{\rho}_B$ and (ii) a Markovian approximation. The latter states that there is no memory, i.e. time evolution of the state depends only on its present value, and is based on the assumption that the correlation functions decay sufficiently fast compared to the time scale over which the system changes notably. If we choose $\hat{\rho}_B$ to be a stationary state of the reservoir, the correlation functions are homogeneous in time, hence $\langle \hat{B}_\alpha(t)\hat{B}_\beta(t-s)\rangle = \langle \hat{B}_\alpha(s)\hat{B}_\beta(0)\rangle$. Furthermore we assume that there is no correlation between different baths, i.e. $\langle \hat{B}_\alpha(s)\hat{B}_\beta(0)\rangle \propto \delta_{\alpha\beta}$. We can then write equation (10.15) in the form

$$\dot{\hat{\tilde{\rho}}}_{Q,I}(t) = -\int_0^\infty \mathrm{d}s \sum_{\nu=x,z} \left\{ \left[\hat{\tilde{\sigma}}_{\nu,I}(t), \hat{\tilde{\sigma}}_{\nu,I}(t-s)\hat{\tilde{\rho}}_{Q,I}(t) \right] \langle \hat{B}_\nu(s)\hat{B}_\nu(0)\rangle + \mathrm{h.c.} \right\}. \tag{10.15}$$

We are looking for the equation of motion in the Schrödinger picture, that is the evolution of $\hat{\tilde{\rho}}_Q(t)$, given by $\dot{\hat{\tilde{\rho}}}_Q(t) = \hat{\tilde{U}}_Q(t)\dot{\hat{\tilde{\rho}}}_{Q,I}(t)\hat{\tilde{U}}_Q^\dagger(t) - i[\hat{\tilde{H}}_Q(t), \hat{\tilde{\rho}}_Q(t)]$.

A straightforward calculation reveals the sought equation of motion in the Schrödinger picture to be

$$\dot{\hat{\bar{\rho}}}_Q(t) = -i \left[\hat{\bar{H}}_Q(t), \hat{\bar{\rho}}_Q(t) \right] - \sum_{\nu=x,z} \left\{ \left[\hat{\bar{\sigma}}_\nu(t), \hat{\bar{S}}_\nu(t)\hat{\bar{\rho}}_Q(t) \right] + \text{h.c.} \right\} \qquad (10.16)$$

where we introduced the operator

$$\hat{\bar{S}}_\nu(t) = \int\limits_0^\infty \mathrm{d}s\, \hat{\bar{U}}_Q(t,t-s)\hat{\bar{\sigma}}_\nu(t-s)\hat{\bar{U}}_Q^\dagger(t,t-s) \left\langle \hat{B}_\nu(s)\hat{B}_\nu(0) \right\rangle. \qquad (10.17)$$

In order to derive an analytic form for the equation of motion we further need to apply an adiabatic Markovian approximation [281] which amounts to expressing the propagator as

$$\hat{\bar{U}}_Q(t,t-s) \approx \exp\left(-i\hat{\bar{H}}_Q(t)s \right). \qquad (10.18)$$

This is sufficiently accurate provided the memory time τ_{mem} of the bath is much smaller than any system time scale, $\tau_{\text{mem}} \ll (t-s)$, and if the drive $\epsilon(t)$ acts on time scales $\tau_\epsilon \gg \tau_{\text{mem}}$ so that it has no significant effect on the rates. The correlation function can be expressed in terms of the spectral density $J_\nu(\omega)$ of the bath (cf section 3.1.4 in [275]):

$$\left\langle \hat{B}_\nu(s)\hat{B}_\nu(0) \right\rangle = \int\limits_0^\infty \mathrm{d}\omega\, J_\nu(\omega) \left[e^{-i\omega s} \left(\bar{n}_\nu(\omega) + 1 \right) + e^{i\omega s}\bar{n}_\nu(\omega) \right] \qquad (10.19)$$

with the single-particle Bose distribution $\bar{n}_\nu(\omega) = 1/(e^{\beta_\nu\omega} - 1)$. Using the identity $\bar{n}_\nu(-\omega) = -(\bar{n}_\nu(\omega)+1)$ we can rewrite equation (10.19) as an integral over positive and negative ω, i.e.

$$\left\langle \hat{B}_\nu(s)\hat{B}_\nu(0) \right\rangle = \int\limits_{-\infty}^\infty \mathrm{d}\omega\, \text{sgn}(\omega)J_\nu(|\omega|)\bar{n}_\nu(\omega)e^{i\omega s}. \qquad (10.20)$$

Inserting equation (10.20) into the definition (10.17) allows us to carry out the integration over s first, which yields terms $\int_0^\infty \mathrm{d}s e^{i\omega s} \approx \pi\delta(\omega)$. Note that we here neglect imaginary parts resulting from principal value integrals since they simply manifest themselves as Lamb shifts. Calculating the right hand side of equation (10.16) while using the Bloch representation $\hat{\bar{\rho}}_Q(t) = (\hat{\mathbb{1}}+\sum_n b_n(t)\hat{\sigma}_n)/2$ we eventually find the quantum master equations presented
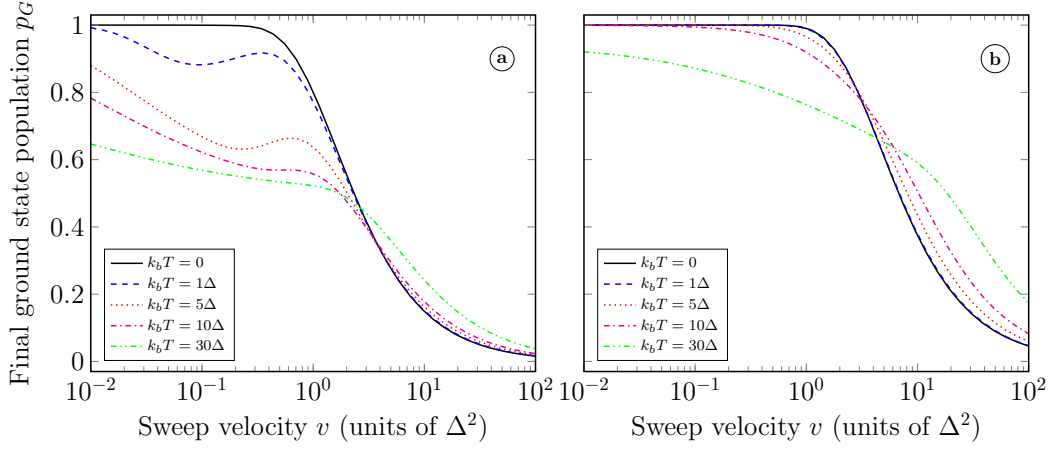
FIG. 10.4 – (a) Final ground state population p_G as a function of the sweep velocity v for a $\hat{\sigma}_z$-only coupling with coupling strength $\alpha_z = 5 \cdot 10^{-3}$ at different temperatures. (b) Final ground state population for same parameters as in (a) but with additional transverse coupler.

in the main article,

$$\dot{b}_x = \left(\dot{\phi} - \gamma_{xz}\right) b_z - \gamma_r \left(b_x - \bar{b}_x\right), \tag{10.5a}$$

$$\dot{b}_y = E_t b_z - \left(\gamma_d + \gamma_r\right) b_y, \tag{10.5b}$$

$$\dot{b}_z = -\dot{\phi} b_x - E_t b_y - \gamma_d b_z - \gamma_{zx} \left(b_x - \bar{b}_x\right). \tag{10.5c}$$

Here, we use the shorthand notation $E_t \equiv E(t)$, $\bar{b}_x \equiv \tanh(\beta E_t/2)$. Note that we assume same temperatures for both baths since, in experiments, they will both be located in the same cyrostat. The rates are then given by

$$\gamma_r = 2\pi\coth\left(\frac{\beta E_t}{2}\right) \left(\sin^2(\phi)J_x(E_t) + \cos^2(\phi)J_z(E_t)\right), \tag{10.6a}$$

$$\gamma_d = 4\pi \lim_{\omega \to 0} \bar{n}(\omega) \left(J_z(\omega) + J_x(\omega)\right), \tag{10.6b}$$

$$\gamma_{xz} = 4\pi\sin(\phi)\cos(\phi) \lim_{\omega \to 0} \bar{n}(\omega) \left(J_x(\omega) - J_z(\omega)\right), \tag{10.6c}$$

$$\gamma_{zx} = 2\pi\sin(\phi)\cos(\phi)\coth\left(\frac{\beta E_t}{2}\right) \left(J_x(E_t) - J_z(E_t)\right). \tag{10.6d}$$

10.B Numerical Verification of Relaxation and Cooling

In addition to the graphics shown in the main part of chapter 10, we want to further support the statements by providing additional numerical data. For
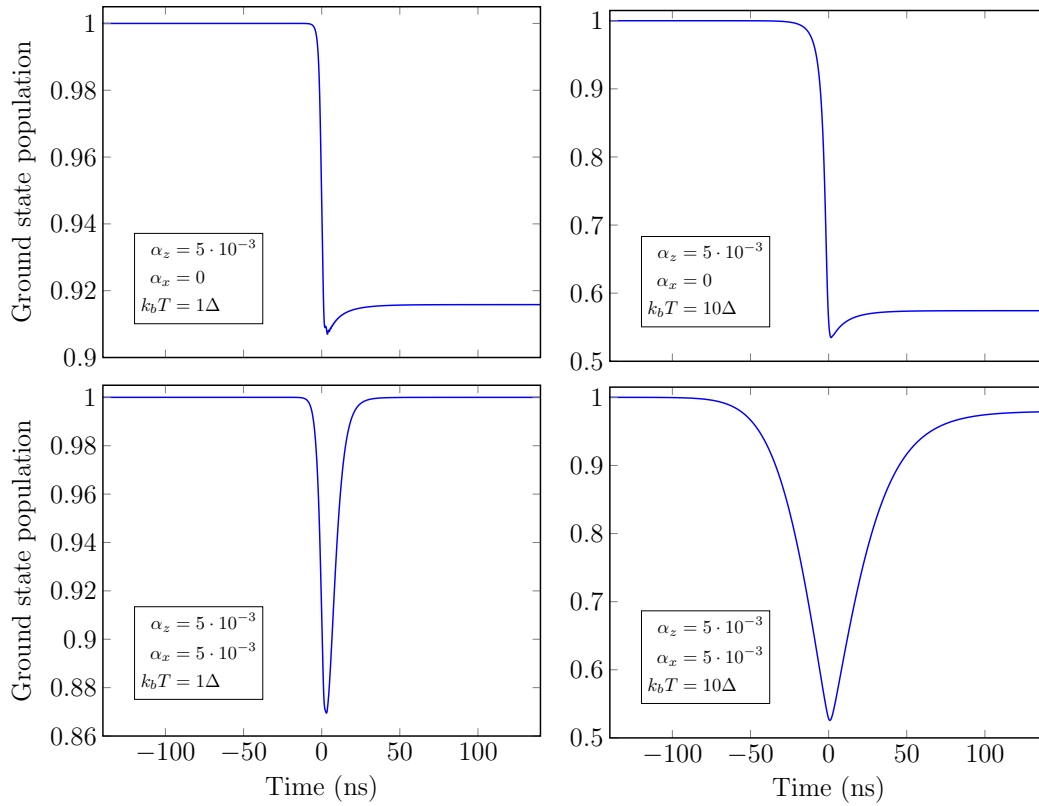
FIG. 10.5 – Population of the ground state as a function of time for different parameter settings with sweep velocity $v = 0.3\Delta^2$. As apparent from the pics/annealing, an additional transverse coupling does not reduce intermediate excitations. Cooling into the ground state is achieved by relaxation back into the ground state.

an absolute comparison of how the final ground state population depends on temperature and sweep velocity, please see FIG. 10.4. Our statement that cooling is solely caused by relaxation processes is supported by FIG. 10.5, which depicts the evolution of ground state population for different parameter settings. If the CPW is transversely coupled to the qubit, excitation out of the ground state is not minimized intermediately. Instead, population relaxes back into the ground state after passing the avoided crossing. We find qualitatively identical dynamics for other parameter regimes as well.

Conclusion

With a variety of already known near- and long-term applications, quantum information processing and computation is of great interest for many areas of science, such as physics, chemistry, biology and pharmaceutics. To date, accurate coherent quantum control has been demonstrated with on the order of ten qubits. Simple algorithms, for instance to compute the energy surface of molecular hydrogen, were carried out successfully and substantiate impressive progress in terms of single- and multi-qubit control over the last decade. Quantum gates achieve fidelities at which error correction via surface codes become useful and indeed simple instances of error correction have already been demonstrated. Nevertheless, building a large-scale fault-tolerant universal quantum computer still seems out of reach. It will require hundreds or thousands of logical qubits, with significant overhead required to implement error correction protocols. Scaling up current quantum systems poses immense challenges to both physics and engineering: Readout and control electronics need to be developed for large-scale applications, algorithms and control protocols need to be carefully designed to minimize overhead when scaling up, and likely a variety of other yet unknown problems remain to be mastered on the course of building a usable quantum computer. A major focus of this thesis was the development of a simple but accurate model of coupled qubits, and the design of optimal waveforms to implement high-fidelity entangling gates on short timescales. Achieving high fidelities is an important means to significantly reduce overhead due to additional physical qubits required for error correction, while short gate times allow to reduce errors due to decoherence and parameter drifts.

In order to determine solutions for accurate quantum control it is inevitable to utilize models of high accuracy. In chapter 5 we provided a framework that can be used to derive accurate effective Hamiltonians of arbitrary time-dependence. Implementing entangling gates between dispersively coupled superconducting qubits is a generic example of where our theory is of great relevance: Advanced control schemes that aim for shortest possible gate times require real-time control of the magnetic flux penetrating the qubits. However,

current models do not account for all effects due to this real-time control and hence lack accuracy. We provided a more exhaustive description of the physics and showed that gate errors deduced from different models can differ by up to 10^{-2} even for very smooth controls, which is on the same order as the lowest known error thresholds for quantum error correction schemes. This encourages to make use of our extended technique in order to reliably estimate the dynamics, which is for instance of particular interest for future applications of quantum optimal control in dispersively coupled systems, or others that are subject to similar Hamiltonians.

Successful implementation of theoretically optimal control pulses in experiments requires calibration of pulse parameters. Hereto it is preferable to parametrize the pulses in terms of simple analytic functions with the fewest possible amount of parameters. Undesired excitations of transitions that are in spectral vicinity of one or more targeted ones (this is referred to as *leakage*) are a major source of error when controlling quantum systems. Chapter 6 reviewed the prominent DRAG framework, which amounts to supporting a base waveform with its derivatives in order to minimize this type of errors by using only a minimal number of tunable parameters. We provided the first description of the theory that properly connects DRAG to related methodology, points out fundamental differences and highlights important aspects relevant for a successful application. To illustrate the power of the method we exemplarily applied it to multiple fundamentally different problems and provided an overview of further experimentally motivated applications.

Chapter 7 combines DRAG pulses and additional optimization of trap parameters to find optimal solutions to entangle Rydberg atoms via the Rydberg blockade interaction. Rydberg atoms – atoms excited to quantum states with large principle quantum numbers – are particularly attractive due to their strong long-range interaction with a huge on-off-ratio of about twelve orders of magnitude. Yet, separation between adjacent quantum states scales inversely with their quantum number so that these gates are very prone to leakage errors. So far it was unclear whether gates based on the Rydberg blockade interaction are capable of achieving fidelities better than 99.9% in a realistic model. The work presented in chapter 7 demonstrates that entangling gates with fidelities larger than 99.99% are indeed possible when accounting for the most relevant leakage channels and dissipative processes, even in room temperature environments. We showed that the required gate times are only 50 ns, outperforming previous protocols both in terms of gate times and fidelities by an order of magnitude. These results establish the potential of neutral atom qubits with Rydberg blockade gates for scalable quantum computation.

In chapter 8 we showed that coherent generation of maximally entangled

states between trapped ions, using Raman lasers, is possible with realistic fidelities of about 99% on sub-microsecond timescales. Hereto, we derived an accurate model that is free from common approximations which otherwise severely restrict the application of quantum optimal control. The error we achieve is comparable to that of advanced dissipative state preparation schemes, and just an order of magnitude lower than that of modern unitary control proposals. However, we operate on timescales that are two to four orders of magnitude below those reported in related literature. In order to better understand if dissipative preparation schemes – which tend to be intrinsically robust against certain experimental noise – are preferable over coherent control, we benchmarked our results against amplitude noise and variable initial conditions, indicating that unitary control sequences achieve appreciable robustness as well. Future research can directly connect to the methods and implications of chapter 8, and study the regime of low microsecond timescales, which should allow to improve state fidelities significantly, while still operating at much shorter time – suggesting that these solutions are also very robust against errors due to parameter drift and dephasing.

The above summary of part II mainly focused on the generation of high-fidelity entangling gates required for applications in the quantum circuit model, where quantum algorithms are divided into multiple discrete gates. Adiabatic quantum computation and quantum annealing are based on a different approach: Computational problems are solved by finding the ground state of a Hamiltonian by the use of adiabatic system control. Current state-of-the-art annealing devices, that are based on superconducting flux qubits, suffer from diabatic errors originating from imperfect adiabaticity due to finite sweep lengths and thermal excitations, induced by blackbody flux noise as the energy gap shrinks below temperature. In chapter 10 we used a dissipative Landau-Zener system to analyze these errors and proposed a remarkably simple solution to them: Adding a heat bath to a transverse, non-commuting observable allows the qubit to relax back to its ground state after the avoided crossing, enhancing cooling effects by up to a few hundred percent. A major advantage of this approach is its independence of the generally unknown energy gap. Based on its functionality, we called our approach hybrid quantum-classical annealing (HQCA) since it combines aspects of both quantum and classical annealing: While pure quantum annealing circumvents local traps at constant energy, additional classical annealing by enhanced relaxation ultimately lowers the energy. The analysis of chapter 10 is restricted to single-qubit problems and opens a future research project about cooling of multi-qubit instances. In this case, frustration becomes relevant and we expect that some modification of our current HQCA proposal is required to account for the additional degrees of freedom. While in the current proposal the amount

of cooling increases monotonically with transverse coupling strength, i.e. with enhanced classical annealing, we expect a sweet spot of transverse coupling strength for multi-qubit instances – corresponding to the optimal tradeoff between quantum and classical annealing.

Recent progress in quantum information science, especially using superconducting qubits, is extremely promising, and it is reasonable to believe that quantum supremacy will be demonstrated in the very near future. This refers to the successful operation of a computational task on quantum hardware which is impossible to run on classical computers. Despite this considerable progress, a myriad of fundamental and technological challenges remains to be solved before being able to build a usable large-scale quantum computer. In order to pursue this ultimate goal efficiently, it appears to be crucial to carefully analyze tradeoffs between quality and quantity of qubits. At the time of writing, it seems that first and foremost industrial research is almost only competing in terms of quantity. Press releases of bigger chips continuously make headlines, but there remains silence about actual performance of these chips over the course of more than half a year already. This suggests that, while of course quantity is an important aspect of scaling up current proof of principle experiments, fundamental research on the few-qubit level, as carried out in this thesis, is equally required and should potentially return to the focus of current research before claiming the next generation of larger quantum chips.

Publication List

Published/Accepted

1. <u>L. S. Theis</u>, F. Motzoi, S. Machnes and F. K. Wilhelm
   Counteracting systems of diabaticities using DRAG controls: The status after 10 years
   Invited *Focus* article: EPL **123**, 60001 (2018)

2. M. A. Rol, C. C. Bultink, T. E. O'Brien, S. R. de Jong, <u>L. S. Theis</u>, X. Fu, F. Luthi, R. F. L. Vermeulen, J. C. de Sterke, A. Bruno, D. Deurloo, R. N. Schouten, F. K. Wilhelm and L. DiCarlo
   Restless Tuneup of High-Fidelity Qubit Gates
   Phys. Rev. Applied **7**, 041001 (2017)

3. <u>L. S. Theis</u> and F. K. Wilhelm
   Nonadiabatic corrections to fast dispersive multiqubit gates involving Z control
   Phys. Rev. A **95**, 022314 (2017)

4. <u>L. S. Theis</u>, F. Motzoi, F. K. Wilhelm and M. Saffman
   High-fidelity Rydberg-blockade entangling gate using shaped analytic pulses
   Phys. Rev. A **94**, 032306 (2016)

Submitted

1. <u>L. S. Theis</u>, Peter K. Schuhmacher, M. Marthaler and F. K. Wilhelm
   Gap-independent cooling and hybrid quantum-classical annealing
   Submitted for peer-review in Physical Review Letters.
   Preprint available: arXiv:1808.09873 (2018)

In Preparation

1. <u>L. S. Theis</u>, S. Machnes, G. Morigi and F. K. Wilhelm
   Coherent and Robust Entanglement of Trapped Ions in the Sub-Micro-second Regime

Previous Publications

1. <u>L. S. Theis</u>, F. Motzoi and F. K. Wilhelm
   Simultaneous gates in frequency-crowded multilevel systems using fast, robust, analytic control shapes
   Phys. Rev. A **93**, 012324 (2016)

2. T. Chasseur, <u>L. S. Theis</u>, Y. R. Sanders, D. J. Egger and F. K. Wilhelm
   Engineering adiabaticity at an avoided crossing with optimal control
   Phys. Rev. A **91**, 043421 (2015)

Bibliography

[1] A. Acín, I. Bloch, H. Buhrman, T. Calarco, C. Eichler, J. Eisert, D. Esteve, N. Gisin, S. J. Glaser, F. Jelezko, S. Kuhr, M. Lewenstein, M. F. Riedel, P. O. Schmidt, R. Thew, A. Wallraff, I. Walmsley, and F. K. Wilhelm, "The quantum technologies roadmap: a European community view", New J. Phys. **20**, 080201 (2018).

[2] R. P. Feynman, "Simulating physics with computers", Int. J. Theor. Phys. **21**, 467 (1982).

[3] D. Deutsch, "Quantum theory, the church-turing principle and the universal quantum computer", P. Roy. Soc. A: Math. Phys. **400**, 97 (1985).

[4] D. Deutsch and R. Jozsa, "Rapid solution of problems by quantum computation", P. Roy. Soc. A: Math. Phys. **439**, 553 (1992).

[5] L. K. Grover, "A fast quantum mechanical algorithm for database search", in Proceedings of the twenty-eighth annual ACM symposium on theory of computing - STOC'96 (1996).

[6] P. W. Shor, "Polynomial-time algorithms for prime factorization and discrete logarithms on a quantum computer", SIAM J. Comput. **26**, 1484 (1997).

[7] D. Gil, "The future is quantum", IBM Quantum computing blog (2017-11-10), visited on: 2018-09-03.

[8] "2018 CES: Intel advances quantum and neuromorphic computing research", Intel newsroom (2018-01-08), visited on: 2018-09-03.

[9] J. Kelly, "A preview of Bristlecone, Google's New Quantum Processor", Google AI blog (2018-03-05), visited on: 2018-09-03.

[10] S. Boixo, S. V. Isakov, V. N. Smelyanskiy, R. Babbush, N. Ding, Z. Jiang, M. J. Bremner, J. M. Martinis, and H. Neven, "Characterizing quantum supremacy in near-term devices", Nat. Phys. **14**, 595 (2018).

[11] B. M. Terhal, "Quantum supremacy, here we come", Nat. Phys. **14**, 530 (2018).

[12] P. J. J. O'Malley, R. Babbush, I. D. Kivlichan, J. Romero, J. R. Mc-Clean, R. Barends, J. Kelly, P. Roushan, A. Tranter, N. Ding, B. Campbell, Y. Chen, Z. Chen, B. Chiaro, A. Dunsworth, A. G. Fowler, E. Jeffrey, E. Lucero, A. Megrant, J. Y. Mutus, M. Neeley, C. Neill, C. Quintana, D. Sank, A. Vainsencher, J. Wenner, T. C. White, P. V. Coveney, P. J. Love, H. Neven, A. Aspuru-Guzik, and J. M. Martinis, "Scalable quantum simulation of molecular energies", Phys. Rev. X **6**, 031007 (2016).

[13] R. Babbush, N. Wiebe, J. McClean, J. McClain, H. Neven, and G. K.-L. Chan, "Low-depth quantum simulation of materials", Phys. Rev. X **8**, 011044 (2018).

[14] K. Kugler, B. Ohs, M. Scholz, and M. Wessling, "Towards a carbon independent and CO_2-free electrochemical membrane process for NH_3 synthesis", Phys. Chem. Chem. Phys. **16**, 6129 (2014).

[15] J. J. Sakurai and J. Napolitano, *Modern quantum mechanics* (Cambridge University Press, 2017).

[16] M. A. Nielsen and I. L. Chuang, *Quantum computation and quantum information* (Cambridge University Press, 2010).

[17] G. Vidal and C. M. Dawson, "Universal quantum circuit for two-qubit transformations with three controlled-not gates", Phys. Rev. A **69**, 010301 (2004).

[18] D. P. DiVincenzo, *Mesoscopic electron transport*, edited by L. L. Sohn, L. P. Kouwenhoven, and G. Schön (Springer Netherlands, 1997), pp. 657–677.

[19] D. Loss and D. P. DiVincenzo, "Quantum computation with quantum dots", Phys. Rev. A **57**, 120 (1998).

[20] E. Knill, "Quantum computing with realistically noisy devices", Nature **434**, 39 (2005).

[21] A. G. Fowler, A. M. Stephens, and P. Groszkowski, "High-threshold universal quantum computation on the surface code", Phys. Rev. A **80**, 052312 (2009).

[22] F. K. Wilhelm, R. Steinwandt, B. Langenberg, P. J. Liebermann, A. Messinger, and P. K. Schuhmacher, "Entwicklungsstand Quantencomputer", BSI Project Number **283** (2018).

[23] Y. Makhlin, G. Schön, and A. Shnirman, "Quantum-state engineering with Josephson-junction devices", Rev. Mod. Phys. **73**, 357 (2001).

[24] M. H. Devoret and J. M. Martinis, "Implementing qubits with superconducting integrated circuits", Quantum Inf. Process. **3**, 163 (2004).

[25] R. Schoelkopf and S. Girvin, "Wiring up quantum systems", Nature **451**, 664 (2008).

[26] J. Clarke and F. K. Wilhelm, "Superconducting quantum bits", Nature **453**, 1031 (2008).

[27] M. H. Devoret and R. J. Schoelkopf, "Superconducting circuits for quantum information: an outlook", Science **339**, 1169 (2013).

[28] M. Tinkham, *Introduction to Superconductivity*, 2nd edition, Dover Books on Physics (Dover Publications, 2004).

[29] B. Josephson, "Possible new effects in superconductive tunnelling", Physics Letters **1**, 251 (1962).

[30] J. Martinis, S. Nam, J. Aumentado, and C. Urbina, "Rabi oscillations in a large josephson-junction qubit", Phys. Rev. Lett. **89**, 117901 (2002).

[31] J. Mooij, T. Orlando, L. Levitov, L. Tian, C. van der Wal, and S. Lloyd, "Josephson persistent-current qubit", Science **285**, 1036 (1999).

[32] V. Bouchiat, D. Vion, P. Joyez, D. Esteve, and M. H. Devoret, "Quantum coherence with a single cooper pair", Phys. Scripta **T76**, 165 (1998).

[33] Y. Nakamura, Y. Pashkin, and J. Tsai, "Coherent control of macroscopic quantum states in a single-Cooper-pair box", Nature **398**, 786 (1999).

[34] J. Koch, T. M. Yu, J. Gambetta, A. A. Houck, D. I. Schuster, J. Majer, A. Blais, M. H. Devoret, S. M. Girvin, and R. J. Schoelkopf, "Charge-insensitive qubit design derived from the Cooper pair box", Phys. Rev. A **76**, 042319 (2007).

[35] R. Barends, J. Kelly, A. Megrant, D. Sank, E. Jeffrey, Y. Chen, Y. Yin, B. Chiaro, J. Mutus, C. Neill, P. O'Malley, P. Roushan, J. Wenner, T. C. White, A. N. Cleland, and J. M. Martinis, "Coherent josephson qubit suitable for scalable quantum integrated circuits", Phys. Rev. Lett. **111**, 080502 (2013).

[36] M. R. Geller, E. J. Pritchett, A. T. Sornborger, and F. K. Wilhelm, "Quantum Computing with Superconductors I: Architectures", in *Manipulating quantum coherence in solid state systems* (Springer Netherlands, 2007), pp. 171–194.

[37] Y. Nakamura, Y. A. Pashkin, T. Yamamoto, and J. S. Tsai, "Charge echo in a cooper-pair box", Phys. Rev. Lett. **88**, 047901 (2002).

[38] A. A. Houck, J. Koch, M. H. Devoret, S. M. Girvin, and R. J. Schoelkopf, "Life after charge noise: recent results with transmon qubits", Quantum Inf. Process. **8**, 105 (2009).

[39] H Paik, D. Schuster, L. Bishop, G. Kirchmair, G. Catelani, A. P. Sears, B. R. Johnson, M. J. Reagor, L. Frunzio, L. I. Glazman, S. M. Girvin, M. H. Devoret, and R. J. Schoelkopf, "Observation of High Coherence in Josephson Junction Qubits Measured in a Three-Dimensional Circuit QED Architecture", Phys. Rev. Lett. **107**, 240501 (2011).

[40] F. Motzoi, J. M. Gambetta, P. Rebentrost, and F. K. Wilhelm, "Simple Pulses for Elimination of Leakage in Weakly Nonlinear Qubits", Phys. Rev. Lett. **103**, 110501 (2009).

[41] Gambetta, J. M., Motzoi, F., Merkel, S. T., Wilhelm, and F. K., "Analytic control methods for high-fidelity unitary operations in a weakly nonlinear oscillator", Phys. Rev. A **83**, 012308 (2011).

[42] A. Blais, R.-S. Huang, A. Wallraff, S. M. Girvin, and R. J. Schoelkopf, "Cavity quantum electrodynamics for superconducting electrical circuits: An architecture for quantum computation", Phys. Rev. A **69**, 062320 (2004).

[43] A. Blais, J. Gambetta, A. Wallraff, D. I. Schuster, S. M. Girvin, M. H. Devoret, and R. J. Schoelkopf, "Quantum-information processing with circuit quantum electrodynamics", Phys. Rev. A **75**, 032329 (2007).

[44] H. Mabuchi, "Cavity Quantum Electrodynamics: Coherence in Context", Science **298**, 1372 (2002).

[45] T. Hime, P. A. Reichardt, B. L. T. Plourde, T. L. Robertson, C.-E. Wu, A. V. Ustinov, and J. Clarke, "Solid-State Qubits with Current-Controlled Coupling", Science **314**, 1427 (2006).

[46] Y. Chen, C. Neill, P. Roushan, N. Leung, M. Fang, R. Barends, J. Kelly, B. Campbell, Z. Chen, B. Chiaro, A. Dunsworth, E. Jeffrey, A. Megrant, J. Y. Mutus, P. J. J. O'Malley, C. M. Quintana, D. Sank, A. Vainsencher, J. Wenner, T. C. White, M. R. Geller, A. N. Cleland, and J. M. Martinis, "Qubit architecture with high coherence and fast tunable coupling", Phys. Rev. Lett. **113**, 220502 (2014).

[47] R. Barends, J. Kelly, A. Megrant, A. Veitia, D. Sank, E. Jeffrey, T. C. White, J. Mutus, A. G. Fowler, B. Campbell, Y. Chen, Z. Chen, B. Chiaro, A. Dunsworth, C. Neill, P. O/'Malley, P. Roushan, A. Vainsencher, J. Wenner, A. N. Korotkov, A. N. Cleland, and J. M. Martinis, "Superconducting quantum circuits at the surface code threshold for fault tolerance", Nature **508**, 500 (2014).

[48] J. Kelly, R. Barends, A. G. Fowler, A. Megrant, E. Jeffrey, T. C. White, D. Sank, J. Y. Mutus, B. Campbell, Y. Chen, Z. Chen, B. Chiaro, A. Dunsworth, I.-C. Hoi, C. Neill, P. J. J. O'Malley, C. Quintana, P. Roushan, A. Vainsencher, J. Wenner, A. N. Cleland, and J. M. Martinis, "State preservation by repetitive error detection in a superconducting quantum circuit", Nature **519**, 66 (2015).

[49] S. Sheldon, E. Magesan, J. M. Chow, and J. M. Gambetta, "Procedure for systematically tuning up cross-talk in the cross-resonance gate", Phys. Rev. A **93**, 060302 (2016).

[50] K. R. Brown, A. C. Wilson, Y. Colombe, C. Ospelkaus, A. M. Meier, E. Knill, D. Leibfried, and D. J. Wineland, "Single-qubit-gate error below 10^{-4} in a trapped ion", Phys. Rev. A **84**, 030303 (2011).

[51] C. J. Ballance, T. P. Harty, N. M. Linke, M. A. Sepiol, and D. M. Lucas, "High-fidelity quantum logic gates using trapped-ion hyperfine qubits", Phys. Rev. Lett. **117**, 060504 (2016).

[52] P. Schindler, J. T. Barreiro, T. Monz, V. Nebendahl, D. Nigg, M. Chwalla, M. Hennrich, and R. Blatt, "Experimental repetitive quantum error correction", Science **332**, 1059 (2011).

[53] A. Bermudez, X. Xu, R. Nigmatullin, J. O'Gorman, V. Negnevitsky, P. Schindler, T. Monz, U. G. Poschinger, C. Hempel, J. Home, F. Schmidt-Kaler, M. Biercuk, R. Blatt, S. Benjamin, and M. Müller, "Assessing the progress of trapped-ion processors towards fault-tolerant quantum computation", Phys. Rev. X **7**, 041061 (2017).

[54] C. Monroe and J. Kim, "Scaling the Ion Trap Quantum Processor", Science **339**, 1164 (2013).

[55] M. F. Brandl, "A Quantum von Neumann Architecture for Large-Scale Quantum Computing", arXiv:1702.02583 (2017).

[56] D. J. Wineland, "Quantum information processing and quantum control with trapped atomic ions", Phys. Scripta **T137**, 014007 (2009).

[57] F. Rohde and J. Eschner, "Quantum computation with trapped ions and atoms", in *Ultracold gases and quantum information* (Oxford University Press, 2011), pp. 218–252.

[58] K. R. Brown, J. Kim, and C. Monroe, "Co-designing a scalable quantum computer with trapped atomic ions", npj Quantum Information **2** (2016).

[59] D. J. Wineland, M. Barrett, J. Britton, J. Chiaverini, B. DeMarco, W. M. Itano, B. Jelenkovic, C. Langer, D. Leibfried, V. Meyer, T. Rosenband, and T. Schatz, "Quantum information processing with trapped ions", Philos. T. R. Soc. A **361**, 1349 (2003).

[60] D. Wineland, C. Monroe, W. Itano, D. Leibfried, B. King, and D. Meekhof, "Experimental issues in coherent quantum-state manipulation of trapped atomic ions", J. Res. Natl. Inst. Stan. **103**, 259 (1998).

[61] D. Leibfried, R. Blatt, C. Monroe, and D. Wineland, "Quantum dynamics of single trapped ions", Rev. Mod. Phys. **75**, 281 (2003).

[62] W. K. Hensinger, "Microwave ion-trap quantum computing", Nature **476**, 155 (2011).

[63] C. Ospelkaus, U. Warring, Y. Colombe, K. R. Brown, J. M. Amini, D. Leibfried, and D. J. Wineland, "Microwave quantum logic gates for trapped ions", Nature **476**, 181 (2011).

[64] N. Timoney, I. Baumgart, M. Johanning, A. F. Varón, M. B. Plenio, A. Retzker, and C. Wunderlich, "Quantum gates and memory using microwave-dressed states", Nature **476**, 185 (2011).

[65] S. Earnshaw, "On the Nature of the Molecular Forces which Regulate the Constitution of the Luminiferous Ether", Trans. Camb. Phil. Soc. **7**, 97 (1842).

[66] W. Paul, "Electromagnetic traps for charged and neutral particles", Rev. Mod. Phys. **62**, 531 (1990).

[67] R. J. Hughes, D. F. V. James, E. H. Knill, R. Laflamme, and A. G. Petschek, "Decoherence bounds on quantum computation with trapped ions", Phys. Rev. Lett. **77**, 3240 (1996).

[68] T. Monz, P. Schindler, J. T. Barreiro, M. Chwalla, D. Nigg, W. A. Coish, M. Harlander, W. Hänsel, M. Hennrich, and R. Blatt, "14-qubit entanglement: creation and coherence", Phys. Rev. Lett. **106**, 130506 (2011).

[69] J. W. Britton, B. C. Sawyer, A. C. Keith, C.-C. J. Wang, J. K. Freericks, H. Uys, M. J. Biercuk, and J. J. Bollinger, "Engineered two-dimensional ising interactions in a trapped-ion quantum simulator with hundreds of spins", Nature **484**, 489 (2012).

[70] D. Kielpinski, C. Monroe, and D. J. Wineland, "Architecture for a large-scale ion-trap quantum computer", Nature **417**, 709 (2002).

[71] M. D. Hughes, B. Lekitsch, J. A. Broersma, and W. K. Hensinger, "Microfabricated ion traps", Contemp. Phys. **52**, 505 (2011).

[72] R. C. Sterling, H. Rattanasonti, S. Weidt, K. Lake, P. Srinivasan, S. C. Webster, M. Kraft, and W. K. Hensinger, "Fabrication and operation of a two-dimensional ion-trap lattice on a high-voltage microchip", Nat. Commun. **5** (2014).

[73] D. F. V. James, "Quantum dynamics of cold trapped ions with application to quantum computation", Appl. Phys. B **66**, 181 (1998).

[74] A. Garg, "Decoherence in ion trap quantum computers", Phys. Rev. Lett. **77**, 964 (1996).

[75] J. P. Schiffer, "Phase transitions in anisotropically confined ionic crystals", Phys. Rev. Lett. **70**, 818 (1993).

[76] J. I. Cirac and P. Zoller, "Quantum Computations with Cold Trapped Ions", Phys. Rev. Lett. **74**, 4091 (1995).

[77] A. Sørensen and K. Mølmer, "Entanglement and quantum computation with ions in thermal motion", Phys. Rev. A **62**, 022311 (2000).

[78] J. D. Miller, R. A. Cline, and D. J. Heinzen, "Far-off-resonance optical trapping of atoms", Phys. Rev. A **47**, R4567 (1993).

[79] Z. Hu and H. J. Kimble, "Observation of a single atom in a magneto-optical trap", Opt. Lett. **19**, 1888 (1994).

[80] T. F. Gallagher, *Rydberg Atoms* (Cambridge University Press, 1994).

[81] M. Saffman, T. G. Walker, and K. Mølmer, "Quantum information with Rydberg atoms", Rev. Mod. Phys. **82**, 2313 (2010).

[82] D. D. Yavuz, P. B. Kulatunga, E. Urban, T. A. Johnson, N. Proite, T. Henage, T. G. Walker, and M. Saffman, "Fast ground state manipulation of neutral atoms in microscopic optical traps", Phys. Rev. Lett. **96**, 063001 (2006).

[83] C. Knoernschild, X. L. Zhang, L. Isenhower, A. T. Gill, F. P. Lu, M. Saffman, and J. Kim, "Independent individual addressing of multiple neutral atom qubits with a micromirror-based beam steering system", Appl. Phys. Lett. **97**, 134101 (2010).

[84] D. Schrader, I. Dotsenko, M. Khudaverdyan, Y. Miroshnychenko, A. Rauschenbeutel, and D. Meschede, "Neutral atom quantum register", Phys. Rev. Lett. **93**, 150501 (2004).

[85] I. Dotsenko, W. Alt, S. Kuhr, D. Schrader, M. Müller, Y. Miroshny-chenko, V. Gomer, A. Rauschenbeutel, and D. Meschede, "Application of electro-optically generated light fields for raman spectroscopy of trapped cesium atoms", Appl. Phys. B **78**, 711 (2004).

[86] Y. Wang, X. Zhang, T. A. Corcovilos, A. Kumar, and D. S. Weiss, "Coherent Addressing of Individual Neutral Atoms in a 3D Optical Lattice", Phys. Rev. Lett. **115**, 043003 (2015).

[87] T. Xia, M. Lichtman, K. Maller, A. W. Carr, M. J. Piotrowicz, L. Isenhower, and M. Saffman, "Randomized benchmarking of single-qubit gates in a 2D array of neutral-atom qubits", Phys. Rev. Lett. **114**, 100503 (2015).

[88] Y. Wang, A. Kumar, T.-Y. Wu, and D. S. Weiss, "Single-qubit gates based on targeted phase shifts in a 3d neutral atom array", Science **352**, 1562 (2016).

[89] K. M. Maller, M. T. Lichtman, T. Xia, Y. Sun, M. J. Piotrowicz, A. W. Carr, L. Isenhower, and M. Saffman, "Rydberg-blockade controlled-NOT gate and entanglement in two-dimensional array of neutral-atom qubits", Phys. Rev. A **92**, 022336 (2015).

[90] A. M. Kaufman, B. J. Lester, M. Foss-Feig, M. L. Wall, A. M. Rey, and C. A. Regal, "Entangling two transportable neutral atoms via local spin exchange", Nature **527**, 208 (2015).

[91] Y.-Y. Jau, A. M. Hankin, T. Keating, I. H. Deutsch, and G. W. Biedermann, "Entangling Atomic Spins with a Rydberg-dressed spin-flip blockade", Nat. Phys. **12**, 71 (2016).

[92] M Saffman, "Quantum computing with atomic qubits and Rydberg interactions: progress and challenges", J. Phys. B: At. Mol. Opt. **49**, 202001 (2016).

[93] L. Santos, G. V. Shlyapnikov, P. Zoller, and M. Lewenstein, "Bose-Einstein Condensation in Trapped Dipolar Gases", Phys. Rev. Lett. **85**, 1791 (2000).

[94] H. Weimer, M. Müller, I. Lesanovsky, P. Zoller, and H. P. Büchler, "A Rydberg quantum simulator", Nat. Phys. **6**, 382 (2010).

[95] D. D. B. Rao and K. Mølmer, "Dark Entangled Steady States of Interacting Rydberg Atoms", Phys. Rev. Lett. **111**, 033606 (2013).

[96]   L. Isenhower, E. Urban, X. L. Zhang, A. T. Gill, T. Henage, T. A. Johnson, T. G. Walker, and M. Saffman, "Demonstration of a neutral atom controlled-not quantum gate", Phys. Rev. Lett. **104**, 010503 (2010).

[97]   T. Wilk, A. Gaëtan, C. Evellin, J. Wolters, Y. Miroshnychenko, P. Grangier, and A. Browaeys, "Entanglement of two individual neutral atoms using rydberg blockade", Phys. Rev. Lett. **104**, 010502 (2010).

[98]   L. S. Theis, F. Motzoi, F. K. Wilhelm, and M. Saffman, "High-fidelity Rydberg-blockade entangling gate using shaped, analytic pulses", Phys. Rev. A **94**, 032306 (2016).

[99]   J. Stehlik, Y. Dovzhenko, J. R. Petta, J. R. Johansson, F. Nori, H. Lu, and A. C. Gossard, "Landau-zener-stückelberg interferometry of a single electron charge qubit", Phys. Rev. B **86**, 121303 (2012).

[100] P. Neumann, J. Beck, M. Steiner, F. Rempp, H. Fedder, P. R. Hemmer, J. Wrachtrup, and F. Jelezko, "Single-Shot Readout of a Single Nuclear Spin", Science **329**, 542 (2010).

[101] V. Dobrovitski, G. Fuchs, A. Falk, C. Santori, and D. Awschalom, "Quantum Control over Single Spins in Diamond", Annu. Rev. Condens. Matter Phys. **4**, 23 (2013).

[102] R. Kalra, A. Laucht, C. D. Hill, and A. Morello, "Robust Two-Qubit Gates for Donors in Silicon Controlled by Hyperfine Interactions", Phys. Rev. X **4**, 021044 (2014).

[103] J. T. Muhonen, A Laucht, S Simmons, J. P. Dehollain, R Kalra, F. E. Hudson, S Freer, K. M. Itoh, D. N. Jamieson, J. C. McCallum, A. S. Dzurak, and A Morello, "Quantifying the quantum gate fidelity of single-atom spin qubits in silicon by randomized benchmarking", J. Phys.: Condens. Mat. **27**, 154205 (2015).

[104] J. L. O'Brien, A. Furusawa, and J. Vučković, "Photonic quantum technologies", Nat. Photonics **3**, 687 (2009).

[105] E. Knill, R. Laflamme, and G. J. Milburn, "A scheme for efficient quantum computation with linear optics", Nature **409**, 46 (2001).

[106] R. W. Boyd, *Nonlinear Optics*, 3rd edition (Elsevier, 2008).

[107] D. G. Cory, A. F. Fahmy, and T. F. Havel, "Ensemble quantum computing by NMR spectroscopy", P. Natl. Acad. Sci. USA **94**, 1634 (1997).

[108] J. Jones, "Quantum computing with NMR", Prog. NMR Spectrosc. **59**, 91 (2011).

[109] L. M. K. Vandersypen and I. L. Chuang, "NMR techniques for quantum control and computation", Rev. Mod. Phys. **76**, 1037 (2005).

[110] R. Alicki and K. Lendi, *Quantum Dynamical Semigroups and Applications*, 1st edition, Vol. 717, Lecture Notes in Physics (Springer-Verlag Berlin Heidelberg, 2007).

[111] H. P. Breuer and F. Petruccione, *The theory of open quantum systems* (Oxford University Press, 2002).

[112] S. J. Glaser, U. Boscain, T. Calarco, C. P. Koch, W. Köckenberger, R. Kosloff, I. Kuprov, B. Luy, S. Schirmer, T. Schulte-Herbrüggen, D. Sugny, and F. K. Wilhelm, "Training Schrödinger's cat: quantum optimal control", Eur. Phys. J. D **69** (2015).

[113] F. Dolde, V. Bergholm, Y. Wang, I. Jakobi, B. Naydenov, S. Pezzagna, J. Meijer, F. Jelezko, P. Neumann, T. Schulte-Herbrüggen, J. Biamonte, and J. Wrachtrup, "High-fidelity spin entanglement using optimal control", Nat. Commun. **5** (2014).

[114] N. Khaneja, T. Reiss, C. Kehlet, T. Schulte-Herbrüggen, and S. J. Glaser, "Optimal control of coupled spin dynamics: design of NMR pulse sequences by gradient ascent algorithms", J. Magn. Reson. **172**, 296 (2005).

[115] S. J. Glaser, "Unitary Control in Quantum Ensembles: Maximizing Signal Intensity in Coherent Spectroscopy", Science **280**, 421 (1998).

[116] A. N. Boto, P. Kok, D. S. Abrams, S. L. Braunstein, C. P. Williams, and J. P. Dowling, "Quantum interferometric optical lithography: exploiting entanglement to beat the diffraction limit", Phys. Rev. Lett. **85**, 2733 (2000).

[117] T. Buckup, T. Lebold, A. Weigel, W. Wohlleben, and M. Motzkus, "Singlet versus triplet dynamics of β-carotene studied by quantum control spectroscopy", J. Photoch. Photobio. A **180**, 314 (2006).

[118] S. Machnes, U. Sander, S. J. Glaser, P. de Fouquières, A. Gruslys, S. Schirmer, and T. Schulte-Herbrüggen, "Comparing, optimizing, and benchmarking quantum-control algorithms in a unifying programming framework", Phys. Rev. A **84**, 022305 (2011).

[119] M. A. Nielsen, "A simple formula for the average gate fidelity of a quantum dynamical operation", Phys. Lett. A **303**, 249 (2002).

[120] S. G. Schirmer and P. de Fouquieres, "Efficient algorithms for optimal control of quantum dynamics: the Krotov method unencumbered", New J. Phys. **13**, 073029 (2011).

[121] M. M. Müller, D. M. Reich, M. Murphy, H. Yuan, J. Vala, K. B. Whaley, T. Calarco, and C. P. Koch, "Optimizing entangling quantum gates for physical systems", Phys. Rev. A **84**, 042315 (2011).

[122] R. Schutjens, F. A. Dagga, D. J. Egger, and F. K. Wilhelm, "Single-qubit gates in frequency-crowded transmon systems", Phys. Rev. A **88**, 052330 (2013).

[123] M. Raginsky, "A fidelity measure for quantum channels", Phys. Lett. A **290**, 11 (2001).

[124] S. Kirkpatrick, C. G. Jr., and M. Vecchi, "Optimization by Simulated Annealing", Science **220**, 671 (1983).

[125] N. Hansen, S. D. Müller, and P. Koumoutsakos, "Reducing the Time Complexity of the Derandomized Evolution Strategy with Covariance Matrix Adaptation (CMA-ES", **11**, 1 (2003).

[126] J. Nelder and R. Mead, "A simple method for function minimization", Comput. J. **7**, 308 (1965).

[127] R. H. Byrd, M. E. Hribar, and J. Nocedal, "An Interior Point Algorithm for Large-Scale Nonlinear Programming", SIAM J. Optim. **9**, 877 (1999).

[128] J. Nocedal, "Updating quasi-Newton matrices with limited storage", Math. Comput. **35**, 773 (1980).

[129] D. J. Egger and F. K. Wilhelm, "Adaptive hybrid optimal quantum control for imprecisely characterized systems", Phys. Rev. Lett. **112**, 240503 (2014).

[130] J. Kelly, R. Barends, B. Campbell, Y. Chen, Z. Chen, B. Chiaro, A. Dunsworth, A. G. Fowler, I.-C. Hoi, E. Jeffrey, A. Megrant, J. Mutus, C. Neill, P. J. J. O'Malley, C. Quintana, P. Roushan, D. Sank, A. Vainsencher, J. Wenner, T. C. White, A. N. Cleland, and J. M. Martinis, "Optimal Quantum Control Using Randomized Benchmarking", Phys. Rev. Lett. **112**, 240504 (2014).

[131] S. Machnes, E. Assémat, D. Tannor, and F. K. Wilhelm, "Tunable, flexible, and efficient optimization of control pulses for practical qubits", Phys. Rev. Lett. **120**, 150401 (2018).

[132] J. Lagarias, J. Reeds, M. Wright, and P. Wright, "Convergence properties of the Nelder-Mead simplex algorithm in low dimensions", SIAM J. Optim. **9**, 112 (1998).

[133] F. Gao and L. Han, "Implementing the Nelder-Mead simplex algorithm with adaptive parameters", Comput. Optim. Appl. **51**, 259 (2012).

[134] S. Bravyi, D. P. DiVincenzo, and D. Loss, "Schrieffer-Wolff transformation for quantum many-body systems", Annals of Physics **326**, 2793 (2011).

[135] J. R. Schrieffer and P. A. Wolff, "Relation between the Anderson and Kondo Hamiltonians", Phys. Rev. **149**, 491 (1966).

[136] J. H. V. Vleck, "On σ-Type Doubling and Electron Spin in the Spectra of Diatomic Molecules", Phys. Rev. **33**, 467 (1929).

[137] L. L. Foldy and S. A. Wouthuysen, "On the Dirac Theory of Spin 1/2 Particles and Its Non-Relativistic Limit", Phys. Rev. **78**, 29 (1950).

[138] S. Teufel, *Adiabatic Perturbation Theory in Quantum Dynamics* (Springer-Verlag Berlin Heidelberg, 2003).

[139] G. Rigolin, G. Ortiz, and V. H. Ponce, "Beyond the quantum adiabatic approximation: Adiabatic perturbation theory", Phys. Rev. A **78**, 052508 (2008).

[140] S. I. Erlingsson, J. C. Egues, and D. Loss, "Energy spectra for quantum wires and two-dimensional electron gases in magnetic fields with Rashba and Dresselhaus spin-orbit interactions", Phys. Rev. B **82**, 155456 (2010).

[141] A. M. Oleś, "Comment on "t/U expansion for the Hubbard model"", Phys. Rev. B **41**, 2562 (1990).

[142] L. C. G. Govia and F. K. Wilhelm, "Entanglement generated by the dispersive interaction: The dressed coherent state", Phys. Rev. A **93**, 012316 (2016).

[143] M. Khezri, E. Mlinar, J. Dressel, and A. N. Korotkov, "Measuring a transmon qubit in circuit QED: Dressed squeezed states", Phys. Rev. A **94**, 012347 (2016).

[144] L. DiCarlo, J. Chow, J. Gambetta, L. Bishop, B. Johnson, D. Schuster, J. Majer, A. Blais, L. Frunzio, S. Girvin, and R. Schoelkopf, "Demonstration of Two-Qubit Algorithms with a Superconducting Quantum Processor", Nature **460**, 240 (2009).

[145] J. Kempe, A. Kitaev, and O. Regev, "The Complexity of the Local Hamiltonian Problem", SIAM J. Comput. **35**, 1070 (2006).

[146] R. Oliveira and B. M. Terhal, "The complexity of quantum spin systems on a two-dimensional square lattice", Quant. Inf. Comp. **8**, 0900 (2008).

[147] S. Bravyi, D. P. DiVincenzo, D. Loss, and B. M. Terhal, "Quantum Simulation of Many-Body Hamiltonians Using Perturbation Theory with Bounded-Strength Interactions", Phys. Rev. Lett. **101**, 070503 (2008).

[148] A. Cottet, "Microwave spectroscopy of a Cooper pair beam splitter", Phys. Rev. B **86**, 075107 (2012).

[149] N. O. Abeling and S. Kehrein, "Quantum quench dynamics in the transverse field Ising model at nonzero temperatures", Phys. Rev. B **93**, 104302 (2016).

[150] J. M. Martinis and M. R. Geller, "Fast adiabatic qubit gates using only σ_z control", Phys. Rev. A **90**, 022307 (2014).

[151] T. Chasseur, L. S. Theis, Y. R. Sanders, D. J. Egger, and F. K. Wilhelm, "Engineering adiabaticity at an avoided crossing with optimal control", Phys. Rev. A **91**, 043421 (2015).

[152] J. D. Strand, M. Ware, F. Beaudoin, T. A. Ohki, B. R. Johnson, A. Blais, and B. L. T. Plourde, "First-order sideband ttransition with flux-driven asymmetric transmon qubits", Phys. Rev. B **87**, 220505(R) (2013).

[153] G. de Lange, B. van Heck, A. Bruno, D. J. van Woerkom, A. Geresdi, S. R. Plissard, E. P.A. M. Bakkers, A. R. Akhmerov, and L. Di-Carlo, "Realization of Microwave Quantum Circuits Using Hybrid Superconducting-Semiconducting Nanowire Josephson Elements", Phys. Rev. Lett. **115**, 127002 (2015).

[154] L. Casparis, T. W. Larsen, M. S. Olsen, F. Kuemmeth, P. Krogstrup, J. Nygård, K. D. Petersson, and C. M. Marcus, "Gatemon Benchmarking and Two-Qubit Operations", Phys. Rev. Lett. **116**, 150505 (2016).

[155] Y. Goldin and Y. Avishai, "Nonlinear response of a Kondo system: Perturbation approach to the time-dependent Anderson impurity model", Phys. Rev. B **61**, 16750 (2000).

[156] A. Imamoglu, D. D. Awschalom, G. Burkard, D. P. DiVincenzo, D. Loss, M. Sherwin, and A. Small, "Quantum Information Processing Using Quantum Dot Spins and Cavity QED", Phys. Rev. Lett. **83**, 4204 (1999).

[157] S. J. Devitt, W. J. Munro, and K. Nemoto, "Quantum error correction for beginners", Rep. Prog. Phys. **76**, 076001 (2013).

[158] W. S. Warren, "Effects of arbitrary laser or NMR pulse shapes on population inversion and coherence", J. Chem. Phys **81**, 5437 (1984).

[159] S. Blanes, F. Casas, J. Oteo, and J. Ros, "The Magnus expansion and some of its applications", Phys. Rep. **470**, 151 (2009).

[160] H. Primas, "Generalized Perturbation Theory in Operator Form", Rev. Mod. Phys. **35**, 710 (1963).

[161] E. T. Jaynes and F. W. Cummings, "Comparison of quantum and semiclassical radiation theories with application to the beam maser", Proc. IEEE **51**, 89 (1963).

[162] M. Boissonneault, J. M. Gambetta, and A. Blais, "Dispersive regime of circuit QED: Photon-dependent qubit dephasing and relaxation rates", Phys. Rev. A **79**, 013819 (2009).

[163] L. C. G. Govia, E. J. Pritchett, B. L. T. Plourde, M. G. Vavilow, R. McDermott, and F. K. Wilhelm, "Scalable two- and four-qubit parity measurement with a threshold photon counter", Phys. Rev. A **92**, 022335 (2015).

[164] D. C. McKay, S. Filipp, A. Mezzacapo, E. Magesan, J. M. Chow, and J. M. Gambetta, "Universal Gate for Fixed-Frequency Qubits via a Tunable Bus", Phys. Rev. Appl. **6**, 064007 (2016).

[165] F. Motzoi and F. K. Wilhelm, "Improving frequency selection of driven pulses using derivative-based transition suppression", Phys. Rev. A **88**, 062318 (2013).

[166] H. Jirari and W. Pötz, "Optimal coherent control of dissipative n-level systems", Phys. Rev. A **72**, 013409 (2005).

[167] P. Rebentrost and F. Wilhelm, "Optimal control of a leaking qubit", Phys. Rev. B **79**, 060507 (2009).

[168] S. Safaei, S. Montangero, F. Taddei, and R. Fazio, "Optimized single-qubit gates for josephson phase qubits", Phys. Rev. B **79**, 064524 (2009).

[169] B Khani, J. M. Gambetta, F Motzoi, and F. K. Wilhelm, "Optimal generation of fock states in a weakly nonlinear oscillator", Physica Scripta **T137**, 014021 (2009).

[170] F. Motzoi, J. M. Gambetta, S. T. Merkel, and F. K. Wilhelm, "Optimal control methods for rapidly time-varying Hamiltonians", Phys. Rev. A **84**, 022307 (2011).

[171] M. Steffen, J. Martinis, and I. Chuang, "Accurate control of Josephson phase qubits", Phys. Rev. B **68**, 224518 (2003).

[172] J. M. Chow, J. M. Gambetta, L. Tornberg, J. Koch, L. Bishop, A. A. Houck, B. R. Johnson, L. Frunzio, S. M. Girvin, and R. J. Schoelkopf, "Randomized Benchmarking and Process Tomography for Gate Errors in a Solid-State Qubit", Phys. Rev. Lett. **102**, 090502 (2009).

[173] R. Unanyan, L. Yatsenko, K Bergmann, and B. Shore, "Laser-induced adiabatic atomic reorientation with control of diabatic losses", Opt. Commun. **139**, 48 (1997).

[174] M. Demirplak and S. A. Rice, "Adiabatic population transfer with control fields", J. Phys. Chem. A **107**, 9937 (2003).

[175] M. Demirplak and S. A. Rice, "On the consistency, extremal, and global properties of counterdiabatic fields", J. Chem. Phys. **129**, 154111 (2008).

[176] M. V. Berry, "Transitionless quantum driving", J. Phys. A: Math. Theor. **42**, 365303 (2009).

[177] E. Torrontegui, S. Ibáñez, S. Martínez-Garaot, M. Modugno, A. del Campo, D. Guéry-Odelin, A. Ruschhaupt, X. Chen, J. G. Muga, et al., "Shortcuts to adiabaticity", Adv. At. Mol. Opt. Phys **62**, 117 (2013).

[178] S. Ibáñez, X. Chen, and J. G. Muga, "Improving shortcuts to adiabaticity by iterative interaction pictures", Phys. Rev. A **87**, 043402 (2013).

[179] L. M. Garrido, "Generalized adiabatic invariance", J. Math. Phys. **5**, 355 (1964).

[180] M. V. Berry, "Quantum phase corrections from adiabatic iteration", P. R. Soc. A **414**, 31 (1987).

[181] J. M. Chow, L. DiCarlo, J. M. Gambetta, F. Motzoi, L. Frunzio, S. M. Girvin, and R. J. Schoelkopf, "Optimized driving of superconducting artificial atoms for improved single-qubit gates", Phys. Rev. A **82**, 040305 (2010).

[182] E. Lucero, J. Kelly, R. C. Bialczak, M. Lenander, M. Mariantoni, M. Neeley, A. D. O'Connell, D. Sank, H. Wang, M. Weides, J. Wenner, T. Yamamoto, A. N. Cleland, and J. M. Martinis, "Reduced phase error through optimized control of a superconducting qubit", Phys. Rev. A **82**, 042339 (2010).

[183] R. Bianchetti, S. Filipp, M. Baur, J. M. Fink, C. Lang, L. Steffen, M. Boissonneault, A. Blais, and A. Wallraff, "Control and tomography of a three level superconducting artificial atom", Phys. Rev. Lett. **105**, 223601 (2010).

[184] D. Ballester, G. Romero, J. J. García-Ripoll, F. Deppe, and E. Solano, "Quantum simulation of the ultrastrong-coupling dynamics in circuit quantum electrodynamics", Phys. Rev. X **2**, 021007 (2012).

[185] J. M. Chow, J. M. Gambetta, A. D. Córcoles, S. T. Merkel, J. A. Smolin, C. Rigetti, S. Poletto, G. A. Keefe, M. B. Rothwell, J. R. Rozen, M. B. Ketchen, and M. Steffen, "Universal quantum gate set approaching fault-tolerant thresholds with superconducting qubits", Phys. Rev. Lett. **109**, 060501 (2012).

[186] E. Magesan, J. M. Gambetta, B. R. Johnson, C. A. Ryan, J. M. Chow, S. T. Merkel, M. P. da Silva, G. A. Keefe, M. B. Rothwell, T. A. Ohki, M. B. Ketchen, and M. Steffen, "Efficient measurement of quantum gate error by interleaved randomized benchmarking", Phys. Rev. Lett. **109**, 080505 (2012).

[187] A. Fedorov, L. Steffen, M. Baur, M. P. da Silva, and A. Wallraff, "Implementation of a toffoli gate with superconducting circuits", Nature **481**, 170 (2012).

[188] A. D. Córcoles, J. M. Gambetta, J. M. Chow, J. A. Smolin, M. Ware, J. Strand, B. L. T. Plourde, and M. Steffen, "Process verification of two-qubit quantum gates by randomized benchmarking", Phys. Rev. A **87**, 030301 (2013).

[189] T. Walter, P. Kurpiers, S. Gasparinetti, P. Magnard, A. Potočnik, Y. Salathé, M. Pechal, M. Mondal, M. Oppliger, C. Eichler, and A. Wallraff, "Rapid high-fidelity single-shot dispersive readout of superconducting qubits", Phys. Rev. Applied **7**, 054020 (2017).

[190] Z. Chen, J. Kelly, C. Quintana, R. Barends, B. Campbell, Y. Chen, B. Chiaro, A. Dunsworth, A. Fowler, E. Lucero, E. Jeffrey, A. Megrant, J. Mutus, M. Neeley, C. Neill, P. O'Malley, P. Roushan, D. Sank, A. Vainsencher, J. Wenner, T. White, A. Korotkov, and J. M. Martinis, "Measuring and suppressing quantum state leakage in a superconducting qubit", Phys. Rev. Lett. **116**, 020501 (2016).

[191] A. M. Forney, S. R. Jackson, and F. W. Strauch, "Multifrequency control pulses for multilevel superconducting quantum circuits", Phys. Rev. A **81**, 012306 (2010).

[192] S. E. Economou and E. Barnes, "Analytic approach to swift nonleaky entangling gates in Superconducting qubits", Phys. Rev. B **91**, 161405 (2015).

[193] C. Zhuang, C. R. Paul, X. Liu, S. Maneshi, L. S. Cruz, and A. M. Steinberg, "Coherent control of population transfer between vibrational states in an optical lattice via two-path quantum interference", Phys. Rev. Lett. **111**, 233002 (2013).

[194] Y.-C. Yang, S. N. Coppersmith, and M. Friesen, "Achieving high-fidelity single-qubit gates in a strongly driven silicon-quantum-dot hybrid qubit", Phys. Rev. A **95**, 062321 (2017).

[195] L. S. Theis, F. Motzoi, and F. K. Wilhelm, "Simultaneous gates in frequency-crowded multilevel systems using fast, robust, analytic control shapes", Phys. Rev. A **93**, 012324 (2016).

[196] G Nenciu, "On the adiabatic theorem of quantum mechanics", J. Phys. A: Math. Gen. **13**, L15 (1980).

[197] T. Kato, "On the adiabatic theorem of quantum mechanics", J. Phys. Soc. Jpn. **5**, 435 (1950).

[198] M. Born and V. Fock, "Beweis des Adiabatensatzes", Zeitschrift für Physik **51**, 165 (1928).

[199] T. Albash and D. A. Lidar, "Adiabatic quantum computation", Rev. Mod. Phys. **90**, 015002 (2018).

[200] M. V. Berry, "Quantal phase factors accompanying adiabatic changes", P. R. Soc. A **392**, 45 (1984).

[201] M. Deschamps, G. Kervern, D. Massiot, G. Pintacuda, L. Emsley, and P. J. Grandinetti, "Superadiabaticity in magnetic resonance", J. Chem. Phys. **129**, 204110 (2008).

[202] D. Petrosyan, F. Motzoi, M. Saffman, and K. Mølmer, "High-fidelity rydberg quantum gate via a two-atom dark state", Phys. Rev. A **96**, 042306 (2017).

[203] F. Motzoi, L. Buchmann, and C. Dickel, "Simple, smooth and fast pulses for dispersive measurements in cavities and quantum networks", arXiv:1809.04116 (2018).

[204] L. S. Theis and F. K. Wilhelm, "Nonadiabatic corrections to fast dispersive multiqubit gates involving z control", Phys. Rev. A **95**, 022314 (2017).

[205] W. Magnus, "On the exponential solution of differential equations for a linear operator", Commun. Pur. Appl. Math. **7**, 649 (1954).

[206] F. Motzoi, "Controlling Quantum Information Devices", PhD thesis (U. Waterloo, 2012).

[207] B. Criger, G. Passante, D. Park, and R. Laflamme, "Recent advances in nuclear magnetic resonance quantum information processing", Philos. T. R. Soc. A **370**, 4620 (2012).

[208] V. Vesterinen, O.-P. Saira, A. Bruno, and L. DiCarlo, "Mitigating information leakage in a crowded spectrum of weakly anharmonic qubits", arXiv:1405.0450 (2014).

[209] T. Caneva, T. Calarco, and S. Montangero, "Chopped random-basis quantum optimization", Phys. Rev. A **84**, 022326 (2011).

[210] B. Khani, S. T. Merkel, F. Motzoi, J. M. Gambetta, and F. K. Wilhelm, "High-fidelity quantum gates in the presence of dispersion", Phys. Rev. A **85**, 022306 (2012).

[211] J. Ghosh and M. R. Geller, "Controlled-NOT logic gate for phase qubits based on conditional spectroscopy", Quantum Inf. Process. **11**, 1349 (2011).

[212] J. M. Chow, A. D. Córcoles, J. M. Gambetta, C. Rigetti, B. R. Johnson, J. A. Smolin, J. R. Rozen, G. A. Keefe, M. B. Rothwell, M. B. Ketchen, and M. Steffen, "Simple All-Microwave Entangling Gate for Fixed-Frequency Superconducting Qubits", Phys. Rev. Lett. **107**, 080502 (2011).

[213] D. Ristè, M. Dukalski, C. A. Watson, G. de Lange, M. J. Tiggelman, Y. M. Blanter, K. W. Lehnert, R. N. Schouten, and L. DiCarlo, "Deterministic entanglement of superconducting qubits by parity measurement and feedback", Nature **502**, 350 (2013).

[214] J. Ghosh, A. Galiautdinov, Z. Zhou, A. N. Korotkov, J. M. Martinis, and M. R. Geller, "High-fidelity controlled-σ^Z gate for resonator-based superconducting quantum computers", Phys. Rev. A **87**, 022309 (2013).

[215] S. Kirchhoff, T. Keßler, P. J. Liebermann, E. Assémat, S. Machnes, F. Motzoi, and F. K. Wilhelm, "Optimized cross-resonance gate for coupled transmon systems", Phys. Rev. A **97**, 042348 (2018).

[216] A. Baksic, H. Ribeiro, and A. A. Clerk, "Speeding up adiabatic quantum state transfer by using dressed states", Phys. Rev. Lett. **116**, 230503 (2016).

[217] D. Jaksch, J. I. Cirac, P. Zoller, S. L. Rolston, R. Côté, and M. D. Lukin, "Fast Quantum Gates for Neutral Atoms", Phys. Rev. Lett. **85**, 2208 (2000).

[218] X. L. Zhang, A. T. Gill, L. Isenhower, T. G. Walker, and M. Saffman, "Fidelity of a Rydberg-blockade quantum gate from simulated quantum process tomography", Phys. Rev. A **85**, 042310 (2012).

[219] M. M. Müller, H. R. Haakh, T. Calarco, C. P. Koch, and C. Henkel, "Prospects for fast Rydberg gates on an atom chip", Quant. Inf. Proc. **10**, 771 (2011).

[220] M. H. Goerz, E. J. Halperin, J. M. Aytac, C. P. Koch, and K. B. Whaley, "Robustness of high-fidelity Rydberg gates with single-site addressability", Phys. Rev. A **90**, 032329 (2014).

[221] M. M. Müller, M. Murphy, S. Montangero, T. Calarco, P. Grangier, and A. Browaeys, "Implementation of an experimentally feasible controlled-phase gate on two blockaded Rydberg atoms", Phys. Rev. A **89**, 032334 (2014).

[222] D. D. B. Rao and K. Mølmer, "Robust Rydberg-interaction gates with adiabatic passage", Phys. Rev. A **89**, 030301(R) (2014).

[223] R. Han, H. K. Ng, and B.-G. Englert, "Implementing a neutral-atom controlled-phase gate with a single Rydberg pulse", Europhys. Lett. **113**, 40001 (2016).

[224] S.-L. Su, E. Liang, S. Zhang, J.-J. Wen, L.-L. Sun, Z. Jin, and A.-D. Zhu, "One-step implementation of the Rydberg-Rydberg-interaction gate", Phys. Rev. A **93**, 012306 (2016).

[225] D. J. Egger and F. K. Wilhelm, "Optimized controlled-Z gates for two superconducting qubits coupled through a resonator", Supercond. Sci. Technol. **27**, 014001 (2013).

[226] E. Fermi, "Über das intensitätsverhältnis der Dublettkomponenten der Alkalien", Z. Phys. **59**, 680 (1930).

[227] C. J. Lorenzen and K. Niemax, "Oscillator strengths of some higher Cs principal series lines", J. Phys. B **11**, L723 (1978).

[228] The AC polarizabilities of the $6s_{1/2}$ ground state and Rydberg states are slightly different which leads to a time dependent detuning during the DRAG pulse. This has not been included in the simulations but can be fully corrected for by changing ω_d during the pulse or by slightly changing the detuning Λ introduced after Eq.(4.2).

[229] I. I. Beterov, I. I. Ryabtsev, D. B. Tretyakov, and V. M. Entin, "Quasiclassical calculations of blackbody-radiation-induced depopulation rates and effective lifetimes of Rydberg nS, nP, and nD alkali-metal atoms with $n \leq 80$", Phys. Rev. A **79**, 052504 (2009).

[230] A. Gilchrist, N. K. Langford, and M. A. Nielsen, "Distance measures to compare real and ideal quantum processes", Phys. Rev. A **71**, 062310 (2005).

[231] C. Sayrin, I. Dotsenko, X. Zhou, B. Peaudecerf, T. Rybarczyk, S. Gleyzes, P. Rouchon, M. Mirrahimi, H. Amini, M. Brune, J.-M. Raimond, and S. Haroche, "Real-time quantum feedback prepares and stabilizes photon number states", Nature **477**, 73 (2011).

[232] P. Campagne-Ibarcq, E. Flurin, N. Roch, D. Darson, P. Morfin, M. Mirrahimi, M. H. Devoret, F. Mallet, and B. Huard, "Persistent Control of a Superconducting Qubit by Stroboscopic Measurement Feedback", Phys. Rev. X **3**, 021008 (2013).

[233] H. Krauter, C. A. Muschik, K. Jensen, W. Wasilewski, J. M. Petersen, J. I. Cirac, and E. S. Polzik, "Entanglement Generated by Dissipation and Steady State Entanglement of Two Macroscopic Objects", Phys. Rev. Lett. **107**, 080503 (2011).

[234] Y. Lin, J. P. Gaebler, F. Reiter, T. R. Tan, R. Bowler, A. S. Sørensen, D. Leibfried, and D. J. Wineland, "Dissipative production of a maximally entangled steady state of two quantum bits", Nature **504**, 415 (2013).

[235] G. Morigi, J. Eschner, C. Cormick, Y. Lin, D. Leibfried, and D. J. Wineland, "Dissipative Quantum Control of a Spin Chain", Phys. Rev. Lett. **115**, 200502 (2015).

[236] F. Reiter, D. Reeb, and A. S. Sørensen, "Scalable Dissipative Preparation of Many-Body Entanglement", Phys. Rev. Lett. **117**, 040501 (2016).

[237] K. P. Horn, F. Reiter, Y. Lin, D. Leibfried, and C. P. Koch, arXiv:1807.10052 (2018).

[238] J. P. Gaebler, T. R. Tan, Y. Lin, Y. Wan, R. Bowler, A. C. Keith, S. Glancy, K. Coakley, E. Knill, D. Leibfried, and D. J. Wineland, "High-Fidelity Universal Gate Set for ^{9}Be$^+$ Ion Qubits", Phys. Rev. Lett. **117**, 060505 (2016).

[239] M. Fewell, "Adiabatic elimination, the rotating-wave approximation and two-photon transitions", Opt. Commun. **253**, 125 (2005).

[240] V. Paulisch, H. Rui, H. K. Ng, and B.-G. Englert, "Beyond adiabatic elimination: A hierarchy of approximations for multi-photon processes", Eur. Phys. J Plus **129** (2014) 10.1140/epjp/i2014-14012-8.

[241] J. Eschner, G. Morigi, F. Schmidt-Kaler, and R. Blatt, "Laser cooling of trapped ions", J. Opt. Soc. Am. B **20**, 1003 (2003).

[242] D. Porras and J. I. Cirac, "Effective Quantum Spin Systems with Trapped Ions", Phys. Rev. Lett. **92**, 207901 (2004).

[243] G. E. Uhlenbeck and L. S. Ornstein, "On the Theory of the Brownian Motion", Phys. Rev. **36**, 823 (1930).

[244] D. T. Gillespie, "Exact numerical simulation of the Ornstein-Uhlenbeck process and its integral", Phys. Rev. E **54**, 2084 (1996).

[245] B. Apolloni, C. Carvalho, and D. de Falco, "Quantum stochastic optimization", Stoch. Proc. Appl. **33**, 233 (1989).

[246] B. Apolloni, N. Cesa-Bianchi, and D. de Falco, "A numerical implementation of quantum annealing", in Proceedings of the international conference on stochastic processes, physics and geometry (1988), pp. 97–111.

[247] C. C. McGeoch, "Adiabatic Quantum Computation and Quantum Annealing: Theory and Practice", Synthesis Lectures on Quantum Computing **5**, 1 (2014).

[248] E. Farhi, J. Goldstone, S. Gutmann, J. Lapan, A. Lundgren, and D. Preda, "A quantum adiabatic evolution algorithm applied to random instances of an NP-complete problem", Science **292**, 472 (2001).

[249] V. N. Smelyanskiy, U. V. Toussaint, and D. A. Timucin, "Simulations of the adiabatic quantum optimization for the Set Partition Problem", arXiv:quant-ph/0112143 (2001).

[250] W. van Dam, M. Mosca, and U. Vazirani, "How powerful is adiabatic quantum computation?", in Proceedings 2001 ieee international conference on cluster computing (2001), pp. 279–287.

[251] D. Aharonov, W. van Dam, J. Kempe, Z. Landau, S. Lloyd, and O. Regev, "Adiabatic quantum computation is equivalent to standard quantum computation", SIAM J. Comput. **37**, 166 (2007).

[252] M. H. S. Amin, C. J. S. Truncik, and D. V. Averin, "Role of single-qubit decoherence time in adiabatic quantum computation", Phys. Rev. A **80**, 022303 (2009).

[253] S. Ashhab, J. R. Johansson, and F. Nori, "Decoherence in a scalable adiabatic quantum computer", Phys. Rev. A **74**, 052330 (2006).

[254] M. H. S. Amin, P. J. Love, and C. J. S. Truncik, "Thermally assisted adiabatic quantum computation", Phys. Rev. Lett. **100**, 060503 (2008).

[255] L. Arceci, S. Barbarino, R. Fazio, and G. E. Santoro, "Dissipative landau-zener problem and thermally assisted quantum annealing", Phys. Rev. B **96**, 054301 (2017).

[256] E. Gibney, "D-wave upgrade: how scientists are using the world's most controversial quantum computer", Nature **541**, 447 (2017).

[257] P. I. Bunyk, E. M. Hoskinson, M. W. Johnson, E. Tolkacheva, F. Altomare, A. J. Berkley, R. Harris, J. P. Hilton, T. Lanting, A. J. Przybysz, and J. Whittaker, "Architectural Considerations in the Design of a Superconducting Quantum Annealing Processor", IEEE T. Appl. Supercon. **24**, 1 (2014).

[258] T. F. Ronnow, Z. Wang, J. Job, S. Boixo, S. V. Isakov, D. Wecker, J. M. Martinis, D. A. Lidar, and M. Troyer, "Defining and detecting quantum speedup", Science **345**, 420 (2014).

[259] S. Mandrà, H. G. Katzgraber, and C. Thomas, "The pitfalls of planar spin-glass benchmarks: raising the bar for quantum annealers (again)", Quantum Sci. Technol. **2**, 038501 (2017).

[260] Office of the Director of National Intelligence, *Quantum Enhanced Optimization (QEO)*, https://www.iarpa.gov/index.php/research-programs/qeo, visited on: 2018-10-17.

[261] S. Novikov, R. Hinkey, S. Disseler, J. I. Basham, T. Albash, A. Risinger, D. Ferguson, D. A. Lidar, and K. M. Zick, "Exploring More-Coherent Quantum Annealing", arXiv:1809.04485 (2018).

[262] W. Vinci and D. A. Lidar, "Non-stoquastic Hamiltonians in quantum annealing via geometric phases", npj Quantum Information **3**, 38 (2017).

[263] J. Roland and N. J. Cerf, "Quantum search by local adiabatic evolution", Phys. Rev. A **65**, 042308 (2002).

[264] J. G. Powles, "The Adiabatic Fast Passage Experiment in Magnetic Resonance", P. Phys. Soc. **71**, 497 (1958).

[265] A. T. Rezakhani, W.-J. Kuo, A. Hamma, D. A. Lidar, and P. Zanardi, "Quantum Adiabatic Brachistochrone", Phys. Rev. Lett. **103**, 080502 (2009).

[266] A. T. Rezakhani, D. F. Abasto, D. A. Lidar, and P. Zanardi, "Intrinsic geometry of quantum adiabatic evolution and quantum phase transitions", Phys. Rev. A **82**, 012321 (2010).

[267] M. Hofmann and G. Schaller, "Probing nonlinear adiabatic paths with a universal integrator", Phys. Rev. A **89**, 032308 (2014).

[268] S. Boixo, T. F. Rønnow, S. V. Isakov, Z. Wang, D. Wecker, D. A. Lidar, J. M. Martinis, and M. Troyer, "Evidence for quantum annealing with more than one hundred qubits", Nat. Phys. **10**, 218 (2014).

[269] L. Zeng, J. Zhang, and M. Sarovar, "Schedule path optimization for adiabatic quantum computing and optimization", J. Phys. A Math. Theor. **49**, 165305 (2016).

[270] L. Landau, "Zur Theorie der Energieübertragung. II", Physikalische Zeitschrift der Sowjetunion **2**, 46 (1932).

[271] C. Zener, "Non-adiabatic crossing of energy levels", P. Roy. Soc. A: Math. Phys. **137**, 696 (1932).

[272] M. Grajcar, S. H. W. van der Ploeg, A. Izmalkov, E. Il'ichev, H.-G. Meyer, A. Fedorov, A. Shnirman, and G. Schön, "Sisyphus cooling and amplification by a superconducting qubit", Nat. Phys. **4**, 612 (2008).

[273] J. Hauss, A. Fedorov, C. Hutter, A. Shnirman, and G. Schön, "Single-qubit lasing and cooling at the rabi frequency", Phys. Rev. Lett. **100**, 037003 (2008).

[274] T. P. Orlando, J. E. Mooij, L. Tian, C. H. van der Wal, L. S. Levitov, S. Lloyd, and J. J. Mazo, "Superconducting persistent-current qubit", Phys. Rev. B **60**, 15398 (1999).

[275] U. Weiss, *Quantum dissipative systems*, 3rd (World Scientific, 2008).

[276] N. G. Dickson, M. W. Johnson, M. H. Amin, R Harris, F Altomare, A. J. Berkley, P Bunyk, J Cai, E. M. Chapple, P Chavez, F Cioata, T Cirip, P deBuen, M Drew-Brook, C Enderud, S Gildert, F Hamze, J. P. Hilton, E Hoskinson, K Karimi, E Ladizinsky, N Ladizinsky, T Lanting, T Mahon, R Neufeld, T Oh, I Perminov, C Petroff, A Przybysz, C Rich, P Spear, A Tcaciuc, M. C. Thom, E Tolkacheva, S Uchaikin, J Wang, A. B. Wilson, Z Merali, and G Rose, "Thermally assisted quantum annealing of a 16-qubit problem", Nat. Commun. **4** (2013).

[277] E. Novais, A. H. Castro Neto, L. Borda, I. Affleck, and G. Zarand, "Frustration of decoherence in open quantum systems", Phys. Rev. B **72**, 014417 (2005).

[278] H. Kohler and F. Sols, "Quasiclassical frustration", Phys. Rev. B **72**, 180404 (2005).

[279] R. Harris, T. Lanting, A. J. Berkley, J. Johansson, M. W. Johnson, P. Bunyk, E. Ladizinsky, N. Ladizinsky, T. Oh, and S. Han, "Compound josephson-junction coupler for flux qubits with minimal crosstalk", Phys. Rev. B **80**, 052506 (2009).

[280] P.-Q. Jin, M. Marthaler, A. Shnirman, and G. Schön, "Strong coupling of spin qubits to a transmission line resonator", Phys. Rev. Lett. **108**, 190506 (2012).

[281] P. Nalbach, "Adiabatic-Markovian bath dynamics at avoided crossings", Phys. Rev. A **90**, 042112 (2014).

[282] M. Yamaguchi, T. Yuge, and T. Ogawa, "Markovian quantum master equation beyond adiabatic regime", Phys. Rev. E **95**, 012136 (2017).

[283] N. Makri, "Numerical path integral techniques for long time dynamics of quantum dissipative systems", J. Math. Phys. **36**, 2430 (1995).

[284] A. Shnirman, Y. Makhlin, and G. Schön, "Noise and decoherence in quantum two-level systems", Phys. Scripta **T102**, 147 (2002).

[285] A. J. Leggett, S. Chakravarty, A. T. Dorsey, M. P. A. Fisher, A. Garg, and W. Zwerger, "Dynamics of the dissipative two-state system", Rev. Mod. Phys. **59**, 1 (1987).

[286] M. Keck, S. Montangero, G. E. Santoro, R. Fazio, and D. Rossini, "Dissipation in adiabatic quantum computers: lessons from an exactly solvable model", New J. Phys. **19**, 113029 (2017).

[287] L. Arceci, S. Barbarino, D. Rossini, and G. E. Santoro, "Optimal working point in dissipative quantum annealing", Phys. Rev. B **98**, 064307 (2018).

[288] K. Kraus, "Measuring processes in quantum mechanics i. continuous observation and the watchdog effect", Found. Phys. **11**, 547 (1981).

[289] M. H. S. Amin and D. V. Averin, "Macroscopic resonant tunneling in the presence of low frequency noise", Phys. Rev. Lett. **100**, 197001 (2008).